NTNU

Norwegian University of
Science and Technology

Modelling Medium- Depth CO_2 Injection at the Svelvik CO_2 Field Laboratory in Norway

Klaus Falk Hagby

Petroleum Geoscience and Engineering
Submission date: June 2018
Supervisor: Ole Torsæter, IGP
Co-supervisor: Anja Sundal, UiO
Alv-Arne Grimstad, SINTEF
Cathrine Ringstad, SINTEF

Norwegian University of Science and Technology
Department of Geoscience and Petroleum

To Finn R. Hagby and Gerd Stenehjem

Summary

The CO_2 Field Lab is a test site at the Svelvik ridge near Oslo in Norway. It is presently being upgraded as part of the European research infrastructure initiative (the ECCSEL laboratories). The test site was established in 2010 by the SINTEF-coordinated "CO_2FieldLab" project with the overall objective to study the performance of monitoring systems to detect and quantify CO_2 migration and leakage.

Modelling of gas injection was performed in the previous projects as part of a feasibility study for geophysical monitoring. This modelling mainly considered the 10-m layer between 60 and 70 m, and consequently assumed zero permeability in the layers above and below. For the present work this constraint is relaxed by assigning a low but non-zero permeability also to the shallower layers. The aim of the work in this thesis is to perform reservoir simulations to investigate major issues related to the operation of a field laboratory. The previous gas injection modelling is simulated by using a homogeneous layercake model, with a simplified relative permeability. This model is evaluated, updated and discussed, in an attempt to increase the accuracy and resolution of the simulations. The geology of the Svelvik ridge is being reviewed, and it is assumed that there are anisotropy present in the north-south and vertical direction. The effect of this is tested by simulating a reduced permeability in the respective directions, for the relevant zones of the reservoir. The relative permeability is calculated by using Corey and Brooks equations, where relative permeability is a function of the grain size distribution. Imbibition curves were calculated with Carlson's method to investigate the effect of hysteresis.

The Svelvik field laboratory is intended for studies of the accuracy and sensitivity of monitoring methods for CO_2 storage. An important part of a monitoring sensitivity test is extensive knowledge of the conditions prior to injection, both for fluid saturations, compositions (brine salinity and CO_2 composition) and pressure. At the moment, before any injection has been performed, these conditions are well known. After the first experimental campaign has been completed, however, these conditions will be more uncertain. For the possibility of conducting more injection tests, it is important to know if and how quickly the conditions will approach a new well-known "reference" state. For pore pressure, this would be relatively fast, due to the relatively high permeability and the short distance to open water a few hundred meters to the north of the Svelvik ridge. For saturations, it would take much longer, and the end state depends on, among other factors, the transport

of brine through the sediments. One of the topics that will be addressed in this thesis is whether it would be possible and/or practical to accelerate this process, by injecting brine for a prolonged period after the end of the gas injection test, or by producing the injected gas out of the reservoir. Due to a low fracture pressure, hence a low injection rate, the brine is not displacing the injected CO_2 efficiently. Production from the reservoir can be a solution to accelerate the system to reach a ”reference” state, where pressure and saturation are known.

Sammendrag

CO_2 Field Lab er en feltlab ved Svelvik utenfor Oslo i Norge. Den blir for tiden oppgradert som en del av European research infrastructure initiative (ECCSEL-laboratoriene). Feltlaboratoriet ble etablert i 2010 av det SINTEF-koordinerte "CO_2 FieldLab"-prosjekt med det overordnede målet å studere overvåkingssystemers evne til å oppdage og kvantifisere CO_2 migrasjon og lekkasje.

Modellering av gassinjeksjon ble utført i de foregående prosjektene som en del av en mulighetsstudie for geofysisk overvåking. Denne modelleringen vurderte hovedsakelig 10-m-laget mellom 60 og 70 m, og det ble antatt null permeabilitet i lagene over og under. For det nåværende arbeidet er denne begrensningen avslappet ved å tildele lav, men ikke-null permeabilitet også til de grunne lagene. Målet med arbeidet i denne oppgaven er å utføre reservoirsimuleringer for å undersøke problemer tilknyttet driften av feltlaboratoriumet. Den forrige gassinjeksjonsmodellen ble simulert ved å bruke en homogen lagekake-modell, med en forenklet relativ permeabilitet. Denne modellen evalueres, oppdateres og diskuteres, i et forsøk på å øke nøyaktigheten og oppløsningen til simuleringene. Geologien til Svelvik-ryggen blir gjennomgått, og det antas at det er anisotropi i nord-sør og vertikal retning. Effekten av dette testes ved å simulere en redusert permeabilitet i de respektive retninger, for de relevante sonene i reservoaret. Den relative permeabiliteten beregnes ved bruk av Corey og Brooks-ligninger, hvor relativ permeabilitet er en funksjon av kornstørrelsesfordelingen. Imbiberingskurver ble beregnet med Carlsons metode for å undersøke effekten av hysterese. Svelvikfeltlaboratoriet er ment for studier av nøyaktigheten og følsomheten til overvåkingsmetoder for CO_2 lagring. En viktig del av en overvåkningssensitivitetstest er omfattende kjennskap til forholdene før injeksjon, både for metninger, sammensetninger (saltvanns salinitet og CO_2 sammensetning) og trykk. For øyeblikket, før noen injeksjon er utført, er disse forholdene godt kjent. Etter at den første eksperimentelle kampanjen er fullført, vil disse forholdene imidlertid være mer usikre. For å bedre muligheten for å utføre flere injeksjonstester, er det viktig å vite om/hvor raskt forholdene vil nærme seg en ny, kjent "referanse" -stat. For poretrykk vil dette være relativt raskt, på grunn av den relativt høye permeabiliteten og den korte avstanden til åpent vann noen få hundre meter nord for Svelvik-åsen. For metningene vil det ta mye lengre tid, og avhenger blant annet av naturlig transport av vann gjennom sedimentene. Et av emnene som skal behandles i denne oppgaven er om det ville være mulig og/eller praktisk

å akselerere denne prosessen ved å injisere saltlake i lengre tid etter slutten av gassinjeksjonstesten eller ved å produsere den injiserte gasen ut av reservoaret. På grunn av et lavt fraktureringstrykk, og dermed en lav injeksjonsrate, forskyver ikke det injiserte saltvannet gassen effektivt. Produksjon fra reservoaret kan være en løsning for å akselerere systemet for å nå en ”referanse” tilstand der trykk og metning er kjent.

Preface

This thesis is the final product of the five year MSc program in Petroleum Geosciences and Engineering with specialisation in Reservoir Technology and Petrophysics. It was written at the Department of Geoscience and Petroleum (IGP) at the Norwegian University of Science and Technology (NTNU) in cooperation with SINTEF.

Acknowledgements

I would like to thank my supervisor, Professor Ole Torsæter for guidance throughout this process. The help, guidance and feedback from Alv-Arne Grimstad and Cathrine Ringstad has been invaluable, this thesis could not have been done without you. I would also like to give a big thanks to Anja Sundal for all her help and feedback. Thank you Kaja Hagby Johnsen and Cecilie Hagby for proofreading.

Lastly I would like to thank my wife, Marianne Falk Hagby, for support, encouragement and patience. You are my rock.

Contents

List of Figures

Chapter 1

Introduction

Climate change and global warming are concepts widely discussed by media, scientists and the average person for the last two decades. Since the beginning of the industrial revolution, around 1750, human activity has caused an increase in the concentration of greenhouse gases in the atmosphere. The greenhouse gases consist mainly of carbon dioxide (CO_2), methane (CH_4), nitrous oxide (N_2O) and water, H_2O. The increasing emissions of methane and nitrous oxide are caused mainly by agriculture and deforestation. Carbon dioxide is a byproduct of combustion reactions, and therefore it occurs in almost all processes where energy is required. The use of fossil fuels in industry, transportation and power generation are the main contributors to the increasing emissions (Bachu, 2015). Due to the population growth and increasing middle class in countries such as China and India, the demand of energy is higher than ever.

Figure 1.1 from U.S. Energy Information Administration (2017) is showing the world energy consumption by energy source. The graph shows that it is estimated that the consumption of petroleum and other liquids as well as natural gas will continue to increase, and that the consumption of coal will stay approximately the same for the next decades. This emphasizes the need for technology to reduce the consequence of the continued fossil fuel combustion.

The Paris Agreement was signed in April 2016, and is a convention between 170 countries. The central goal of the agreement is to keep the global temperature rise below 2°C this century compared to pre-industrial level, and even pursue efforts to limit the increase even further to 1.5°C, (UNFCCC, 2017). In order to accomplish this, the anthropogenic greenhouse gas emissions into the atmosphere has to be reduced by 80% to 95% by 2050, (STEMM-CCS, 2017). Furthermore, it is estimated that renewable energy sources can not fulfill the goal of the Paris Agreement alone. The CEO of the Global CCS Institute, Brad

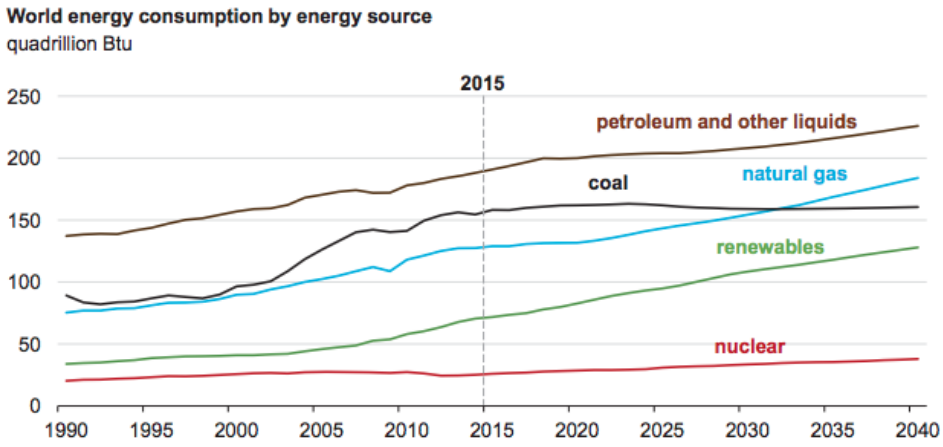

Figure 1.1: World energy consumption by energy source. Historical data until 2015, estimated consumption for the future (U.S. Energy Information Administration, 2017)

Page said at the 23^{rd} conference of the parties (COP23), (Global CCS Institute, 2017):

> *"Renewables alone would not meet international climate change targets, and expert opinion was conclusive that CCS must be part of a suite of clean technologies needed to achieve below 2 degree targets".*

In the light of the increasing demand for knowledge on CO_2 storage, many CCS research projects has been conducted. The CCS research project CO_2FieldLab, was conducted by SINTEF and partners from 2009 to 2015. The overall objective of the project was to study the performance of monitoring systems to detect and quantify CO_2 migration and leakage. Presently, a continuation of the project is initiated, and activity on the test site is set to start in January 2019.

Chapter 2

Background

2.1 CCS

Carbon Capture and Storage, CCS, is a common name for the different processes needed to efficiently store CO_2. Within CCS, there are three main areas of focus: Capture, Transportation and Storage.

2.1.1 Capture

Industry and fossil fuel combustion power plants are among the major emitters of CO_2 and are natural points to capture large volumes of CO_2 for storage. Capturing CO_2 involves separating CO_2 from other gases, for instance flue gases, or hydrocarbon gas containing a large amount of CO_2, before it is compressed. The CO_2 gas is usually compressed into liquid form, so that the transportation becomes more effective (Norwegian Petroleum Directorate, 2017).

Chemical absorption is the most common technology for capturing CO_2. It is a multistage process which is illustrated in Figure 2.1. The process starts with flue gases being sent into an absorber. In the absorber it will react with advanced chemical mixtures or pure solutions that will dissolve the CO_2 physically (Hoff, 2017). Then the solution is sent to a stripper where the CO_2 will be separated from the absorbing chemical. For illustration, at SINTEFs CO_2 capture lab at Tiller outside Trondheim in Norway, they use the amine; monoethanolamine (MEA). The result will be an (almost) pure stream of CO_2. There are several other components in this process, such as heat exchangers, pumps, boilers etc. These are mainly included in the process to reduce energy consumption.

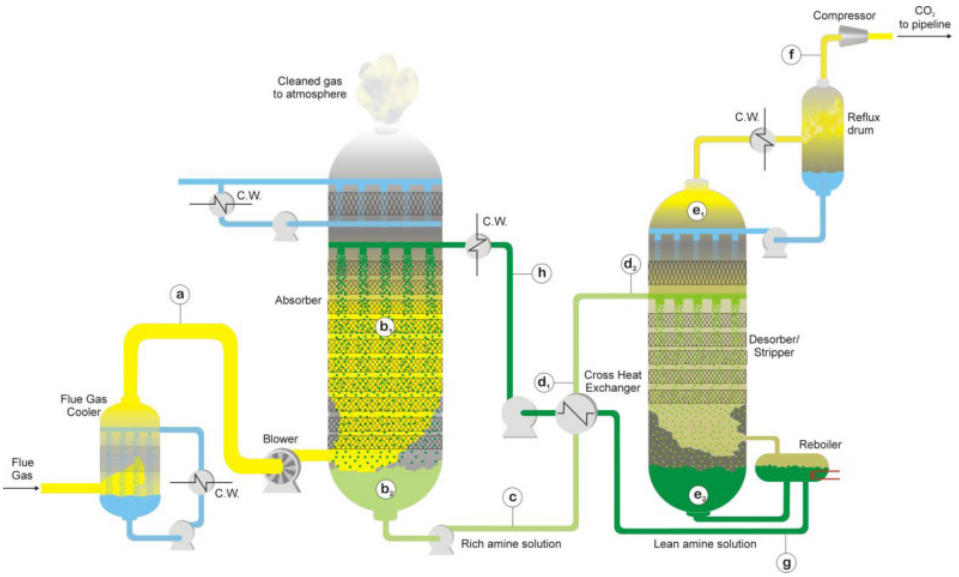

Figure 2.1: Illustration of CO_2 capture with Absorber and Stripper (Krzemień, 2013).

Other possible CO_2 capture methods are pre-combustion separation of CO_2 and oxy-fuel combustion. The pre-combustion separation involves extraction of carbon from the fuel before the fuel is combusted for energy generation. This is done by first creating CO gas in a conversion facility, then the CO gas and water vapour is converted to hydrogen and CO_2. The hydrogen can be used for fuel, which do not generate CO_2 when combusted. About 90 $\%$ of the CO_2 in the fuel can be cleaned using this technology. Oxyfuel combustion is a complete combustion where the post combustion flue gas is only consisting of CO_2 and H_2O. The H_2O is removed by condensation. (Norwegian Petroleum Directorate, 2017) After the CO_2 is captured and compressed it is transported to the storage site.

2.1.2 Transportation

Transportation is the stage of carbon capture and storage (CCS) that links the the capturing facility to the storage site. This involves infrastructure, such as pipelines and/or shipping. An important aspect of the transportation of a gas is that to be able to transport large volumes efficiently, especially by ships, it needs to be in a super critical phase or liquefied. Liquefying CO_2 requires high pressure and low temperatures as shown in Figure 2.2, and is very energy consuming Palmer and Doctor (2017). Eventually the CO_2 reaches the storage location.

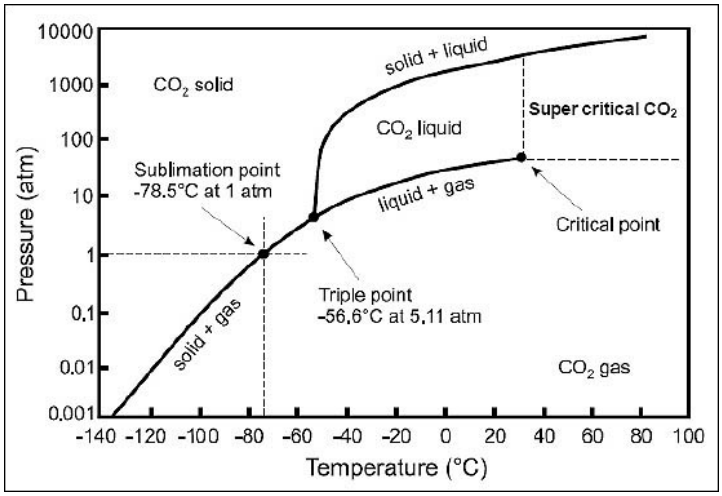

Figure 2.2: Phase Diagram for CO_2 Institute (2018)

2.1.3 Storage

When choosing a storage location, there are many factors that has to be considered. Properties of the storage formation and the sealing unit(s) are crucial, and some of these key indicators are listed in Table 2.1. The table describes the ideal storage reservoir as a reservoir with high capacity, in terms of high porosity and permeability large bulk volume. The ideal cap rock, eg. an unfaulted and continuous, thick confining layer, has a very low risk of leakage.

Table 2.1: Key geological indicators for storage site suitability Chadwick et al. (2017)

	Positive indicators	**Cautionary indicators**
Storage capacity		
Total storage capacity	Reservoir capacity >Source capacity	Reservoir capacity <Source capacity
Reservoir properties		
Depth	1000m - 2500m	Less than 800m, More than 2500m
Reservoir thickness (net)	>50m	<20m
Porosity	>20%	<10%
Permeability	>300 mD	<10 - 100 mD
Salinity	>100 (g/L)	<30 (g/L)
Caprock properties		
Lateral continuity	Unfaulted	Lateral variations, faulting
Thickness	>100m	<20m
Capillary entry pressure	Capillary entry pressure much greater than buoyancy force of max predicted CO_2 column height	Capillary entry pressure similar to buoyancy force of max predicted CO_2 column height

Usually two types of reservoirs are considered for storage, deep saline aquifers and

empty oil or gas reservoirs. There are pros and cons of both alternatives. Aquifers can be found all over the world, and the risk of leakage through abandoned wells is lower than in a depleted oil field. Depleted reservoirs have the benefit of existing infrastructure and usually a complementary amount of data. Depth is also an important factor. As pressure and temperature affects CO_2 to a greater extent than water or oil, the storage efficiency will increase non-linearly with depth (Bachu, 2015). When the location is selected, the injection has to be planned. Storage efficiency is a widely used parameter in CO_2 storage literature, and it is defined as the ratio of the volume occupied by CO_2 to a total pore volume. It is expressed by the storage efficiency coefficient E_s:

$$E_s = \frac{V_{CO_2}}{V_\phi} \tag{2.1}$$

Where it is usual to express the V_{CO_2} as the cumulative injection of CO_2. V_ϕ is the pore volume (Bachu, 2015). The storage capacity, hence the storage efficiency, can be increased artificially, and it has to be assessed whether or not these methods are required to fulfill the total storage capacity criteria in Table 2.1. Such methods are often referred to as "active storage management". These revolve around controlling the pressure build up and accessing more storage volume. Four main strategies for pressure management are often considered:

- Stopping injection, waiting for the system to reach equilibrium.
- Producing at the injection well
- Producing at a distant well and stopping injection
- Producing at a distant well without stopping injection

Where only the fourth option will effectively increase storage capacity (Bachu, 2015). To access more storage volume, multiple injection wells could be used. The usage of horizontal wells would not increase the storage capacity, but it could decrease the number of injection wells required. Co-injection of CO_2 and water would decrease density and viscosity contrasts between the injected fluid and the resident brine, allowing the CO_2 to be displaced deeper into the formation and hence increasing the storage efficiency. Injection of brine after the injection of CO_2 is also an option as this will lead to an imbibition process increasing snap-off and capillary trapping (Krevor et al., 2015). When controlling the pressure build up, storage security is dependant of the maximum acceptable pressure. This is the limit defined at the location with the lowest allowable maximum pressure. This location may not be close to the injection well (SCCS, 2015). Storage efficiency calculated and published in literature varies in the range from $< 1\%$ to $> 10\%$, (Bachu, 2015).

There are several different storing mechanisms that occur during the CO_2 injection- and post-injection phase. Initially, stratigraphic storage is the dominating mechanism. As the CO_2 plume migrates, brine starts to imbibe back into the pores, trapping the residual CO_2 saturation. This is often referred to as residual or capillary trapping. The CO_2 will, with time, dissolve into the brine, this is the effect defining solubility storage. After thousands of years, precipitation and mineral trapping will occur. This increase in CO_2 being trapped by capillary-, solubility- and mineral trapping, results in an increase in storage security with time (Krevor et al., 2015). These different trapping mechanisms are shown in Figure 2.3.

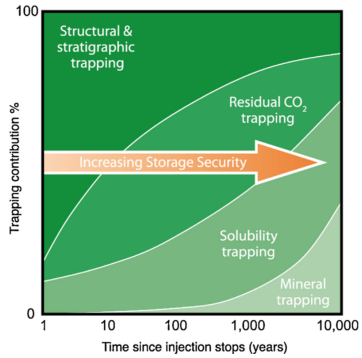

Figure 2.3: A schematic figure of the relative importance of various trapping mechanisms over time. Krevor et al. (2015)

During the injection phase and to some extent in the post-injection phase, monitoring verifies the security of the storage. Most importantly, potential leakages could be detected, but monitoring is also a tool used frequently to confirm and improve the accuracy of scientists models on CO_2 behaviour as an injection fluid. Some of the monitoring methods typically used in CCS projects are listed below.

Well Monitoring: Monitoring of CO_2 injection rate, temperature, formation and wellhead pressure.

Cross-Well and 3-D Seismic: Seismic surveys creates a three dimensional picture of the subsurface by measuring the differences in reflected sound waves created by changes in pressure or density. Seismics can identify where the CO_2 plume is located, give vital information of stratigraphic features of the subsurface, and even give a picture of the initial water saturation.

Acoustic Emissions:A technique used to track the movement of injected CO_2 by recording small sounds created by the CO_2 movement through the formation rock.

Wireline Monitoring (WL): Wireline measurements are common in the oil and gas industry,

and the range of different tools is large. A typical application could be to measure saturation, porosity and permeability for model validation. WL monitoring could also be used above storage formation to confirm containment. In storage projects, there are usually a limited amount of wells. As a result wireline measurements and monitoring are usually conducted in the injection zone. This type of monitoring is conducted when there is a stop in the injection or during maintenance.
Brine Chemistry: Fluid samples are gathered to look at chemical changes caused by the injection of CO_2 (Rodoste, 2010). These are monitoring methods used in both large scale CCS facilities and on small test sites.

2.2 Trapping Methods and Residual Gas Saturation

Reservoir technology is highly important when assessing a potential storage location for CO_2. It is essential to understand the trapping mechanisms taking place in the underground, when different artificially enhancing methods for storage capacity are being assessed. The definition of the storage efficiency, Equation 2.1, illustrates the need for increasing pressure of the CO_2 so that the injected fluid has as high density as possible. Depth of the storage reservoir is therefore an important parameter to ensure that the CO_2 is stored in a dense phase or a super critical phase. The storage efficiency is dependant on many factors. Among the different storing mechanisms, the residual trapping, or capillary trapping is specifically interesting from a reservoir technological view. When we look at the pore scale physics, we assume for simplicity that CO_2 is the non-wetting phase, and that there are two types of flow in porous media: Frontal, or piston-like advance and wetting layer flow. The process when the wetting phase pushes the non-wetting phase directly out of the pore during imbibition, is called frontal advance. This inhibits trapping, as the residual saturation of the non-wetting phase decreases. This happens when a high number of pore throats around the pore are filled with wetting phase. This reduces the radius of curvature and the displacement can happen at a lower pressure in the wetting phase, P_w. The displacement pressure can be expressed with the capillary pressure P_c:

$$P_c = \frac{2\sigma cos\theta}{r} \tag{2.2}$$

Where σ is the interfacial tension between the two phases, θ is the contact angle and r is the radius of curvature.

When the radius of curvature is smaller, the displacement can take place at a higher

capillary pressure, hence lower a water pressure since

$$P_c = P_{non-wetting} - P_{wetting} \tag{2.3}$$

The wetting layer flow is on the other hand not inhibiting trapping, but it is a vital criteria to have capillary trapping. When water is displaced by CO_2 during drainage, some water will remain in the smallest areas of the pore space. These are not molecular films, but bulk volumes that can allow significant flow. As the water pressure starts to increase and the capillary pressure starts to decrease, these wetting layers will start to swell. When an advancing contact angle θ_α is reached as shown in Figure 2.4, the wetting layers will move towards each other until the non-wetting phase is no longer in contact with the surface.

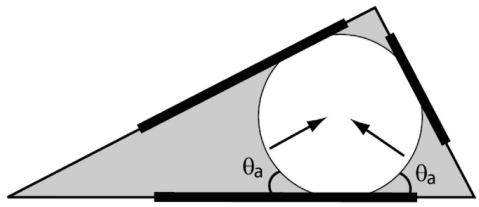

Figure 2.4: Cross section of a pore throat, where advancing contact angle is reached (Krevor et al., 2015).

The situation when the non-wetting phase is no longer in contact with the surface is very unstable, and water will rapidly fill the pore throat and CO_2 is effectively trapped in the pore. This process is called snap-off and is a key process of capillary trapping.

In the oil and gas industry it is common to assume gas as the non-wetting phase, but is not always strongly wetting by water. Therefore the possibility of gas as a wetting phase should be assessed. Since a water wet system is a criteria for wetting layer flow and snap-off, the difference in residual CO_2 saturation is large. The difference in residual saturation for the two wetting phases can be seen on the capillary pressure curves in Figure 2.5. CO_2 is injected during the primary drainage phase. This will increase the pressure in the non-wetting phase and therefore also the capillary pressure, as can be seen from Equation 2.3. When the gas injection has stopped, the water will imbibe back into the pores, and the wetting phase pressure will increase. From Equation 2.3 one can see that an increase in the wetting phase pressure will decrease the capillary pressure. The residual saturation is measured when P_c = 0. Figure 2.5 illustrates that the residual saturation for the non-wetting phase is smaller for the mixed wet system.

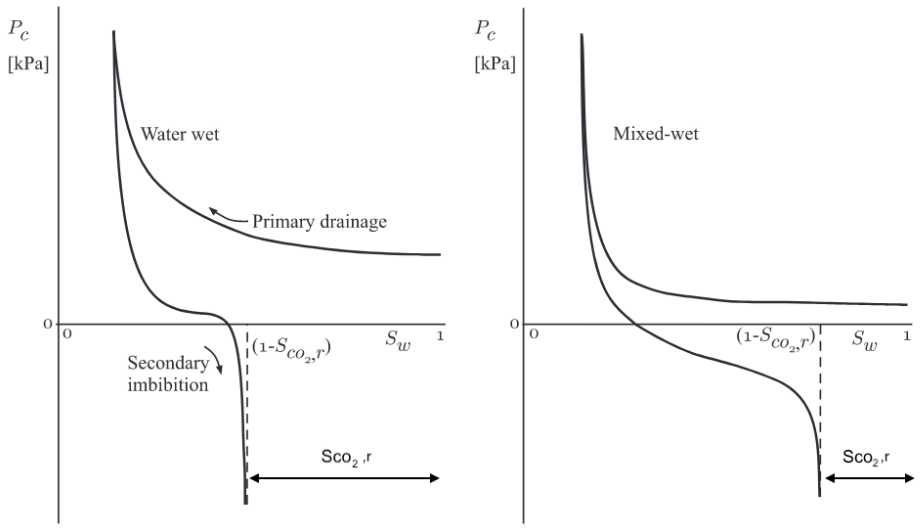

Figure 2.5: Pc vs Sw for two water-wet and mixed-wet systems during drainage and imbibition Krevor et al. (2015)

Mixed wet systems can occur when organic rich materials contaminate the surface of the rock, for instance in coal beds or depleted hydrocarbon reservoirs. Because of valuable infrastructure and data connected to the hydrocarbon reservoirs, these stand out as possible storage locations, hence understanding trapping mechanisms in such systems is valuable and important.

Another important factor to address is heterogeneity within the storage formation. Heterogeneity in form of layers with different permeability has a high influence on pressure build up and storage efficiency. Essentially, the most common effect observed is that heterogeneity could lead to higher capillary trapping as low permeable layers can work as local traps. Simulations ignoring the effects of heterogeneity will among other things observe significant changes in plume behaviour (Krevor et al., 2015). These low permeability layers will also increase the lateral pressure build up and the maximum pressure observed near the injection well.

Later in this thesis the effect of anisotropy, relative permeability and hysteresis will be discussed. The relative permeability is defined as the ratio of the effective permeability of a given phase to the absolute permeability. In this thesis, a gas-brine system is considered, where CO_2 is the non-wetting phase and brine is the wetting phase. The relative permeability is a function of saturation and other factors such as the grain size distribution. The relationship suggested by Corey and Brooks displayed in Equation 2.4 can be rewritten as the logarithmic equivalent as in Equation 2.5 (Standing, 1975).

$$(P_c/P_e)^{-\lambda} = \frac{(S_w - S_{wi})}{(1 - S_{wi})} \tag{2.4}$$

$$logP_c = logP_e - (1/\lambda)log\frac{(S_w - S_{wi})}{(1 - S_{wi})} \tag{2.5}$$

Where:

$P_c =$ Capillary pressure
$P_e =$ Capillary entry pressure
$S_w =$ Water saturation
$S_{wi} =$ Initial water saturation

Relative permeability hysteresis is the effect caused by the ”history” of the system. This effect is essential and will be discussed further in ”Theoretical Approach”.

Hysteresis and relative permeability as a function of grain size distribution are among the updates of the simulation model conducted in this thesis. The effect of these updates were tested in the reservoir simulator Eclipse.

2.3 The Svelvik CO_2ield Lab

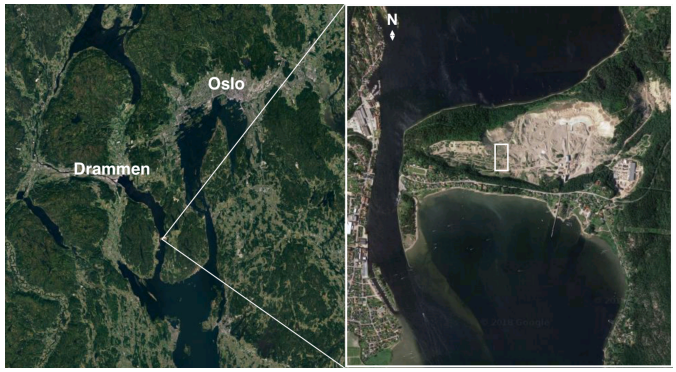

Figure 2.6: The CO_2 Field lab is located in a sand quarry about 50 km south of Oslo. Site marked with a white square. Picture taken from google maps

The Svelvik CO_2 Field Lab is a small scale field lab focusing on CO_2 storage research, that is located about 50 km south of Oslo in the outer part of the Drammensfjord, as shown in Figure 2.6. The research site is located in a sand quarry operated by Svelviksand AS. There was conducted a geological site characterization from 2009 to 2010, including drilling of an appraisal well and geological surveys like Electrical Resistivity Tomography (ERT),

Ground Penetrating Radar (GPR) and 2D seismic. From 7th to 12th September 2011, 1.7 tonnes of CO_2 were injected into the reservoir with a wellhead pressure of 1.9-2 bar at a depth of 20 m. There were made simulation models and geological models to describe and predict the migration and movement of the injected CO_2, but the results of the shallow injection was not completely corresponding to the models. From this project the following wells were preserved:

- The Svelvik #1 Well, a 330m deep appraisal well.
- The Svelvik #2 Well, a 90m deep well promising for injection at between 60m and 70m.
- Eight monitoring pipes and ten ground water wells.

Presently, SINTEF is planning to start up the test site once again. With valuable data from the previous project, and partners, SINTEF starts a new project, making the test site ready for CO_2 injection tests. The plan is to inject CO_2 into the Svelvik #2 well between 60-70m. This is assumed to be a silty layer with a permeability suited for CO_2 injection. The injection zone is lying under a muddy layer with low permeability, expected to work as a cap rock. To monitor the injection and the evolution of the CO_2 plume, it is planned to drill four new monitoring wells. These wells will be completed with a fiberglass casing, a fiber optic cable for distributed seismic (DAS) and temperature (DTS-measurements). There will be a permanent cross well monitoring of electrical resistivity tomography (ERT), and in situ measurements of pressure, CO_2 concentration, salinity and pH. Figure 2.7 shows an illustration of a possible well placement. The placement of the monitoring wells in Figure 2.7 are just illustrative, and not necessarily the actual placements. It is ideal to place the wells so that they ”surround” the injection well, Svelvik #2. It could be ideal if two wells were placed along the north-south seismic line marked with green dots, so that well data can be used in combination with the seismic. The test site is assumed to be ready for experiments in January 2019.

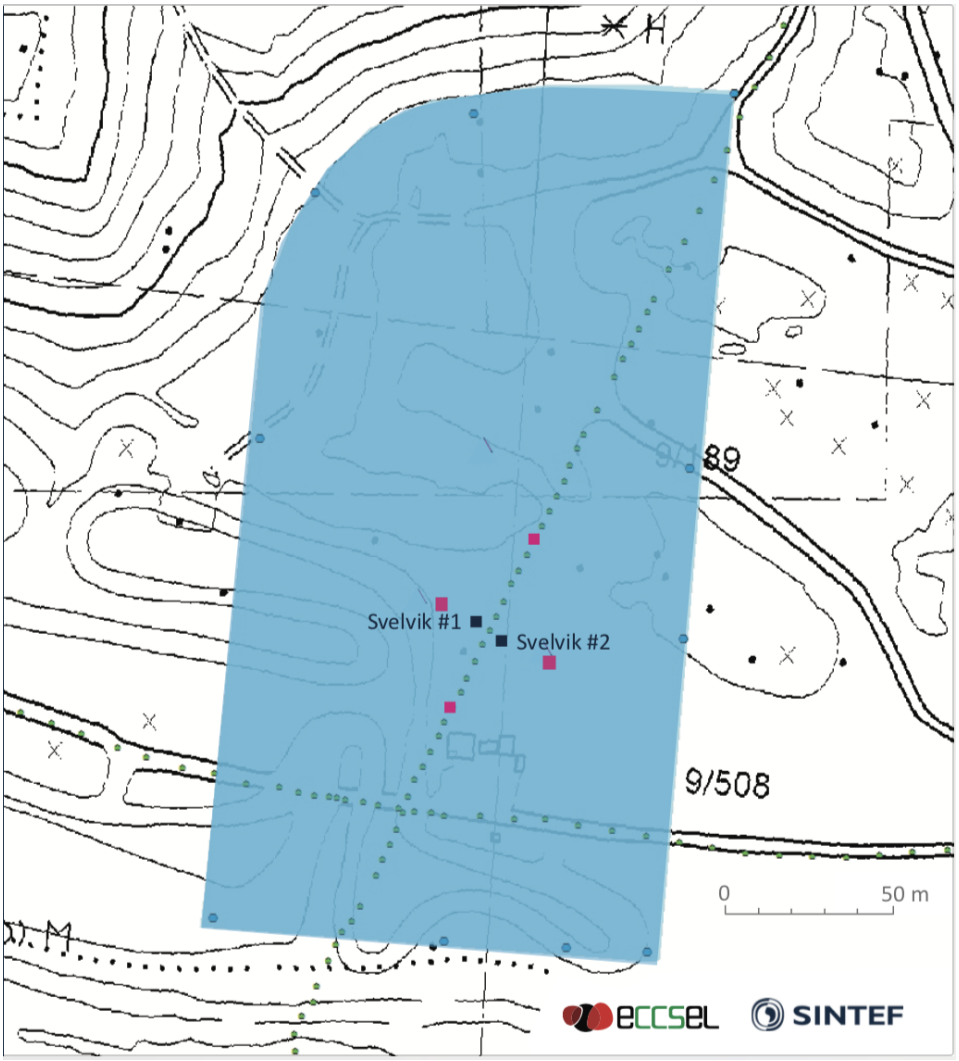

Figure 2.7: Illustration of a possible placement of the monitoring wells around the Svelvik #2 well. Monitoring wells shown as pink squares. Adapted from Ringstad (2017)

Chapter 3

Theoretical Approach

3.1 Geological Background

The injection site is located at the Svelvik ridge in the Drammensfjord, south west of Oslo in Norway. The east-west running ridge consist of unconsolidated ice contact deposits formed during the Ski stage of the Holocene ice recession approximately 10 000 years ago. The deposit forms a sill in the fjord as can be seen in Figure 3.1, and works as a blockage between the outer and inner fjord. This blockage creates Norway's second strongest tidal, the *Svelvikstrøm*.

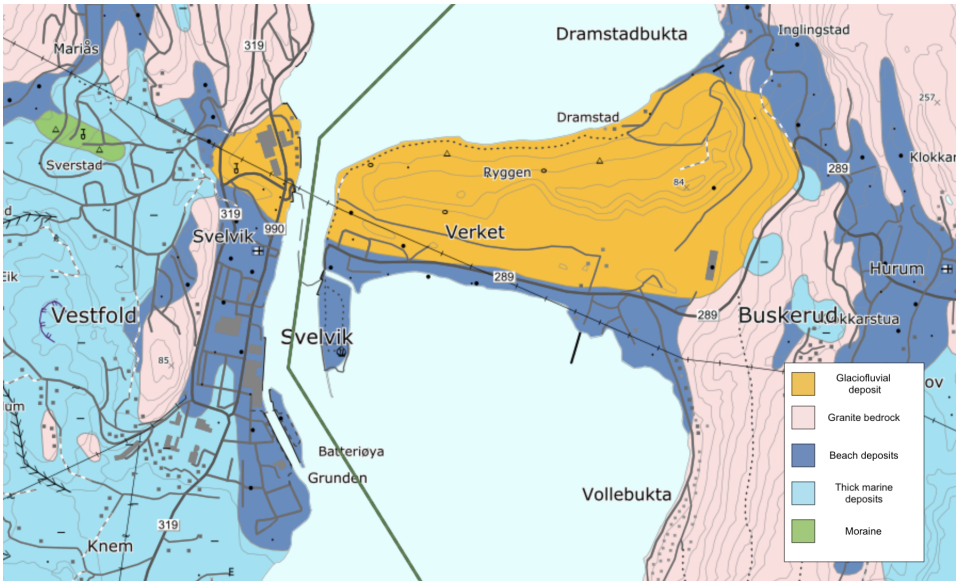

Figure 3.1: A geological map showing the Svelvik ridge, produced by Norges Geologiske Undersøkelse, showing the Svelvik ridge in orange (NGU, 2018).

In Figure 3.1 the orange colour represent *glaciofluvial deposit*, while the dark blue represent a *Beach deposits*. The Svelvik ridge was deposited in pro-glacial fluvial and marine environments during a halt in ice retreat. This retreat was a response to a period of warming after the *Younger Dryas* cool period. During the Ski stage, the ice readvanced and it kept its position for a significant time, around 10 000 years ago (Sørensen, 1981). The beach deposits are well sorted, washed and reworked by waves and currents in the shoreface (Sørensen et al., 1990). The local bedrock, marked in pink in Figure 3.1, is dominated by Drammensgranite. Small morains like the one marked in green right above *"Sverstad"* in Figure 3.1 can be found in the area.

Earlier, the Svelvik Ridge has been interpreted by, among others, Sørensen in 1981 and 1990, and Melø in 2011. Melø uses Lønnes models for ice-contact glaciomarine systems to describe the ridge as he states that the glacier, at one point, came in contact with the ocean, therefore, subsequently the deposit can be characterized as a glaciomarine ice-contact system (Melø, 2011). Lønne (1993) proposed a system for classifying these systems. She stated that the depositional settings for these systems are very complex. The main sedimentary supply comes from two sources, unsorted sub glacial diamictic material and outwash material from the meltwater outflow. Meaning that the sediments of the deposit should be *diamictic* or *poorly sorted* in nature as well as showing a varied lithologic composition. The glaciomarine termini systems can be classified in three main

facies as illustrated in Figure 3.2-3.4:

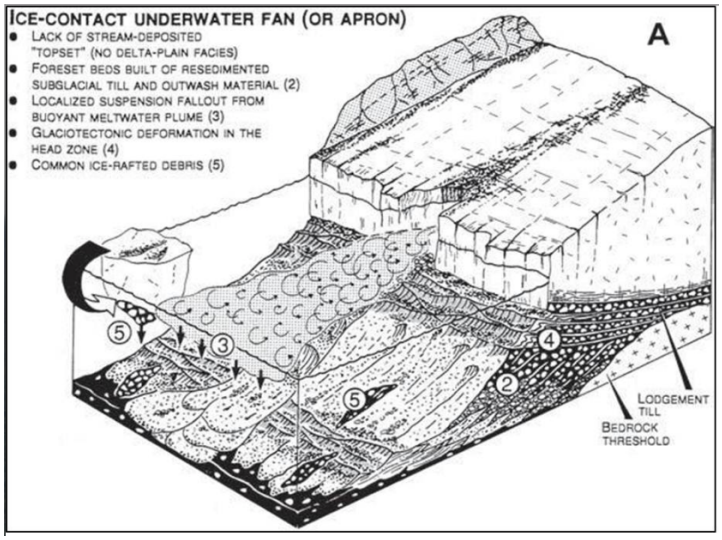

Figure 3.2: Illustrations of ice-contact underwater fan, (Barker, 2011).

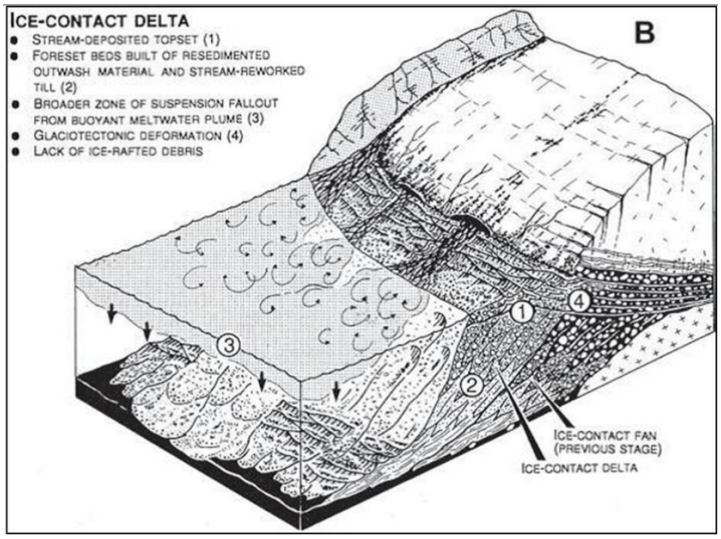

Figure 3.3: Illustrations of an ice-contact delta, (Barker, 2011).

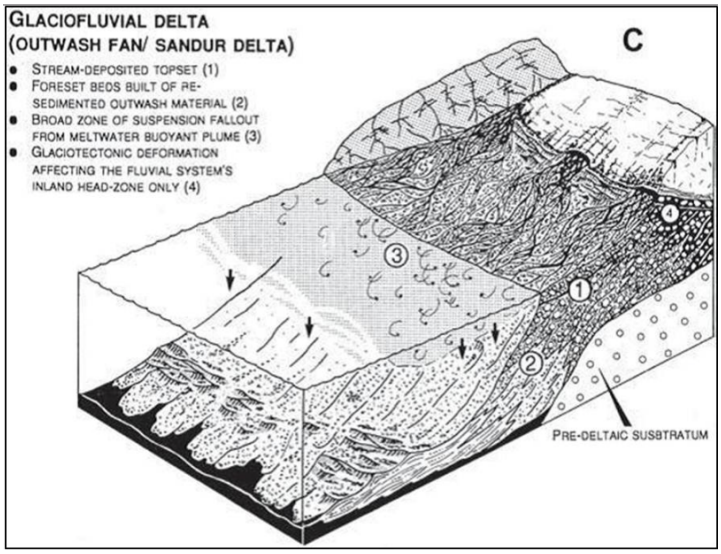

Figure 3.4: Illustrations of a glaciofluvial delta, (Barker, 2011).

Among these three illustrations displayed in Figures 3.2-3.4, Melø (2011) interprets the Svelvik ridge as an Ice-contact submarine fan. Like illustrated in Figure 3.2, this is a wedge of coarse grained materials which has been deposited under water in front of the glacier. The wedge has bedded fore- and bottomset deposits, however, there is no top set on the wedge, as there is a lack of stream activity. The submarine fan was formed by resedimentation of the poorly sorted (diamictic) glacial material along with ice rafted debris from melting sea ice (Lønne, 1993).

Figure 3.5 shows a cross section of Lønne's Ice-contact submarine fan model, where the depositis are devided into four major sedimentary facies, A, B, D and E.

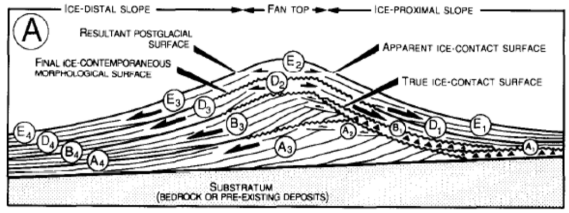

Figure 3.5: Cross section of an Ice-contact submarine fan with four major sedimentary facies, A, B, D and E (Lønne, 1993).

Unit A in Figure 3.5 is devided into four sub-units, A_1, A_2, A_3 and A_4. These are ice-contact facies formed during the glacier's advance. A_3 represent a facies that will

normally comprise of coarse grained clinoformal (sloping depositional surface) foreset deposits. These deposits will downlap into horizontal bottomset facies consisting with silty mud along with turbiditic sands, A_4. If the Glacier move across the fan top, the sub-unit A_2 may be present as a sub horizontal layer (Lønne, 1993).

The B-units are deposits formed when the glacier is standing still or retreating. These facies may be similar to the A-units. The sediment will be coarse grained and may have a high content of sub-glacially derived debris and ice rafted debris (Lønne, 1993).

The D-units are mainly deposited by the hyperpycnal meltwater plume, when the glacier terminus is retreating. Hyperpycnal flow is defined as a flow where the density of the suspended sediment flow is more than that of the water (Bates, 1953). This may result in a deposition consisting of very fine sand. The D-units tend to drape the front and back slope.

During the retreat of the glacier, an uplift of the submarine fan called *"post glacial isostatic uplift"* may occur. This is where the E-units are formed. This uplift may result in a reworking and resedimentation of the original sedimetns. Again, this can result in shoreline facies on the proximal and distal sides of the deposit. These four processes can be repeated if the glacier re-advance and retreat in a cyclical pattern. Such a repetition of the processes may make the sedimentary structure of the deposit very complex (Lønne, 1993).

Sørensen interpreted the ridge earlier than Melø, and Melø is relying much of his thoughts on these interpretations. A north to south cross section of the Svelvik ridge as interpreted by Sørensen is displayed in Figure 3.6. The cross section is following the same colour system as in Figure 3.1.

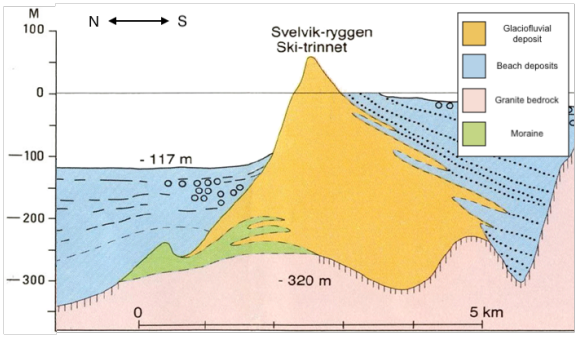

Figure 3.6: North-South Cross section of the Svelvik ridge Sørensen (1981)

Sørensen (1981) stated that for a glacier to halt, a preexisting bedrock threshold or moraine should be present. The pink top to the south in Figure 3.6 could work as a thresh-

old to halt the glacier. (Sørensen, 1981) The green area under the yellow glaciofluvial deposit and the blue marine deposits, indicates a preexisting moraine. This moraine could have served as a threshold for the advancing glacier, and were probably formed by the oscillating glacier front. As mentioned previously, scattered moraines can be found in the area, and Melø (2011) propose that this indicatie this oscillation. This advancing and retreating front have resulted in a complex sedimentary structure at the Svelvik ridge.

Further, Sørensen et al. (1990) states that. Due to the isostatic rebound caused by the deglaciation, the original deposits were exposed to air around 7000 years ago. This exposure introduced erosional forces in form of rivers, wave and tidal action. There is found evidence of wave action up to 197 m above sea level, implying the marine limit in the area. The tidal current has later divided the upper part of the deposits into an eastern and a western part. Sørensen et al. (1990)

Melø (2011) states that there are thought to be two existing aquifers present at the Svelvik ridge, an upper and a lower. An aquifer is described as a formation, a part of a formation or a group of formations that contains water saturated permeable material. The volume of water in the formation should be sufficient to yield economic quantities to wells. Layers or units that separate the aquifer from other geological formations are often referred to as aquitards or confining beds. These hinders the flow of water, due to very low permeability. The upper aquifer has the groundwater table as an upper limit, and a confining layer as a lower limit, below the confining layer there may be a confined aquifer.

Sørensen's interpretations were made when very little data were present, and Melø (2011) build much of his geological interpretation on this. During the previous CO_2 Field Lab project, various geophysical measurements were conducted at the site, giving valuable information about the the geology on site, the depositional environment and the aquifer systems.

3.1.1 New Information From the CO_2ield Lab Project

During the previous CO_2 Field Lab project, two deep wells were drilled and logged. Svelvik #1 drilled down to 333m, and Svelvik #2 drilled down to 90m. Both wells were logged with a range of tools, including conductivity, formation velocity, gamma ray counts, temperature and readings from a caliper tool. Based on the gamma ray, a clay content log was calculated. The clay content versus depth can be seen on figure 3.7.

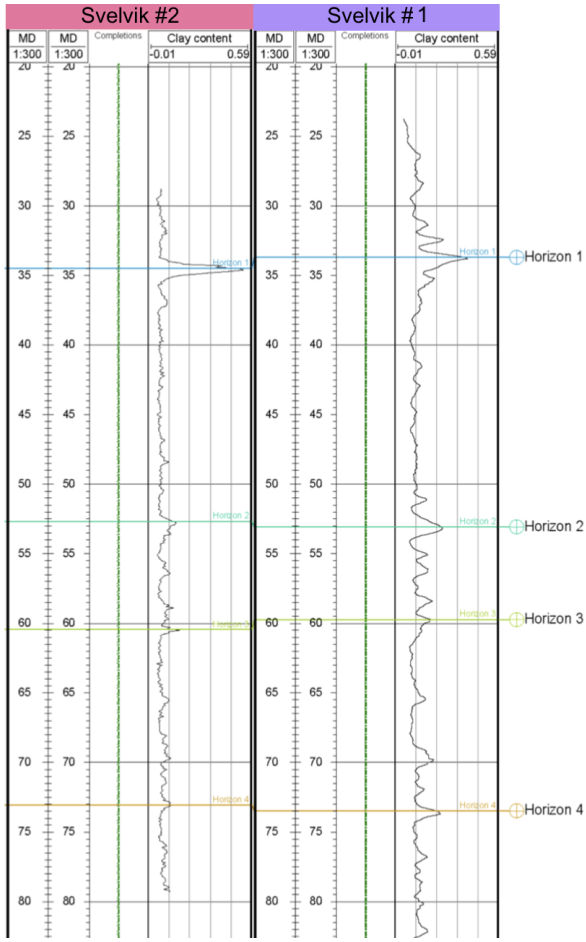

Figure 3.7: An excerpt from the clay content log of the two deep wells at the Svelvik Ridge (Grimstad, 2013).

When investigating these logs, one can notice a clear signal at about 35 m. This is interpreted as the transition from sand-dominated glaciofluvial sediments to the more clay-dominated deposits below. The correlating similarities between the two logs with depth is

taken as an indication of fairly horizontal layering, given the separation of 10 m between the two wells. With these logs and a digital geomodel created by the French Geological Survey (BRGM) based on seismic surveys conducted at the Svelvik ridge from 2010, a revised version of the geological model was created. In Figure 3.8 a cross section of the new geomodel is compared to the traditional created by Sørensen (1981).

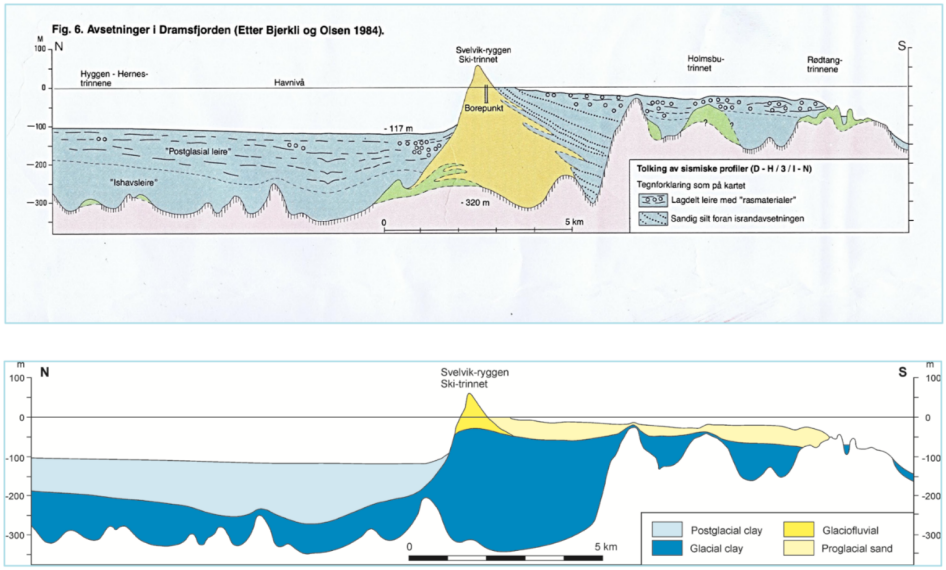

Figure 3.8: Geological model from (Sørensen, 1981)(top), and the new interpretation after results in the CO_2 Field Lab project (bottom) (Grimstad and Polak, 2013).

The glacial clay marked in dark blue in Figure 3.8 illustrates that more muddy layers are introduced. A more detailed illustration is showed in Figure 3.10. With the data from the Svelvik CO_2 Field Lab, it is now more relevant to interpret the deposits on the Svelvik Ridge as a mixture of Lønne's models for ice-contact glaciomarine systems, shown in Figures 3.2-3.4. This mixture caused by the recession and readvancement of the glacier results in a heterogeneus system. When sediments were deposited on the Svelvik ridge, clinoforms were formed. A clinoform can be defined as a sloping depositional surface of a major morphological feature as seen in Figure 3.9.

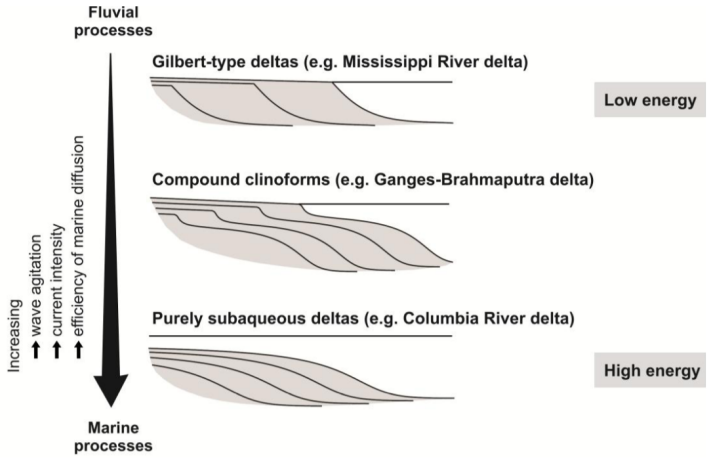

Figure 3.9: Trends in clinoform geometry in response to the ambient energy regime (Röhnert, 2016).

As seen from Figure 3.9 the trends in the clinoform geometry is a function of energy in the system (Röhnert, 2016). Since the deposits on the Svelvik Ridge might be deposited in different environments, a combination of Lønne's models, there will be different trends in the clinoforms on the site. A common feature of the clinoforms is the sloping trend. This trend might also result in lateral layering as well as vertical layering. This layering will presumably result in a reduced cross-layer permeability, hence an permeability anisotropy. As can be seen in Figure 2.6, the ridge is east-west running. This means that the progradating clinoforms were formed in the north-south direction. This anisotropy and its effect on the injection will be investigated through simulations that are described later in this thesis. Other geological features that assumably are present at the ridge and affects the anisotropy are cross-bedding and flooding surfaces.

Several intervals in the Svelvik #1 well shows a larger fraction of coarser sand and may represent extended bodies of sediments where gas, air or CO_2, could be injected. These bodies can be seen on figure 3.10 in yellow. The two wells on the figure are the Svelvik #1 and #2, where Svelvik #1 is the deepest. It is now planned to inject CO_2 in a body consisting of coarser sand found on 65 m deep in the Svelvik #2 well, marked with a black "*X*" in Figure 3.10. A pumping test was conducted at this depth, and the interval was found to be applicable for injection. These permeability values are used in the original geomodel and in the simulations conducted in thesis.

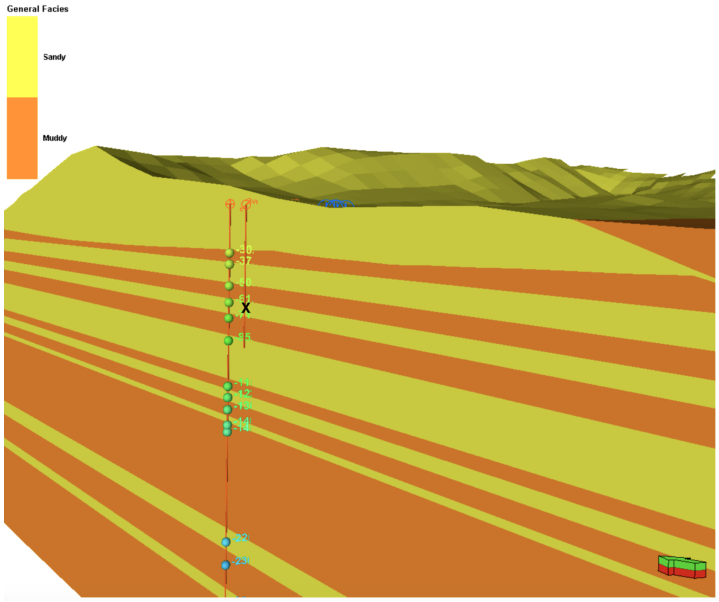

Figure 3.10: Geomodel showing general facies versus depth. Svelvik #1 well on the left, Svelvik #2 well on the right. Grimstad (2013)

The transition from the sand-dominated glaciofluvial sediments to the more clay-dominated deposits at 30m can be seen in Figure 3.10 as orange, "muddy" layers are introduced.

3.1.2 Assumed Geology in Previous Simulations

To create a consistent framework for modelling work, SINTEF has created a digital geomodel using the Petrel tool (Grimstad and Polak, 2013). As input, data from various monitoring surveys were combined. The data collection campaigns that were imported into the shallow geomodel are listed below:

- Bitmap images of interpreted Ground Penetrating Radar (GPR) data. The GPR survey were conducted by Norwegian Geotechnical Institute (NGI)
- Inverted radar velocities from the cross-well GPR data sets recorded by (BRGM). Data from before, during and after the shallow CO_2 injection were recorded and used as input in the model. Along with these, the calculated ratio of repeat to baseline velocities, were placed as properties in a 3D grid.
- Shallow gas concentration and flux data sets recorded by British Geological Survey (BGS). Data from before, during and after the shallow CO_2 injection were recorded and used as input in the model.

- Inverted resistivities from the Automated time lapse electrical resistivity tomography (ALERT) cube data measured by BGS before, during and after the shallow CO_2 injection, along with the calculated resistivity ratios are placed as properties in a 3D grid.
- Baseline resistivity data from the measurements in the ImaGeau and Geosciences Montpellier wells.
- Well trajectories of most wells used for CO_2 injection and for monitoring equipment.
- Bitmap images of surface features from various map services
- Surfaces and horizons from the BRGM 3D geolmodel
- Bitmap images from the first migration of the data from the 2D seismic survey in 2010
- Seismic velocity profiles and migrated images after the reprocessing of the 2010 seismic
- The trajectory of two deep wells (333m and 90m deep) and the corresponding well logs recorded in the wells Grimstad (2013).

Since the Svelvik ridge is located in the south of Norway, UTM32 was chosen as the common reference system.

The resulting Petrel model is the one presented in Figure 3.10. A few simplified tentative models were also created; including a dipping model, a model with low permeability in the sealing layer, high permeability in the sealing layer and a ”hole” in the sealing layer. All these petrel models were exported into Eclipse, where an air injection was simulated at 65m depth. In this thesis, the effect of hysteresis and specific relative permeability curves allocated to specific layers will be investigated. The results of the updated simulations will be compared to the original simulations.

3.1.3 The Effect of Anisotropy

In conjunction with the continuation of the CO_2 Field Lab project, Anja Sundal from the Department of Geosciences at UiO were asked to create a new and updated, digital geomodel of the Svelvik Ridge. The digital model will be a Petrel model, designed to be an input to the simulations conducted in the reservoir simulator Eclipse. When the model is finished, it should be compared to the results of this thesis and observations from future injection tests. This is discussed in ”Further work”. To test the effect of

anisotropy, simulations in the existing model was conducted. In this setting, anisotropy implies different permeability in different directions of the reservoir. According to the description in Chapter 3.2. Simulations were conducted with reduced permeability from north to south, from east to west, and in the vertical direction of the reservoir.

The earlier model shown in Figure 3.10 is a typical layercake model, where the layering is based on the information from the well logs. Anja Sundal is working on a model where the anisotropy is included, and the layering of the model is more realistic according to the interpretation of the geology on the site. A screenshot of the potential model is shown in Figure 3.11.

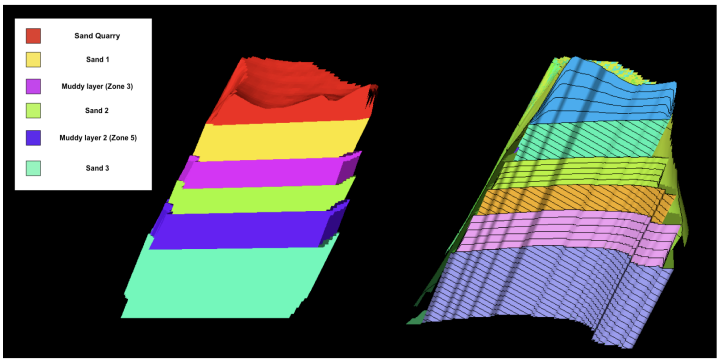

Figure 3.11: Suggested geomodel by Sundal (2017), with dipping layers of sands, simulating clinoforms. Model grid on the right, facies on the left.

Through geological pollen analysis conducted at UiO for the Svelvik CO_2 Field Lab, it is planned to find out more about the age of the deposits, and thereby the depositional environment for the different facies at the ridge.

Another aspect of the geology of the Svelvik ridge is the grain size distibution and its effect on the relative permeability of CO_2 and water.

3.2 Grain Size Distribution and Relative Permeability

Corey and Brook's equations describing the relative permeability of a two phase system are dependant on the grain size distribution. Hence, it would be interesting to investigate if there would be a significant change in the simulation results if the relative permeability curves were implemented as a function of grain size distribution, λ.

To get a grasp of the grain size distribution with depth, a selection of samples (cuttings), has be analysed with regard to their grain distribution. The instrument used was a Coulter LS 230 and the technique is based on laser diffraction. The output of the instrument is a high resolution grain size distribution from clay to coarse sand. The laboratory work was carried out by senior engineer Irene Bragstad at "SINTEF Materialer og kjemi". 11 samples that could give a general understanding of the lithologies present in the well were selected. This was followed up by running 10 new samples covering three interpreted sand horizons. These horizons are 61,5 – 72 m, 122 – 131 m, and 249 – 262 m. Finally 6 samples were run to cover two more sand horizons at 85 – 115 m, and at 220 -236 m (Rendall, 2012). The table in Figure 3.12 shows the resulting grain size distribution versus depth.

From figure 3.7 one can see the similarities between Svelvik #1 and #2, hence it is assumed that this grain size distribution is valid for both Svelvik #1 and #2.

Depth (m)	Clay (%)	Silt(%)	Very fine sand (%)	Fine sand (%)	Medium sand(%)	Coarse sand (%)	Very coarse sand (%)	Grain>1.7 mm(% of total sample)
37,5	8,9	48,9	7,1	4,2	6,0	12,6	12,4	16,5
54,5	12,4	50,7	14,3	9,7	3,8	8,0	1,1	14,8
59,5	1,7	8,8	24,1	31,6	12,9	11,8	9,0	7,2
64,5	0,3	11,2	8,6	21,1	34,3	12,6	11,9	10,2
65,5	0,6	21,5	4,2	5,5	16,4	22,2	29,7	3,9
68,5	0,3	4,1	3,5	9,9	29,8	25,9	26,6	1,3
69,5	0,2	4,9	1,2	3,2	16,8	22,3	51,5	50,2
71,5	14,3	57,7	13,7	5,8	2,8	4,9	1,0	6,2
80,5	14,4	53,9	12,3	9,0	5,2	3,8	1,5	2,1
100,5	2,2	10,4	5,2	14,2	19,5	18,4	30,2	3,6
110,5	1,7	8,8	24,1	31,6	12,9	11,8	9,0	0,0
126,5	3,9	13,0	4,6	8,4	13,2	22,7	34,1	12,6
127,5	2,9	13,7	5,0	7,8	11,4	24,4	34,7	20,1
128,5	6,7	24,1	9,4	14,0	19,8	18,6	7,5	0,4
150,5	12,9	53,6	12,6	11,9	7,6	1,4	0,0	0,2
191,5	19,1	66,4	9,2	3,0	2,3	0,0	0,0	0,6
210,0	3,5	16,1	13,9	26,6	32,2	7,3	0,4	0,0
221,5	4,0	14,6	15,6	22,1	25,8	13,5	4,5	0,5
229,5	2,7	9,6	7,1	17,6	40,6	19,9	2,5	0,5
235,5	16,0	61,1	10,0	5,7	4,4	2,7	0,1	0,0
249,5	6,8	27,4	19,8	16,8	15,8	8,9	4,5	2,4

Figure 3.12: Grain size distribution versus depth (Rendall, 2012).

The grain size distribution of the sediment can give an indication of deposition environment and the sorting of the sediment. It can give an indication of the quality of the sealing formation and the reservoir rock. As mentioned previously, this information can

also be used to calculate relative permeability curves for different layers by using Corey and Brooks equations.

Corey and Brooks (1964) stated that the relative permeability is a function, not only of saturation, but also of the grain size distribution. The relative permeability for the wetting phase $k_{r,w}$ is given by:

$$k_{r,w} = \frac{(S_w - S_{wr})}{(1 - S_{wr})}^{\frac{2+3\lambda}{\lambda}} \tag{3.1}$$

and the non-wetting relative permeability, $k_{r,nw}$ by:

$$k_{r,nw} = \left(\frac{1 - S_w}{1 - S_{wr}}\right)^2 \left[1 - \left(\frac{S_w - S_{wr}}{1 - S_{wr}}\right)^{\frac{2+\lambda}{\lambda}}\right] \tag{3.2}$$

Where:

$k_{r,w}$ = Wetting phase relative permeability
$k_{r,nw}$ = Non-wetting phase relative permeability
S_w = Wetting phase saturation
S_{wr} = Wetting phase residual saturation
λ = Grain Size Distribution Index

In the previous simulation model, the confining layer was assumed to be impermeable. Hence, when injectiong CO_2 under this cap rock, it could be assumed that the gas would only flow in one layer. Therefore, only one set of relative permeability curves was needed in the simulation model. In this thesis, the possibility of migration through the confining layer and migration patterns throughout the formation was investigated, by relating different relative permeability curves to the different layers of the model, as a function of the grain size distribution. Figure 3.13 shows the relative permeability curves that were retrieved from previous simulation works.

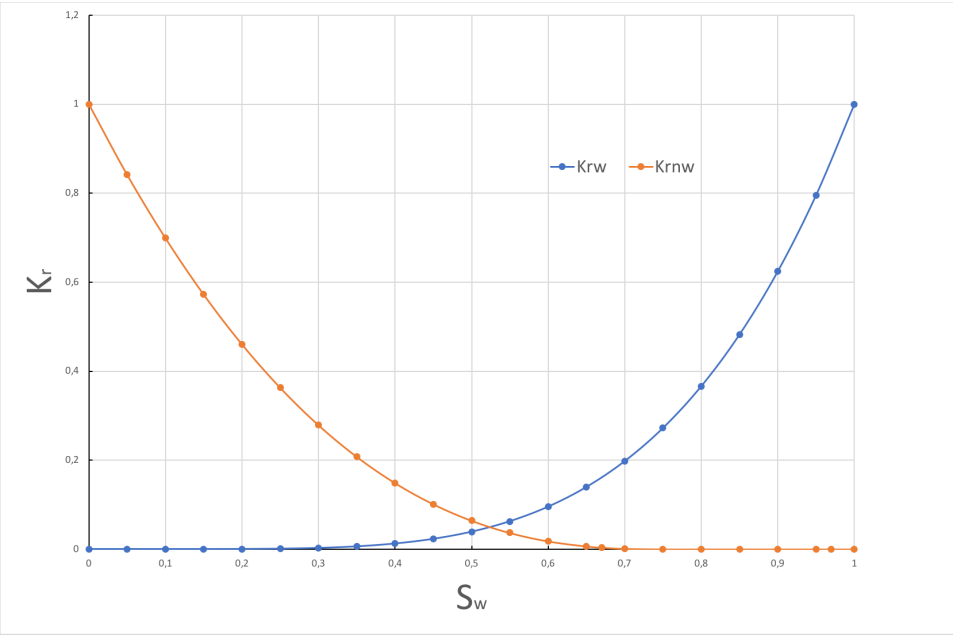

Figure 3.13: Relative permeability versus water saturation, as original input (Grimstad, 2013).

The water is the wetting phase, while CO_2 is the non-wetting (nw) phase. The curves in this figure were calculated by using Corey and Brook's equation, with end point saturations of 0.25 and 1.0 and an exponent of 2.5 for the gas, and end point saturations of 0.1 and 1.0 and an exponent of 4 for the water. For simplicity, the functional term of Equation 3.1 were used both for the wetting and non-wetting phase.

By using the values displayed in Table 3.1, and the Corey and Brook's equations, new relative permeability curves have been calculated. These curves are displayed in Figure 3.14.

Table 3.1: Grain Size Distribution Index, for Different Porous Media (Assouline, 2005).

Type	**Grain size distribution index, λ**
Unconsolidated Sand	3,7
Silt	1,82
Sandy Clay	0,81
Consolidated Sand	2,29

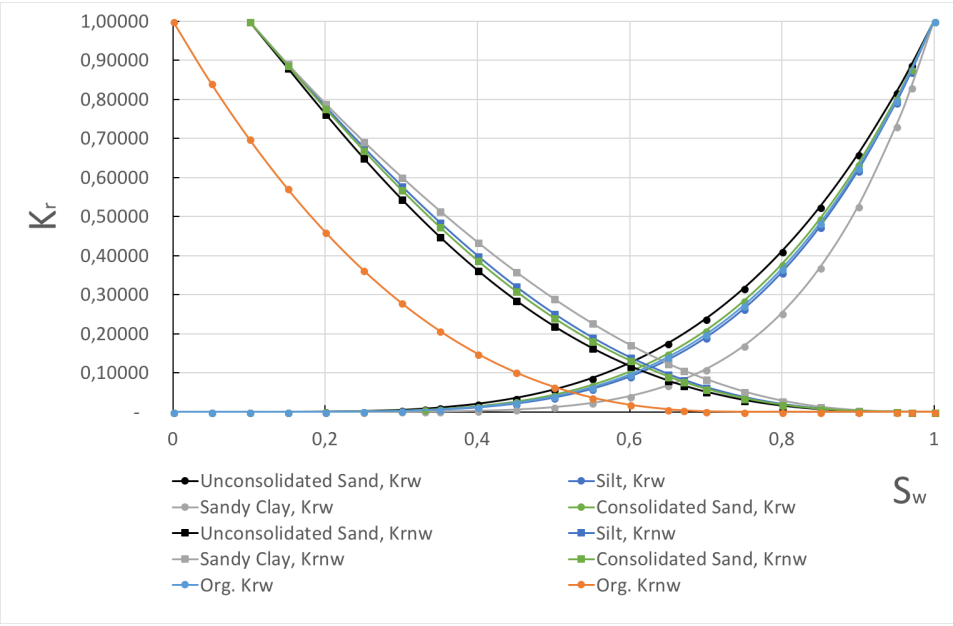

Figure 3.14: Drainage, Relative permeability versus water saturation curves.

When comparing the new relative permeability curves to the curves used as input in the original model in Figure 3.14, one can see that the difference lies in the relative permeability of the non wetting phase, CO_2. Since the original relative permeability model was calculated by using a simplification, where the functional term of Equation 3.1 was used both for the wetting and non-wetting phase, a deviation in the relative permeability for the wetting phase occurs. This inequality is mainly resulting in a lower residual trapping of the injected CO_2 in the new model.

3.3 Relative Permeability Hysteresis in Porous Media

The relative permeability of a fluid is a function of saturation. When the water saturation in a reservoir increases, the relative permeability of the water will increase. The response of the increase in saturation will depend on whether the system is in a drainage state or in an imbibition state. The state of the system affects the relative permeability. Not only is the system dependant on the current state, but also on its previous history. The result is that the relative permeability is not only a function of saturation, but also the history of the system. This dependence on the history of the systems, is called hysteresis. Capillary pressure is also dependant on the history of the system, and will therefore exhibit hysteresis behaviour

when plotted against saturation. To illustrate the effect of of hysteresis, one can compare the drainage and imbibition curves (often called bounding curves) for the non-wetting phase. Relative permeability plotted against saturation of the wetting phase as shown in Figure 3.15.

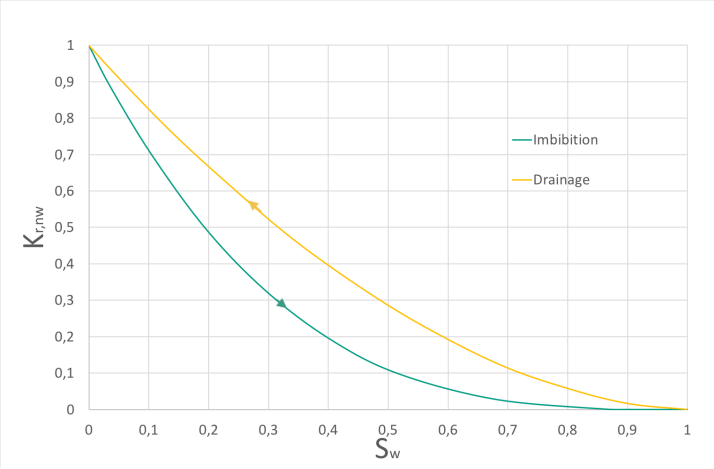

Figure 3.15: Drainage and imbibition curves for the non-wetting phase, versus saturation of the wetting phase. Notice that the saturation on the x-axis is normalized, and that Sw = 0 starts at Swi, (Schaerer et al., 2006a).

This simple illustration shows that the state of the system has a distinct effect on the relative permeability of the fluids. In the CO_2 Field Lab project, the injected CO_2 pushes the wetting phase (in situ water/brine) out of the pores in a drainage process. Therefore, the drainage curves where initially used in the simulations.

When following the drainage curve shown in Figure 3.15, one can see that the relative permeability of the CO_2 starts to increase at a much lower non-wetting saturation than the imbibition curve.

This only a valid situation when CO_2 is displacing the water during injection. When the injected CO_2 starts to migrate due to buoyancy, water will start to imbibe back into the pores. During this process, the relative permeability will follow the imbibition curve. This is illustrated in Figure 3.16.

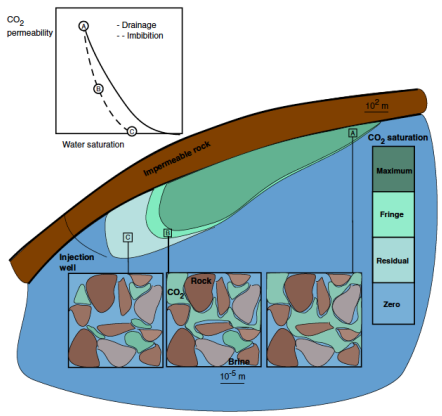

Figure 3.16: A sketch of key processes governed by capillary trapping after CO_2 injection has ceased at a storage site (Krevor et al., 2015).

The pores in ”point A” in Figure 3.16, are now filled with CO_2 in the middle, while water clings to the corners and roughness of the pore space. This is illustrated further in Figure 3.17 at step t_1 where the CO_2 is marked with green, and water is marked with white. The water clinging to the roughness of the pore space is not a thin film, but bulk volumes of water that are often referred to as ”wetting layers”. When the water imbibes back into the pores, the wetting layers will start to swell as the capillary pressure decreases. The narrowest part of the pore is often called a ”pore throat” marked with x in the figure. Eventually, in the narrowest part of the pore throat, during the swelling of the wetting layers, an advancing angle is reached and the wetting layers will move towards each other until contact occurs. This is a very unstable condition, and water will rapidly fill the pore throat as in t_2 in Figure 3.17. This rapid filling of the pore throat is called a snap-off (Blunt, 2017). As shown in Figure 3.17, this mechanism will trap the CO_2 in the pore. This has happened in region C in Figure 3.16.

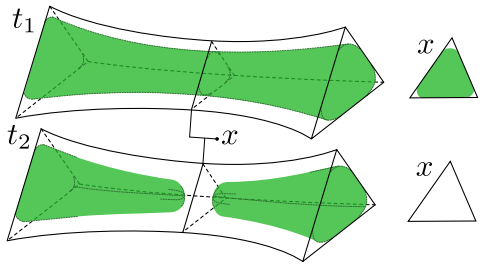

Figure 3.17: Illustration of the process behind ”snap-off” (Torland, 2018).

Since the pores represent the main volume in the rock, large amounts of CO_2 can be trapped in the formation by snap-off. Since snap-off is mainly caused by the imbibition process, and that snap-off is one of the main mechanisms causing residual- or capillary trapping, it is important that the reservoir simulation takes this into account. By including hysteresis and the possibility of both drainage and imbibition processes in the simulation, the capillary trapping of CO_2 can be described.

There are many models used to describe hysteresis, and the hysteresis model presented by Killough and Carlson are the best known in the industry.

3.3.1 Carlson

The model proposed by Carlson in 1981 focus on the relative permeability of the non-wetting phase, which in our case is CO_2. The model describes a two phase system, and assumes that the relative permeablity of the wetting phase shows no hysteric behaviour. Carlson proposes that the relative permeability of the non-wetting phase follow two bounding curves: the primary imbibition curve, and the primary drainage curve. According to Land (1968b), it is assumed that trapping only occurs during imbibition. Therefore it is also assumed that if the imbibition process is reverced, the imbibition curve will be retraced exactly. Hence, the model is based on different imbibition curves as shown in Figure 3.18.

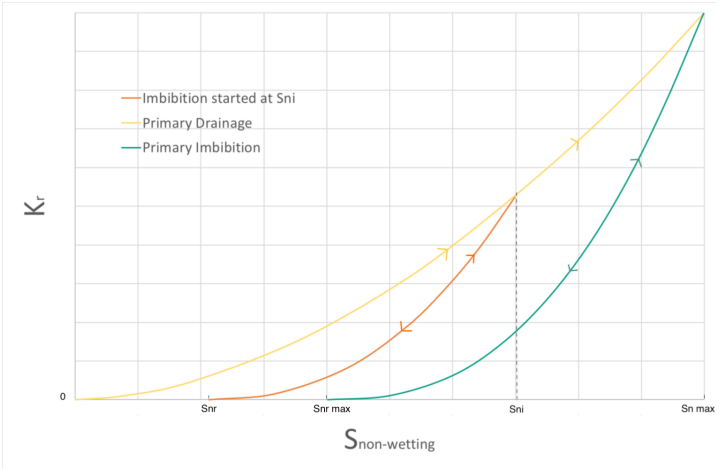

Figure 3.18: Bounding curves, relative permeability of the non-wetting phase plotted against the saturation of the non-wetting phase with two imbibition curves for illustration. The drainage curve is being reversed in S_{ni} Carlson et al. (1981).

$S_{nw,t}$ is the trapped saturation of the non-wetting fluid that was discussed previously.

$S_{nw,f}$ is the free saturation so that: S_{nw}=$S_{nw,t}$+$S_{nw,f}$. Carlson states that the imbibition curve can be predicted by using the drainage curve and adjusting for trapping. Hence, the values of the imbibition curve, k^I_{nw}, must be equal to the values of the drainage curve evaluated at free saturation:

$$k_n^I(S_{nw}) = k_n^D(S_{nwf}) \tag{3.3}$$

Meaning that if there are no trapping present, the imbibition curve would be identical to the drainage curve. At the beginning of the imbibition, S^{max}_{nw}, the drainage and imbibition curves are equal, as no trapping has taken place yet. As the imbibition process moves on, the amount of trapping will increase and the curves will grow further apart. This means that to obtain the imbibition curve, the value of $S_{nw,t}$ needs to be known. From Figure 3.18 one can see that the higher the starting S_{nw} when the drainage process is reversed, the larger the residual saturation caused by trapping will become.

Land (1968a) formulated a relation between the saturation at which drainage is reversed ($S_{nw,i}$ in Figure 3.18) and the irreducible saturation $S_{nw,r}$.

$$\frac{1}{S_{nr}} - \frac{1}{S_{ni}} = C \tag{3.4}$$

Where C is a constant.

The value of the free saturation $S_{nw,f}$ is a function of C, S_{nw} and $S_{nw,r}$. By looking at Figure 3.18 one can see that $S_{nw,t}$ = 0 when S_{nw} = $S_{nw,i}$, and that $S_{nw,f}$ = 0 when S_{nw} = $S_{nw,r}$. For any other value where
$S_{nw,i} > S_{nw} > S_{nw,r}$, the distribution S_{nw} between $S_{nw,t}$ and $S_{nw,f}$ can be determined by Equation 3.4. At S_{nw}, $S_{nw,t}$ has been trapped. At this point more of the free saturation can still be trapped, according to Equation 3.4. The amount of $S_{nw,f}$ that is yet to be trapped, $S_{nw,fr}$, can be determined by $S_{nw,f}$ for $S_{nw,i}$ and $S_{nw,fr}$ for $S_{nw,r}$ in Equation 3.4 so that Equation 3.5 is obtained:

$$S_{nw,fr} = \frac{S_{nw,f}}{1 + CS_{nw,f}} \tag{3.5}$$

The trapped saturation, $S_{nw,t}$, will eventually reach a maximum when it is equal to $S_{nw,r}$. At this moment, the trapped saturation can be defined as the future total trapped saturation minus the saturation yet to be trapped: $S_{nw,t}$ = $S_{nw,r}$ - $S_{nw,fr}$. The saturation yet to be trapped, S_{nfr}, is described by Equation 3.5. By inserting this, the following expression is obtained:

$$S_{nw,t} = S_{nw,r} - \frac{S_{nw,f}}{1 + CS_{nw,f}}$$

The trapped saturation $S_{nw,t}$ was originally defined as $S_{nw,t}$ = S_{nw} - $S_{nw,f}$. By using this definition, the equation becomes:

$$S_{nw} - S_{nw,f} = S_{nw,r} - \frac{S_{nw,f}}{1 + CS_{nw,f}}$$

Finally, by solving for S_{nf} yields:

$$S_{nw,f} = \frac{1}{2}\left[\quad (S_{nw} - S_{nw,r}) + \sqrt{(S_{nw} - S_{nw,r})^2 + \frac{4}{C}(S_{nw} - S_{nw,r})} \quad \right] \tag{3.6}$$

With Equation 3.6 the free non-wetting saturation can be obtained at any given moment. The value of $S_{nw,f}$ can be used to predict the unknown imbibition curve from the empirically known drainage curve.

Before that, the constant *C* has to be estimated. To do this, $S_{nw,r}$ has to be known. In practise measurements of $S_{nw,r}$ are difficult to obtain, therefore a procedure to calculate it without experimental determination is followed. The $S_{nw,i}$ is assumed to be known exactly, and let $S_{nw,j}$ be N experimental imbibition data points. The $S_{nw,j}$ is then their respective free saturation. By substituting Equation 3.4 into Equation 3.6, the equation for $S_{nw,r}$ becomes:

$$S_{nwr_j} = \frac{1}{2}\left[\quad S_{nw_j} - S_{nw,f_j} + (S_{nw_j} - S_{nw,f_j})^2 + \sqrt{\frac{4S_{nw,i}S_{nw,f_j}(S_{nw,i} - S_{nw,f_j})}{S_{nw,i} - S_{nw,f_j}}} \quad \right] \tag{3.7}$$

To get a representative value of $S_{nw,r}$, a value is computed for every data point *j*, and then the average value is computed by:

$$\overline{S}_{nw,r} = \frac{1}{N}\sum_{j=1}^{N} S_{nw,r_j}$$

Once $\overline{S}_{nw,r}$ is obtained the constant *C* can be calculated with Equation 3.5. With this constant and the same equation, $S_{nw,r}$ for any given $S_{nw,i}$ can be obtained. By using Equation 3.6, $S_{nw,f}$ can be determined and hence the imbibition curve.

An important aspect of this method is that the process requires an exact knowledge of the primary drainage curve, the point $S_{nw,i}$ and at least one experimental value of $S_{nw,j}$ in the imbibition curve.

Carlson assumes that there are no hysteric behaviour in the relative permeability of wetting phase, but there are models describing this phenomena. Land proposes the following equation for the relative permeability of the water when trapped gas is present in the pores:

$$k_{rw} = \frac{S_w^{*2} \int_0^{S_w^*} \frac{dS_w^*}{P_c^2}}{\int_0^1 \frac{dS^*}{P_c^2}} \tag{3.8}$$

Where the capillary pressure, P_c, is a function of the fraction of the effective pore space, S*. The effective water saturation, S_w^* is given by:

$$S_w^* = \frac{S_w - S_{wr}}{1 - S_{wr}}$$

To solve the integral, Land expressed P_c as a function of S_w^*, the imbibition capillary pressure curve, and S_w^* were treated as a function of S*. Since S* is the sum of the water saturation, S_w^*, and the trapped gas saturation, S_{gt}^*, Equation 3.8 can be written as:

$$k_{rw} = \frac{S_w^{*2} \left[\int_0^{S_w^* + S_{gt}^*} \frac{dS^*}{P_c^2} - \int_0^{S_{gt}^*} \frac{dS_{gt}^*}{P_c^2} \right]}{\int_0^1 \frac{dS^*}{P_c^2}} \tag{3.9}$$

S_{gt}^* is given by:

$$S_{gt}^* = S_{gr}^* - \frac{S_{gF}^*}{1 + C S_{gF}^*}$$

This equation can be written in terms of S^*, since S_{gF}^*=1-S^*. This substitution results in an equation which, when differentiated, yields:

$$S_{gt}^* = \frac{(S_{gr}^*)_{max}^2 \cdot dS^*}{\left(1 - \left[1 - (S_{gr}^*)_{max}\right] S^*\right)^2} \tag{3.10}$$

Where $S_{gr_{max}}^*$ is the residual effective gas saturation left in the sand after completion of an imbibition cycle. A substitution of Equation 3.10 into Equation 3.9 yields:

$$k_{rw} = S_w^{*2}\left(\frac{\int_0^{S_w^*+S_{gt}^*}\frac{dS^*}{P_c^2}}{\int_0^1\frac{dS^*}{P_c^2}} - (S_{gr}^*)_{max}^2\frac{\int_{S_{wi}^*}^{S_w^*+S_{gt}^*}\frac{dS^*}{\left(1-\left[1-(S_{gr}^*)_{max}\right]S^*\right)^2P_c^2}}{\int_0^1\frac{dS^*}{P_c^2}}\right) \tag{3.11}$$

Whit integration, Equation 3.11 becomes:

$$k_{rw} = S_w^{*4} + S_w^{*2}\left[\left(2S_w^* + S_{gt}^* - \frac{2}{1-(S_{gr}^*)_{max}}\right)S_{gt}^* - \frac{2}{C^2}ln\frac{(S_{gr}^*)_{max}^2(S_w^*+S_{gt}^*)}{S_{gt}^*}\right] \tag{3.12}$$

This equation can be generalized as k_{rw}^I=k_{rw}^D+$f(S_w^*)$, where $f(S_w^*)$ is the last term of the equation. It is the difference between the drainage and imbibition relative permeability, caused by the redistribution of water in the pores (Land, 1968a). The function $f(S_w^*)$ is different for each pore size distribution. This can make it possible to assign imbibition relative permeability curves for the wetting phase to different layers of the model. This will be discussed under *Implementation* and *Further Work*.

Killough's method is equally famous This is a simpler model that acquire more input data. Also, similar to Land, Killough proposed a solution for the effect of trapping on the wetting phase.

3.3.2 Killough

Identical to Carlsons proposal, Killough assumes that the trapping occurs only in the imbibition phase (Killough et al., 1976). The imbibition curves are then retraced exactly until it reaches the primary drainage curve when reversed. This is similar to what is illustrated in Figure 3.18. From this graph, one can see that $k_{nw}^I(S_{nw,i})$ = $k_{nw}^D(S_{nw,i})$, and $k_{nw}^I(S_{nw,r})$ = 0. To find the intermediate curve lying between $k_{nw}^I(S_{nw,r})$ and $k_{nw}^I(S_{nw,i})$, Killough consider two methods: parametric interpolation and normalized experimental data.

By using parametric interpolation, Killough obtained the following expression:

$$k_{nw}^{I}(S_{nw}) = k_{nw}^{D}(S_{nw,i})\left(\frac{S_{nw} - S_{nw,r}}{S_{nw,i} - S_{nw,r}}\right)^{\lambda} \tag{3.13}$$

Where λ is a given parameter. It is obvious that this fulfills $k_n^I(S_{ni}) = k_n^D(S_{ni})$ and $k_n^I(S_{nw,r}) = 0$. To obtain the corresponding $S_{nw,r}$, the constant *C* has to be computed by using Equation 3.4, or Killough's version:

$$C = \frac{1}{S_{nw,r}^{max}} - \frac{1}{S_{nw,i}^{max}}$$

This approach requires measuring $S_{nw,r}^{max}$, which can be difficult to implement. The alternative method is to use normalized experimental data i the following expression:

$$k_{nw}^{I}(S_{nw}) = k_{nw}^{D}(S_{nw,i})\left(\frac{k_{nw}^{I^*}(S_{nw}^{*}) - k_{nw}^{I^*}(S_{nw,r}^{max})}{k_{nw}^{I*}(S_{nw}^{max}) - k_{nw}^{I*}(S_{nw,r}^{max})}\right) \tag{3.14}$$

Where $k_{nw}^{I^*}$ is the analytical primary imbibition curve, and S_{nw}^{*} is given by:

$$S_{nw}^{*} = \left(\frac{(S_{nw} - S_{nw,r})(S_{nw}^{max}) - S_{nw,r}^{max}}{S_{nw,i} - S_{nw,r}}\right) + S_{nw,r}^{max} \tag{3.15}$$

For this method it is assumed that both the imbibition curve and the drainage curve are known, at least empirically. Killough also proposed a solution for the effect of trapping on the wetting phase. The solution follows the same idea as the one for the non-wetting phase, and the interpolation between $k_w^{I^*}(S_{nw,i})$ and $k_w^{I^*}(S_{nw,r}^{max})$ os given by:

$$k_w^I(S_{nw}) = k_w^D(S_{nw,i})\left(\frac{k_w^{I^*}(S_)^* - k_w^{I^*}(S_{nw,r}^{max})}{k_w^{I^*}(S_{nw,r}^{max}) - k_w^{I^*}(S_{nw}^{max})}\right)(k_w^I(S_{nw,r}) - k_w^D(S_{nw,i}) \tag{3.16}$$

Where $k_w^{I^*}$ is the analytical primary imbibition curve for the wetting phase, and S_{nw}^{*} is given by Equation 3.15.

The Killough and Carlson models are the most famous in the industry, but there are many other and newer proposals. Among these, there will be presented only one in this thesis, the Scanning Hysteresis Model.

3.3.3 The Scanning Hysteresis Model

This model, described in 2000, is based on data gathered from Gladfelter and Gupta and from Braun and Holland's experiments. One thing that stands out with this model, is that the relative permeability curves are different from those proposed by Land as you can be seen in Figure 3.19, (Gladfelter et al., 1980).

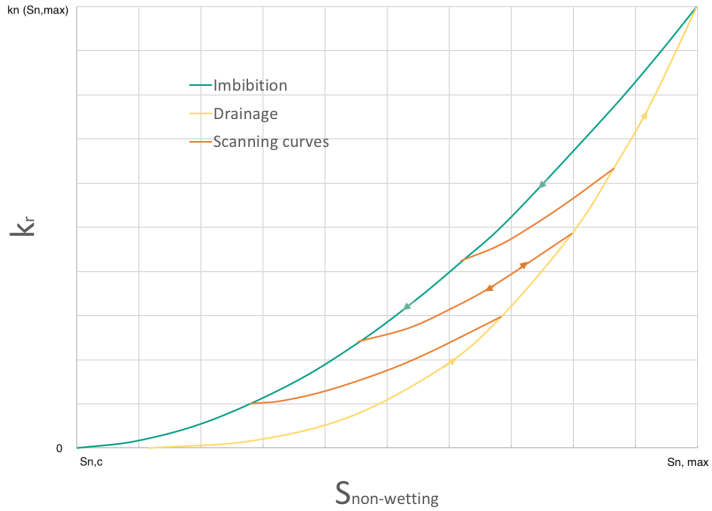

Figure 3.19: Bounding curves, relative permeability of the non-wetting phase plotted against the saturation of the non wetting phase. Illustration of bounding and scanning curves according to the Scanning Hysteresis Model. Adapted from Gladfelter et al. (1980)

Notice the difference from Lands proposal by comparing Figure 3.19 with Figure 3.18. The bounding curves have now inverted roles, and this helps us understand why there is no well-established model to describe the physical aspect of hysteresis. The scanning curves, marked in orange color in Figure 3.19 are used to move from one primary curve to the other when the primary process is reversed. If the process is reversed while on a scanning curve, the curve is retraced exactly. In this model, the boundary curves are assumed to be known exactly. A new parameter, π, is introduced to serve as a memory of the system so that k_n^S = $k_n^S(S_n, \pi)$. This is only a reference parameter, so values can be chosen arbitrarily.

When moving along a boundary curve, imbibition or drainage, the memory of the system changes. Hence the value of π will change. However, π will remain constant during a scanning process, until it reaches a boundary curve once again. It is important that π is modified so that when following a primary curve the following criteria are being fulfilled: $k_n^D(S_n) = k_n^S(S_n, \pi)$ and $k_n^I(S_n) = k_n^S(S_n, \pi)$.

The scanning curves, denoted with k_n^S, needs to be expressed. Schaerer et al. (2006b)

use the following choices, defined as functions of S = S_w :

$$k_{nw}^D(S) = (s-1)^\eta \qquad for \quad 0 \leq s \leq 1 \qquad and \quad when \quad \frac{\delta s}{\delta t} < 0$$

$$k_{nw}^I(S) = (s-1)^\theta \qquad for \quad 0 \leq s \leq 1 \qquad and \quad when \quad \frac{\delta s}{\delta t} > 0$$

Where $1 < \theta < \eta$, and in this region, the non-wetting relative permeability is chosen as:

$$k_n^S(S,\pi) = \frac{(1-\pi)^\varepsilon}{(1-\alpha\pi)^\zeta}(1-\alpha S)^\zeta \tag{3.17}$$

Where ε and ζ are shaping parameters. Schaerer et al uses $\theta = 2$, $\eta = 3$, $\varepsilon = 2$ and $\zeta = 1$ in their paper. Once π^D and π^I are defined, the convection-diffusion equation for the wet- ting phase:

$$\frac{\delta}{\delta t}(s_w) + \frac{\delta}{\delta x}(f_w) = \frac{\delta}{\delta x}\left[\epsilon \frac{\delta S_w}{\delta x}\right] \tag{3.18}$$

is modified to include the parameter π:

$$\frac{\delta S}{\delta t} + \frac{\delta}{\delta x}(f_w)F(S,\pi) = \frac{\delta}{\delta x}\left[\epsilon \frac{\delta S}{\delta x}\right] \tag{3.19}$$

Where S = S_w, ϵ is a small positive constant, and F is a funcion dependant on the state of the system. The following three functions represent F for drainage, imbibition and scanning, respectively:

$$\begin{aligned}
F(S,\pi) = f^D(s) &= \frac{k_w(S)/\mu_s}{k_w(S)/\mu_s + k_n^D(S,\pi)/\mu_n} \qquad when \quad \pi = \pi^D(s) \quad and \quad \frac{\delta s}{\delta t} < 0 \\
F(S,\pi) = f^I(s) &= \frac{k_w(S)/\mu_s}{k_w(S)/\mu_s + k_n^I(S,\pi)/\mu_n} \qquad when \quad \pi = \pi^I(s) \quad and \quad \frac{\delta s}{\delta t} > 0 \\
F(S,\pi) = f^S(s) &= \frac{k_w(S)/\mu_s}{k_w(S)/\mu_s + k_n^S(S,\pi)/\mu_n} \qquad when \quad \frac{\delta \pi}{\delta t} = 0 \quad otherwise.
\end{aligned} \tag{3.20}$$

The system is then provided with initial conditions or boundary conditions. Schaerer et al. (2006b) present Riemann solutions for this problem. In this thesis, the effect of relative permeability hysteresis will be studied by running simulations in Eclipse.

3.3.4 Hysteresis In Eclipse

The way in which the relative permeability hysteresis process is treated in Eclipse follows the techniques described by Aziz and Settari, Killough, Carlson, Land and Jargon. Jargon's method is an unpublished method, which is used only in Eclipse (Schlumberger, 2015). The method construct the trapped saturation, S_{ncrt}, by moving the drainage critical saturation towards the imbibition critical saturation by the same fraction that the hysteresis saturation has moved towards the maximum non-wetting saturation (Schlumberger, 2015):

$$S_{ncrt} = S_{ncrd} + \frac{(S_{ncri} - S_{ncrd})(S_{hy} - S_{ncrd})}{(S_{n,max} - S_{ncrd})} \tag{3.21}$$

Where S_{hy} the maximum non-wetting phase saturation reached in the run, S_{ncrd} is the critical saturation of the drainage curve, S_{ncrd} is the critical saturation of the imbibition curve and $S_{n,max}$ is the maximum stauration for the non-wetting phase where the drainage curve and the imbibition curve meet.

A function F(x), which represents the ratio of imbibition and drainage curves as a function of the saturation value scaled between the drainage curve end point and the maximum saturation, is defined as:

$$F(x) = \frac{k_{ri}(S_n)}{k_{rd}(S_n)} \tag{3.22}$$

Where x is defined as the function:

$$x = \frac{S_n - S_{ncrd}}{S_{n,max} - S_{ncrd}}$$

Here, x lies between 0 and 1 and F(x) goes from 0 at x = 0 to 1 at x = 1, where the two curves meet. If the drainage curve is always above the imbibition curve, F(x) also must lie between 0 and 1. The scanning relative permeability value is then constructed by multiplying the drainage curve value by the function F(x) , where F(x) is evaluated at an x-value which reflects the fractional distance of the current saturation between the drainage curve end point and the hysteresis saturation:

$$k_r n(S_n) = F(x_s) k_{rnd}(S_n) \tag{3.23}$$

Where x_s is given by:

$$x_s = \frac{S_n - S_{ncrd}}{S_{hy} - S_{ncrd}}$$

3.4 Limits and Assumptions of the Scenario Modelling and Simulations

In the CO_2 Field Lab project simulations, the injection gas was given the properties of air (N_2). In this thesis the objective is to simulate injection of CO_2, therefore new PVT input data had to be calculated. In addition to this, knowledge about the injection and production process and limiting factors was needed. To decide a maximum allowable water injection rate, the input bottom hole pressure limit in the previous simulations was considered. This limit was verified by calculating the fracture pressure of the formation. For the production case, the minimum allowable bottom hole pressure was considered.

3.4.1 PVT-data

The gas volume factor, B_g, is defined as the ratio of gas volume at a specified pressure and a specified temperature to the ideal gas volume at standard conditions (Whitson and Brulé, 2000).

$$B_g = \frac{p_{sc}}{T_{sc}} \frac{ZT}{p} \tag{3.24}$$

Where:

$B_g =$ Gas volume factor
$p_{sc} =$ Pressure at standard conditions. For customary units: p_{sc}= 14.7 psia
$T_{sc} =$ Temperature at standard conditions. For customary units: T_{sc}= 520°R
$Z =$ pV/nRT, the Z factor.
$T =$ Temperature [°R]
$p =$ Pressure [psia]

Since p_{sc} and T_{sc} are known, Equation 3.24 can be written as:

$$B_g = 0.02827 \frac{ZT}{p} \tag{3.25}$$

There are many ways to calculate the Z-factor, a very common way to do so is to use the Standing et al. (1942) Z-factor chart. In this thesis an other common correlation is used, where Z is a function of pseudo reduced pressure and temperature (Whitson and Brulé, 2000).

$$Z = 1 - \frac{3.53 p_{pr}}{10^{0.9813 T_{pr}}} + \frac{0.274 p_{pr}^2}{10^{0.8157 T_{pr}}} \tag{3.26}$$

The pseudo reduced pressure and temperature are functions of the pseudocritical properties p_{pc} and T_{pc} are given by:

$$p_{pr} = \frac{p}{p_{pc}} \tag{3.27}$$

$$T_{pr} = \frac{T}{T_{pc}} \tag{3.28}$$

To calculate the pseudocritical properties, the Standing (1981) correlations for gas specific gravity higher than or equal to 0.75 was used:

$$p_{pc} = 706 - 51.7\gamma_g - 11.1\gamma_g^2 \tag{3.29}$$

$$T_{pc} = 187 + 330\gamma_g - 71.5\gamma_g^2 \tag{3.30}$$

Where:

$p_{pc} =$ Pseudocritical pressure [psia]
$T_{pc} =$ Pseudocritical temperature [°R]
$\gamma_g =$ Gas specific gravity

3.4.2 Fracturing Pressure

It is important to determine a fracturing pressure or a maximum pore pressure for the injection well. This is especially important if water is injected after the CO_2,due to changes in compressibility and viscosity, the injection pressure will increase faster for water than CO_2. There was not conducted any leak off tests during the previous project at Svelvik, so to determine the limitations of the injection pressure a few, simple calculations was made to verify the existing limit. For a sedimentary compressed rock, like the poorly consolidated sand at Svelvik, the horizontal strain ϵ_x can be assumed equal to zero. It is also assumed that the horizontal stresses σ_x and σ_y are equal.

Hence, the average horizontal stress and the matrix stress is given by:

$$\sigma_H = \frac{\mu}{1-\mu} \cdot \sigma_z \tag{3.31}$$

$$\sigma_z = \sigma_{ob} - p_f \tag{3.32}$$

Where:

$\sigma_H =$ Average horizontal stress [Pa]
$\sigma_z =$ Matrix stress [Pa]
$\sigma_{ob} =$ Vertical overburden stress [Pa]
$p_f =$ Pore pressure [Pa]
$\mu =$ Poisson's ratio [Dimensionless]

The vertical overburden stress, σ_{ob}, is a function of grain density, fluid density, porosity and depth. Since porosity is affected by compaction, a porosity decline constant, K, is often included in the calculation. This constant is defined by Equation 3.33

$$K = \frac{ln(\frac{\phi_0}{\phi})}{D_s} \tag{3.33}$$

Where:

$\phi_0 =$ Surface porosity [%]
$\phi =$ Porosity [%]
$D_s =$ Thickness of sediments / depth [m]

At the injection site in Svelvik, the CO_2 is injected at 65m depth. This is relatively shallow, and it is fair to assume that the porosity is not affected much by the overburden at this depth. Hence, by assuming a reasonable ratio $\frac{\phi_0}{\phi}$, the overburden stress can be calculated without measurements of surface porosity. The overburden stress defined by the integral displayed in Equation 3.34, will then be derived into the soluble expression in Equation 3.35.

$$\sigma_{ob} = \int_0^{D_{Tot.}} \rho_b g dD \tag{3.34}$$

$$\rho_b = \rho_g(1-\phi) + \rho_{fl}\phi$$

$$\sigma_{ob} = g \int_0^{D_{Tot.}} [\rho_g(1-\phi) + \rho_{fl}\phi] dD$$

$$\sigma_{ob} = g \int_0^{D_{Tot.}} [\rho_g - (\rho_g - \rho_{fl})\phi_0 e^{-KD}] dD$$

$$\sigma_{ob} = \rho_g g D_s - \frac{(\rho_g - \rho_{fl})g\phi_0}{K}(1 - e^{-KD_s}) \tag{3.35}$$

Where:

$\rho_b =$ Bulk density [kg/m^3]
$\rho_g =$ Grain density [kg/m^3]
$\rho_{fl} =$ Fluid density [kg/m^3]
$D =$ Depth [m]
$D_{Tot.} =$ Total depth [m]
$K =$ Porosity decline constant [m^{-1}]

With σ_{ob} and the p_f obtained by assuming hydrostatic pressure, the matrix stress can be determined and hence the average horizontal stress. Finally when the limiting injection pressure is to be found, one can look at two different fracturing pressures. Hubert & Willis introduced many fundamental thoughts and principles on this limits. Among them is that the minimum wellbore pressure required to extend an existing fracture is given as the pressure to overcome the minimum principal stress:

$$p_{ff} = \sigma_{min} + p_f = \sigma_H + p_f \tag{3.36}$$

Where:

$p_{ff} =$ Fracturing pressure [Pa]
$\sigma_{min} =$ Minimum stress [kg/m^3]

As shown in Equation 3.36, the minimum stress σ_{min} is equal to the total average horizontal stress σ_H. If there are pre-existing fractures or joints in the formation, the fracture extension pressure shown in Equation 3.36 can be used as a limit for the wellbore pressure during an injection. The other and more applicable option for the Svelik ridge, when deciding an injection pressure limit, is to look at the pressure required to create a new fracture shown in Equation 3.37. Given that the minimum principal stress occurs in the horizontal plane, and that σ_x and σ_y are equal, the local stress concentration at borehole wall, σ_{Hw} is equal to the product of the two horizontal stresses (Bourgoyne Jr. et al., 1986).

This fracturing pressure is defined as:

$$p_{ff} = \sigma_{Hw} + p_f = 2\sigma_H + p_f \tag{3.37}$$

Where:

σ_{Hw} = Local stress concentration at borehole wall [Pa]

3.4.3 Production of the Injected CO_2nd the Risk of Sand Production

Pressure loss in a well can be calculated by using the Darcy-Weisbach Equation (Kudela, 2001). This equation is considered among the best empirical relations for pipe-flow resistance. In terms of pressure drop, the equation can be written as:

$$\Delta p = (z_1 - z_2)\rho g + f \cdot \frac{L}{D} \cdot \frac{\rho v^2}{2} \tag{3.38}$$

Where:

Δp = Pressure drop from well bottom hole to well head [Pa]
z_i = Height of well, starting at zero at the bottom of the well [m]
ρ = Density of produced fluid [kg/m^3]
g = Gravitational constant [m/s^2]
L = Depth of well [m]
D = Inner diameter of well [m]
v = Average flow velocity [m/s]
f = Complex function of the Reynolds Number and relative roughness

There are several ways to estimate the f (Brown, 2000). In this thesis, it is assumed that pipe roughness is not a factor for laminar flow. Laminar flow is defined as a flow with a Reynolds number lower than 2000, and the Reynolds number is calculated by:

$$Re = \frac{\rho v D}{\mu} \tag{3.39}$$

Where:

ρ = Density of produced fluid [kg/m^3]
D = Inner diameter of well [m]
v = Average flow velocity [m/s]
μ = Viscosity of fluid

For laminar flow, the function f in equation 3.38 can be given by:

$$f = \frac{64}{Re} \tag{3.40}$$

If the Reynolds number exceed 4000, the flow is defined as a turbulent flow. For turbulent flow, the function f in equation 3.38 can be given by:

$$f = \frac{0.3164}{Re^{0.25}} \tag{3.41}$$

The calculation of the pressure loss in the well was used to determine a minimum bottom hole pressure for the simulations. An other factor that is important to consider is the risk of sand production. Sand production can be defined as the migration of formation sand caused by the flow of reservoir fluids. The production of sand is generally undesirable since it can restrict productivity, erode completion components, impede wellbore access, interfere with the operation of downhole equipment, and present significant disposal difficulties. Morita et al. (1994) defines the following factors that can affect the sand production rate:

- Reduction of well pressure. If the well pressure falls below the critical sand production pressure, the chance of sand production increase.
- Fluid flow rate and viscosity. Higher rate and viscosity increase the possibility of sand production.
- Cementation. With increasing cementation of the rock, the chance of sand production will decrease.

By investigating the possible risk of sand production, one might also gain knowledge about migration of sand particles away from the well during injection of gas and/or water.

Chapter 4

Implementation

4.1 PVT-data

In this thesis CO_2 injection was simulated instead of an air injection as in the CO_2 Field Lab simulations. The gas volume factor, B_g, was calculated for various pressures by using Equation 3.24. B_g was then, together with other CO_2 PVT-data like gas specific gravity, viscosity and density, used as input data in Eclipse using the keywords DENSITY and PVDG. Table 4.1 shows the formation volume factors for CO_2, air and water for different pressures. Notice that the difference in B_g between CO_2 and air is very small.

Table 4.1: Formation volume factors for CO_2, air and water for different pressures.

Pressure [bara]	B_g, CO_2	B_g, Air	B_w
1.01325	1.000000	1.000000	1.000000
1.994283	0.506814	0.507424	0.999981
3.956401	0.251095	0.256021	0.999948
5.937769	0.164398	0.17086	0.995000
6.928962	0.139643	0.146562	0.990000
7.920156	0.121092	0.128347	0.989800
8.911349	0.106672	0.114186	0.989600

The input PVT-data can be found in the Eclipse data file included in the appendix under the ”Props”-section.

4.2 Corey and Brooks Relative Permeability Curves

Eclipse allows for subdivision of the reservoir into smaller parts or regions. These parts serve to be described by different characterizations of various kinds. This is favorable when different relative permeability curves are to be assigned to different layers, dominated by a grain size distribution, of the reservoir. To decide the regions of validity for relative permeability curves, the keyword SATNUM is used.

When SATNUM is included in the input text file, every grid cell is assigned one SATNUM number between 1 and N_{SATNUM}, where N_{SATNUM} is the total number of regions. This SATNUM number assigns the grid cell to a certain set of relative permeability tables. If the grid cell belongs to SATNUM number M, relative permeability data will be obtained from table number M. This means that N_{SATNUM} sets of relative permeability curves must be defined.

The relative permeability curves were calculated by using the Corey and Brooks equations as stated in Chapter 3.5. The number of sets of relative permeability curves were decided by the the number of different facies in the reservoir with a corresponding grain size distribution index, λ. In Figure 4.1 the different layers with a corresponding set of relative permeability curves can be seen.

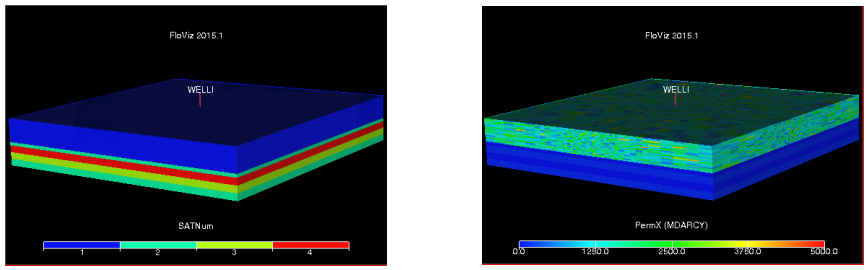

(a) **(b)**

Figure 4.1: (a) The different SATNUM regions with corresponding sets of relative permeability curves. 1 (Dark Blue):Unconsolidated sand, 2 (Green): Silt, 3 (Yellow):Sandy Clay, 4: Consolidated sand. (b) Permeability of the different regions.

The different relative permeability curves can be implemented into the Eclipse simulation model by using a variety of keywords. In this case, there are only two phases, water and gas. In the previous simulation models, ”oil” has been given the properties of water in the model. Hence, the model believes that there are two phases, oil and gas, where the oil will act exactly like water. This has not been changed, and therefore when the relative permeability curves are assigned, keywords where oil is the wetting phase and gas is the non-wetting phase are being used. The keywords used are SOF2 for the wetting phase

relative permeability, and SGFN for the non-wetting phase relative permeability. This is a common trick for simulations of water-gas systems, since ordinary black-oil formulations can be used to model the solubility of CO_2 in water.

These two keywords take in N_{SATNUM} relative permeability tables, calculated in excel using the Corey and Brooks equations, i.e. a list of saturations from zero to one, with corresponding relative permeability values. The number of tables that are entered must be specified under NTSFUN and TABDIMS in the RUNSPEC section. SGFN is dependant on a capillary pressure value corresponding to the saturation, in addition to the relative permeability value. One capillary pressure curve was included in the previous simulation model, however the source of this is unknown. Since this was not investigated in this thesis, this capillary pressure curve is only used in conjunction with the the corresponding relative permeability curve. For all the other relative permeability curves, the capillary pressure input was defaulted, as can be seen in the Eclipse data file included in the appendix. When the tables are read in, defaults are replaced by values computed by linear interpolation.

The size of each layer was decided by copying the structure of the model shown in Figure 4.1 (b). By using the lithology description in Figure 4.2, it was verified that a fitting grain size index was chosen to each layer.

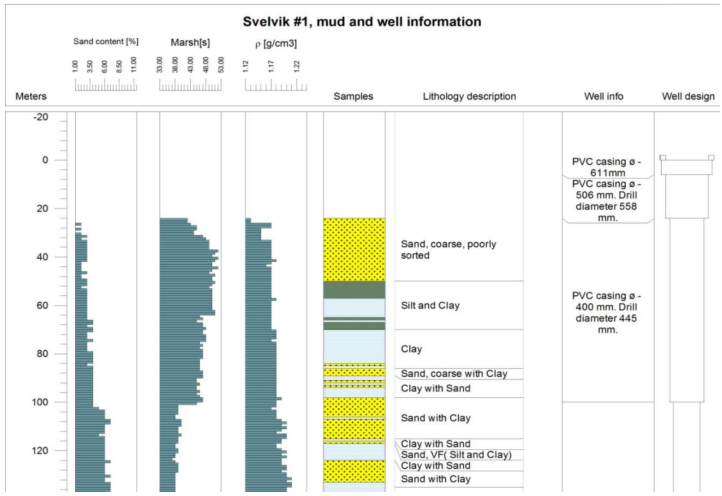

Figure 4.2: Excerpt from the Svelvik #1 mud and well information (Ruden, 2010).

The SATNUM-curves are primary drainage curves and will not be able to describe the plume evolution alone, as discussed in Chapter 3.3. therefore hysteresis and imbibition curves was introduced by including the IMBNUM keyword.

4.3 Relative Permeability Hysteresis

If the hysteresis option are being used in Eclipse both drainage curves and imbibition curves have to be entered. Similar to the SATNUM-keyword, the region keyword IMBNUM is used to assign imbibition table numbers to every cell in the model. The syntax of these two keywords are identical. In our model, IMBNUM distributes the imbibition curves to the corresponding layer, so that the distribution of imbibition curves match the the distribution of drainage curves assigned by the SATNUM keyword, like shown in Figure 4.3. The CO_2 is injected into the silty layer marked in green at the bottom of the two figures. The overlying clay is the confining layer.

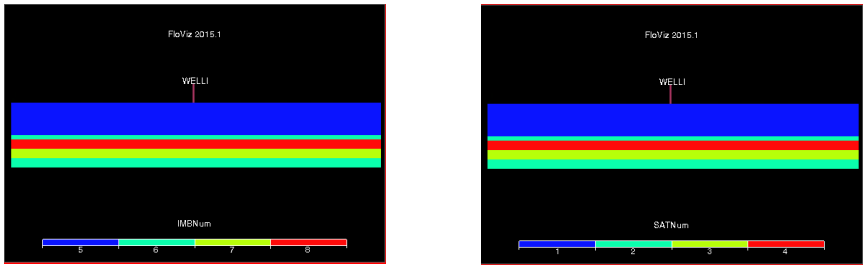

(a) **(b)**

Figure 4.3: The IMBNUM layering (a), is identical to the SATNUM layering (b)

The imbibition curves were calculated in excel by using the Carlson model. The main idea behind this model is Equation 3.3, which states that the imbibition curve, at the non wetting saturation, is equal to the drainage curve at the free non-wetting saturation. The free non-wetting saturation is calculated by Equation 3.6, but before this can be calculated, the constant *C* has to be estimated. Since there are no experimental imbibition data points availiable, the constant was estimated by Jerauld's assumption (Jerauld et al., 1997):

At $S_{nwi} = 1$,

$$S_{nwr} = \frac{1}{C+1}$$

This assumption is an error source, that may effect the results. This is further discussed under "Further Work". The resulting imbibition curves are shown in Figure 4.4.

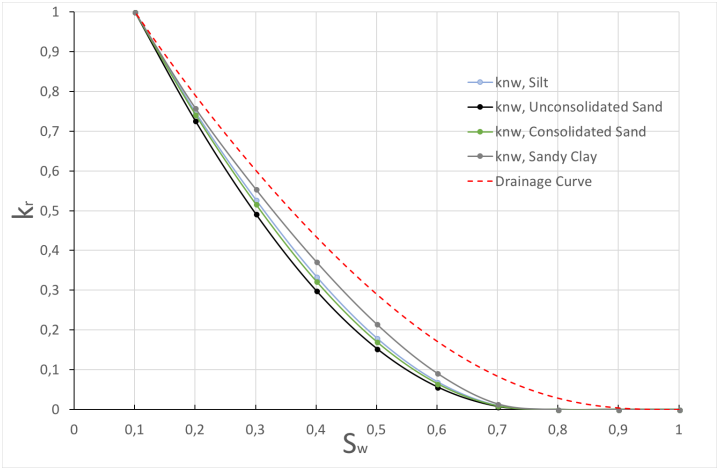

Figure 4.4: The imbibition curves, calculated by using Carlsons model for the non-wetting phase. The drainage curve in red is shown as reference

The Carlson model assumes that the relative permeability of the wetting phase shows no hysteric behaviour. Hence, the relative permeability imbibition curve was only calculated for the non-wetting phase. Based on this assumption, the imbibition relative permeability curve for the wetting phase was set to be equal to the drainage curve in Eclipse. Imbibition curves for the wetting phase could be calculated by many models eg. Land or Killough, but this was not done in this thesis. It is possible to include Killough's model for wetting phase hysteresis in Eclipse.

4.4 Geology and Anisotropy

In the previous simulation model, the permeability was isotropic for all layers. To simulate the effect of anisotropy, the directional permeability was changed in the simulation model in this thesis. Eclipse allows for alternation of the permeability described in the input geology model. This is done in the "Grid"-section of the text script. Firstly, the region where the permeability is to be changed needs to be defined. This is done by using the keyword BOX. The BOX is an index cube that is bounded by constant indices in all directions.

When the region where the permeability will be changed is defined, the direction of the permeability and the new value are decided by the keywords PERMX, PERMY and PERMZ. The last letter of the keyword decides the direction of the permeability. The keyword is then followed by the new permeability value in millidarcy. In this thesis anisotropy in the different directions was simulated by using these keywords.

For the reduced permeability in the east-west and north-south directions, the box included the whole model except the boundaries like seen in Figure 4.5 (a).

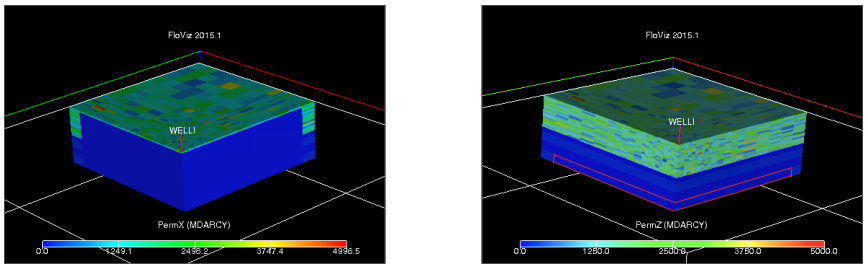

(a) **(b)**

Figure 4.5: (a) Permeability in x- and y-direction, (b) Permeability in z-direction, the region with reduced permeability is enclosed with red lines

To keep a realistic permeability of the confining layer, the permeability in the z-direction was only reduced inside the region where the CO_2 was injected, below the sealing layer. This means that the permeability in the confining layer is so low that it was kept isotropic for simplicity. The region where CO_2 was injected is enclosed with red lines in Figure 4.5 (b).

There were conducted separate simulations where the different directional permeabilities were reduced in separate runs. One with no anisotropy, one with reduced permeability in the north-south(x) direction, one with reduced permeability in the east-west (y) direction, one with reduced permeability in the vertical(z) direction and lastly one with reduced permeability in both north-south (x) and vertical (z) directions. These various simulations were conducted to see a possible effect of the anisotropy that is belived to be present as discussed in Chapter 3.1. The last simulation with reduced permeability in north-south and vertical (x and z) direction is the most relevant.

Permeability of the confining layers

To investigate the possibility of vertical migration through the confining layers, different scenarios where modelled. In these simulations the vertical permeability in the two layers were set to be equal. The migration was simulated for permeabilities of 0.5, 1, 2, 5, 8 and 10 mD in the two confining layers at 50-60m depth and 30-37m depth. The CO_2 migration was simulated for one year after cessation of CO_2 injection.

4.5 Scenario Modelling

An ideal scenario for the Field Lab would be to be able ”reset” the conditions of the reservoir. I.e. regain initial pressure and saturation conditions. According to the simulations, the pressure is reset quite fast, however, the time before the CO_2 plume is entirely out of the system is much longer. The reduction of the CO_2 saturation in the reservoir is dependant on among other factors, the transport of brine through the sediments. Therefore, in thesis it will be discussed whether it would be possible and/or practical to accelerate this process, e.g. by injecting brine for a prolonged period after the end of the gas injection test or producing from the reservoir.

To investigate the effect of these two options, it was desirable to monitor the simulated gas in place in the injection zone around the well. To do this, the reservoir was subdevided into regions by the keyword FIPNUM. Eclipse can then request separate reports for each region, eg. gas in place or formation pressure. These regions was set to have the confining layer as an upper limit, and three separate regions was created as shown on figure 4.6. One is a 100m x 100m square with the well in center, one is 50m x 50m and the last one is 30m x 30m. The confining layer is close to impermeable, so an injection of water was expected to result in a lateral displacement of the gas.

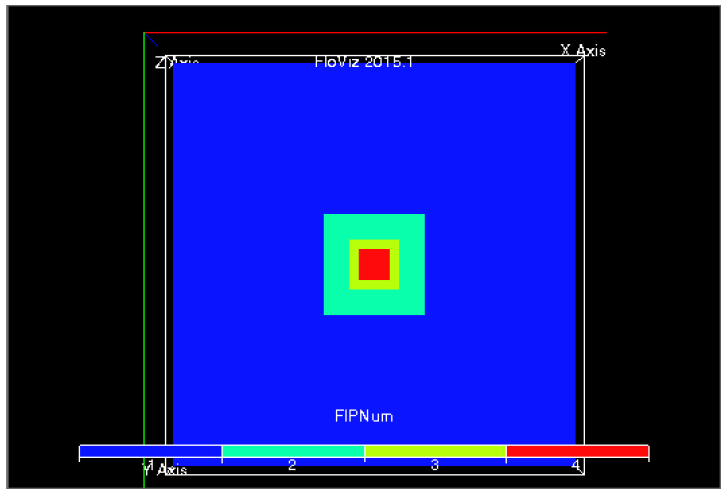

Figure 4.6: Different FIPNUM-regions, where 1: The whole model, 2: A 100m x 100m square with the well in center, 3: A 50m x 50m square with the well in center and 4: A 30m x 30m square with the well in center

These regions are created to monitor the formation pressure and the gas in place. When the whole model is considered, the gas in place is constant for the water injection simulations, and the effect of lateral migration and the effect of lateral displacement by water is non existing. If the 100m x 100m square is defined as the area of interest, the migration effect, and the effect of water injection becomes visible. The effect of production is visible either way, but it will be easier to compare the two options if these regions are used for both cases.

The FIPNUM keyword syntax is very similar to the other REGION keywords. Number of blocks in the region is multiplied with the value of the region. This makes it complicated when the regions needs to be defined as squares with the well in the center as shown in Figure 4.6. To make it easier to define these regions, the keyword EQUALS are used. EQUALS allows you to define the region as a BOX with ix_1-ix_2, jy_1-jy_2 and kz_1-kz_2 as boundary coordinates.

After defining these, the effect of migration on the gas in place was tested for the different models. These simulation results will work as a base case when the effect of water injection and production is tested.

To test the effect of water injection, different simulations of water injection after the CO_2 injection were conducted. Using the keyword WCONINJE, the injection rate and maximum bottom hole pressure was determined. To decide the duration of the injection, the keyword TSTEP was used. For the first water injection simulation, the injection was set to be limited by a bottom hole pressure of 10 Bara. This limit was used for the CO_2 injection in the earlier CO_2 Field Lab simulations, and was verified by the calculations of the fracturing pressure using Equation 3.31-3.37. The calculated fracturing pressure is plotted against depth in Figure 4.7.

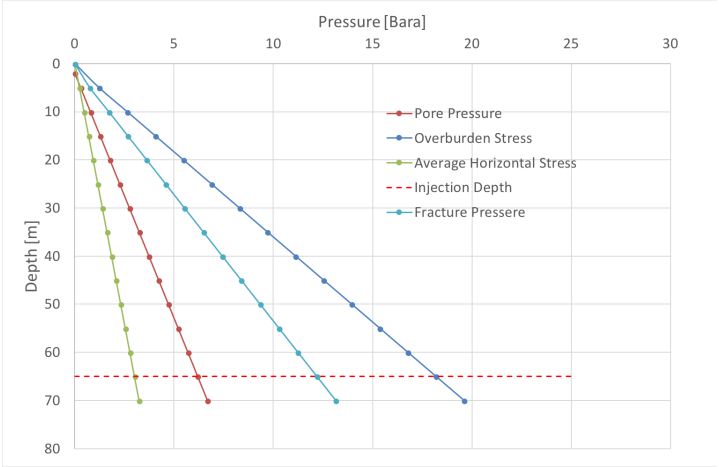

Figure 4.7: Fracture pressure, Pore pressure, Average Horizontal Stress and Overburden Stress versus depth

The Figure shows a fracture pressure slightly higher than 10 bara in the injection zone. This fracture pressure was calculated based on simplifications and without a safety factor. It was therefore concluded that 10 bara could be a realistic limit. This low pressure results in a very low injection rate, as this fracturing pressure is quite low, mainly caused by the shallow injection depth. To see any effect, simulations with no limiting bottom hole pressure and a higher injection rate was conducted.

The other option to approach pre-test saturation and pressure conditions was to produce. Production from the reservoir in an attempt to produce out the injected CO_2, was simulated. To define the bottom hole pressure limit, pressure loss calculations were conducted. The pressure drop throughout the well was calculated with Equation 3.38 for different rates. The pressure drop was relatively low, and it did not vary much with the rate. The different rates and the corresponding pressure drop are displayed in Table 4.2.

Table 4.2: Pressure loss from bottom hole to well head for five different rates.

Rate	Δp
1 Sm^3	0,13990053 Bar
5 Sm^3	0,13990102 Bar
10 Sm^3	0,13990164 Bar
25 Sm^3	0,13990348 Bar
50 Sm^3	0,139906546 Bar

The default bottom hole pressure limit in eclipse was 1 bar. Since the pressure drop for all rates was less than 1 bar, it could be assumed that the well was capable of producing at a well bottom hole pressure of 1 bar. For the simulations in this thesis, the bottom hole pressure limit was kept at 1 bar. The pressure drop in Table 4.2 was calculated with a water cut of 2%. The water cut where the pressure drop inside the well became larger than 1 bar, (where the well no longer could produce), was found by using the "Solver"-function in excel. In Figure 4.8 the water cut is plotted versus time, together with the production rates and the limiting water cut for the simulation case where a gas production rate of 50 sm^3/day was chosen.

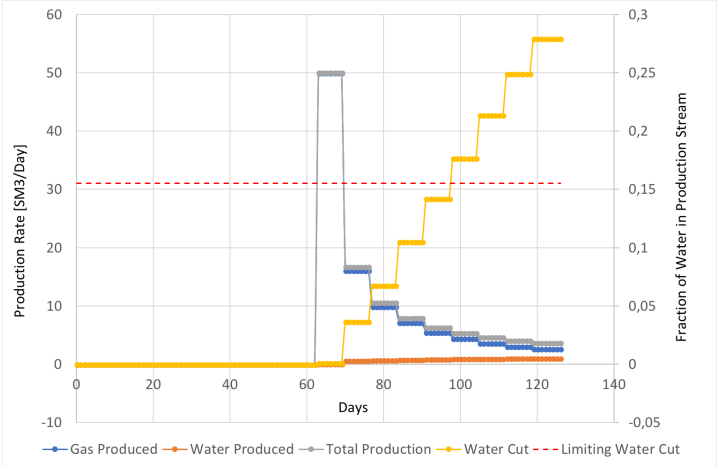

Figure 4.8: Determination of production stop caused by bottom hole pressure limit and water cut.

The effect of different production rates, production build up and well placement was tested. Production was simulated in both the original and the updated model, the results were compared and analyzed.

The well placement test was conducted to see if the cumulative CO_2 production would increase if the well was perforated directly under the confining layer. To simulate this, a new well was defined in WELLSPECS and COMPDAT. The new well, named 'WELLP', was located in the exact same blocks as the injection well. The only difference was that the new well was shorter in the vertical direction and stopped in the grid block right below the confining layer.

Chapter 5

Simulation Results

5.1 Updates of the Simulation Model

In this section, the results of the different model updates simulated in the reservoir simulator Eclipse are compared to the air injection simulation results from the CO_2 Field Lab project. Mainly, the simulation output that will be compared and discussed in this section, is the saturation profile around the injection well, 126 days after injection start. Jordan et al. (2015) stated that an injection rate of 200 m^3/day would lead to a bottom hole pressure higher than the calculated limit of 10 bar. This was not considered safe, and the injection rate was set to 50 m^3/day for all succeeding simulations. CO_2 is therefore injected with a rate of 50 SM3/day in this thesis. The injection lasts for 63 days, then the injection is stopped for 63 more days. The injection rate and the increasing gas in place can be seen in Figure 5.1 (a) and (b).

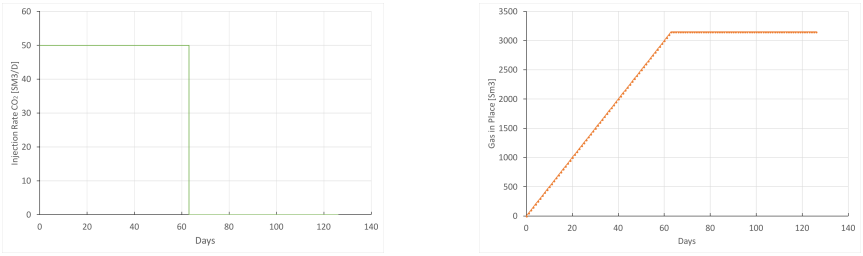

(a) **(b)**

Figure 5.1: (a) CO_2 injection rate plotted against time for all simulation models. (b) Gas in place as a function of time, for all simulation models.

The first addition to the model was to change relative permeability drainage curves. Each layer in the layercake model was assigned a set of relative permeability curves corresponding to the grain size of the layer. Hence, the relative permeability became a function of the grain size distribution of the reservoir. In Figure 5.2 the saturation profile around the injection well 63 days after injection cessation is shown. Model with different relative permeability curves as a function of different grain size distributions at the bottom. Original model at the top, with visible hysteresis and an endpoint gas saturation of 0.25.

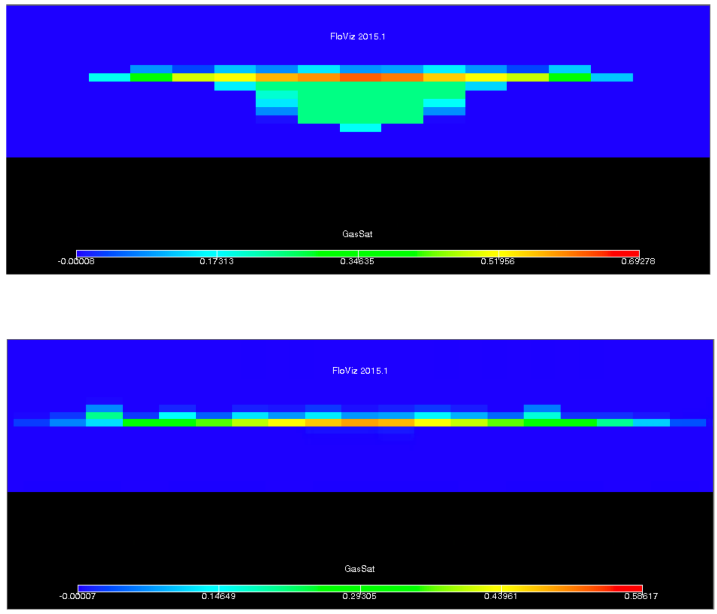

Figure 5.2: The saturation profile around the injection well 63 days after injection cessation. Model with different relative permeability curves as a function of different grain size distributions at the bottom. Original model at the top.

In Figure 5.2, the saturation profile of the model with different relative permeability curves assigned to different grain size distributions is narrower and wider. The main grain size in the layer where the CO_2 is being injected is Silt. The grain size distribution index of Silt is very close to the index chosen to be applicable for the whole reservoir in the original model, however there are huge differences in these two profiles. The main thing that stands out is that there is no residual trapping in the model where hysteresis is not yet included. All the injected CO_2 will migrate and be trapped by the confining layer. The

main reason for this can be seen on the relative permeability curves in Figure 3.14 under Chapter 3.5. The relative permeability curves for the non-wetting phase increase at a much lower non-wetting saturation. This will result in a more mobile CO_2 plume causing more CO_2 to migrate and be trapped under the confining layer.

In Figure 5.3, the model with different relative permeability curves assigned to different grain size distributions (top) is compared to the model with relative permeability hysteresis for the non-wetting phase included (bottom). By including hysteresis, one can see that there will be more residually trapped gas.

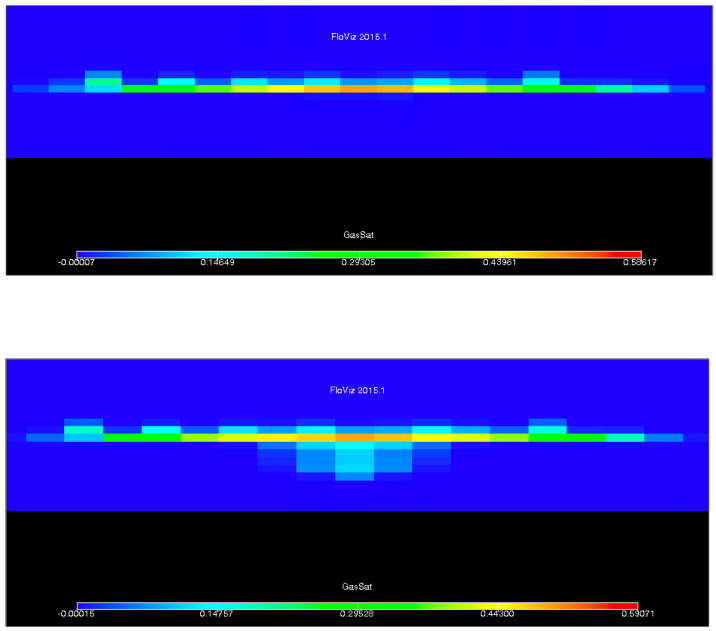

Figure 5.3: The saturation profile around the injection well 63 days after injection cessation. Model with relative permeability as a function of grain size distributions at the top. Same model with relative permeability hysteresis for the non-wetting phase included at the bottom.

In Figure 5.4 the CO_2-saturation is plotted against distance from the well. This figure shows that the CO_2 moves more freely and migrates further in a lateral direction, when hysteresis and residual trapping is not included.

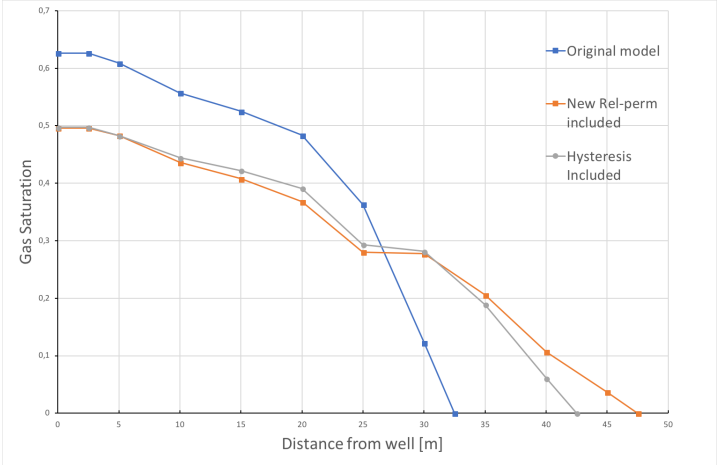

Figure 5.4: CO_2-saturation versus distance from well, right below the confining layer, for the three different models.

The original model has a higher gas saturation closest to the well than the two other models, but as you move further away from the well the two other models has a higher gas saturation. This difference is not caused by the grain size distribution index, but by the simplification in the relative permeability model used in the CO_2 Field Lab simulations.

5.2 The Effect of Anisotropy

Anisotropy was simulated by reducing the directional permeability separately, respectively for x-, y- and z-direction. Here, the x-direction represents north-south, the y-direction represent east-west, and the z-direction represent depth into the reservoir. As a simplification, when simulating the lateral anisotropy, the permeability of the whole interior of the model was reduced in the x- and y-directions. As suspected, a change in the directional evolution of the plume was the main difference from the isotropic model. In Figure 5.5, the CO_2 plume is seen from above, 63 days after cessation of injection.

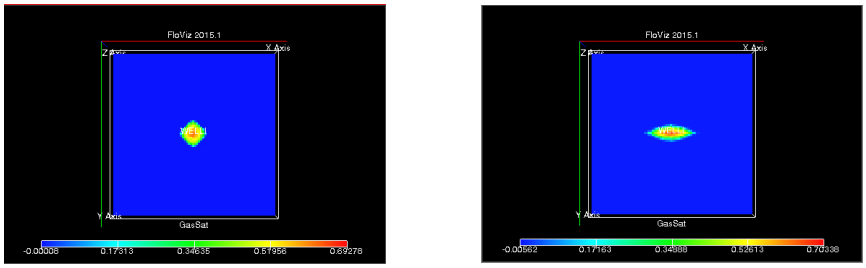

(a) **(b)**

Figure 5.5: (a) The CO_2 plume is seen from above, 63 days after cessation of injection, for the original, isotropic simulation model, (b) The CO_2 plume is seen from above, 63 days after cessation of injection, for the simulation with reduced permeability in north-south direction (y-direction).

The vertical profile of the CO_2 plume is similar to the isotropic model created in this thesis, shown in figure 5.3. Anisotropy in the vertical direction was simulated by reducing the reservoir permeability in the z-direciton, however, the permeability is only changed in the facies where the CO_2 is being injected as shown in Figure 4.5 (b). The CO_2 plume, seen from the side, 63 days after cessation of injection, for the simulation with reduced permeability in vertical and north-south direction is show in Figure 5.6.

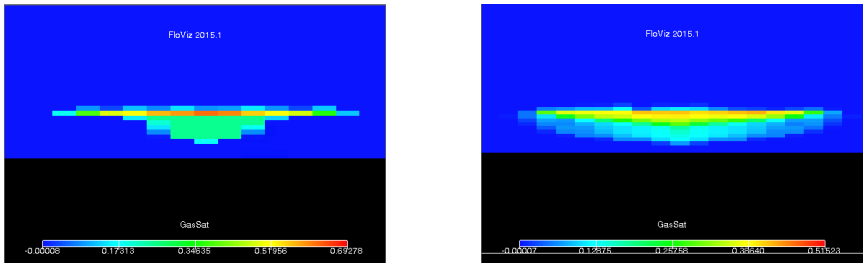

(a) **(b)**

Figure 5.6: (a) The saturation profile around the injection well 63 days after injection cessation. Original, isotropic simulation model , (b) The saturation profile around the injection well 63 days after injection cessation. Anisotropy in north-south and vertical direction simulated by reducing the permeability in the respective directions.

In the simulations in this thesis, the vertical and north-south directed permeability was reduced to 10 millidarcy, which is less than $\frac{1}{10}$ of the permeability in the isotropic model. This reduced permeability will result in a slower migration of the CO_2, and more CO_2 will be residually trapped during the imbibition process as shown in Figure 5.6 (b). 63 days after injection stop, the main features of the anisotropic model shown in Figure 5.6 (b) is that the saturation profile is more evenly distributed. The lateral extension in the middle

of the plume is much wider than the models where vertical anisotropy is not included.

5.3 Scenario Modelling Results

5.3.1 Permeability of the Confining Layers

To evaluate the possibility of vertical migration of CO_2 throughout the formation, various permeabilities were allocated to the two confining layers in the model. The saturation profiles around the injection well for the different permeabilities are displayed in Figure 5.8.

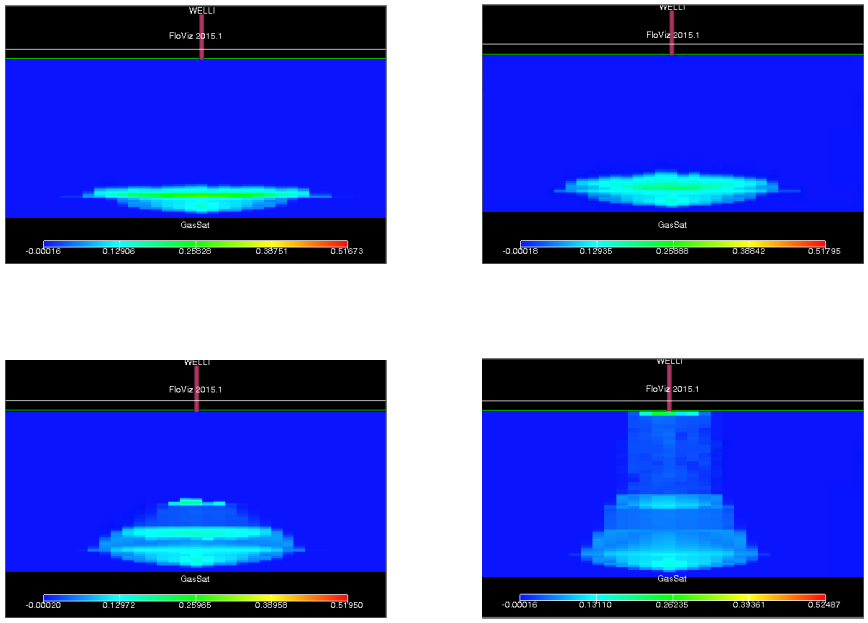

Figure 5.8: CO_2 migration pattern for different permeabilities of the confining layers. Top left: confining layer permeabilty of 0.5 mD, Top right: confining layer permeabilty of 1 mD, bottom left: confining layer permeabilty of 2 mD and bottom right: confining layer permeabilty of 5 mD.

The CO_2 will migrate into the confining layer, but not through, when the confining layer permeability is 0.5 mD. At a confining layer permeability of 1 mD, the CO_2 will migrate further in to the confining layer, but not completely through after one year. When the permeability of the confining layer is 2 mD, the CO_2 is able to migrate through the first confining layer and into the second at 37m depth. And as shown at the last saturation profile in Figure 5.8 where the confining layer permeability is 5 mD, the CO_2 is able to migrate through both confining layers and out of the formation after one year.

5.3.2 Water Injection Post Cessation of CO_2njection.

To investigate the effect of water injection and production of the gas in place, three monitoring regions was created. A 100m x 100m square, a 50m x 50m and a 30m x 30m as shown in Figure 4.6. All with the well in the center. To be able to see the effect caused by either options, the effect of the migration alone had to be determined. In Figure 5.9 the gas in place is plotted for the different regions against time.

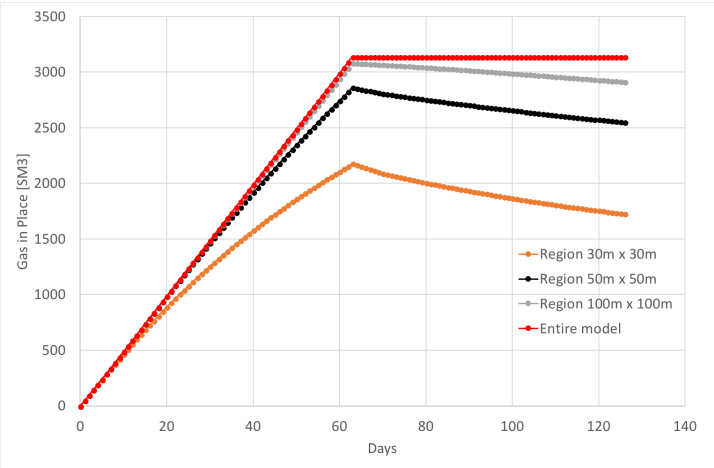

Figure 5.9: Gas in place for the three different regions in addition to the gas in place for the whole model.

Notice that the gas in place for the entire model is constant. This means that there are no vertical migration of CO_2 out of the model. This is mainly because the permeability of the confining layer is set to be close to zero. The effect of the lateral migration can be seen as the CO_2 saturation decrease faster with time, closer to the well.

With this background data, water injection and production was tested and evaluated. For the water injection case, three simulations sets were conducted. One with a bottom hole pressure limit of 10 bar, similar to the CO_2 injection limit. One simulation set where the effect of the water injection rate were tested. During this set, there was no bottom hole pressure limit and three different rates were tested. The last simulation set tested the effect of anisotropy.

With the calculated fracture pressure shown in Figure 4.7, the limit bottom hole pressure was set to be 10 bar as in previous simulation models. This limit results in a low injection rate. From Figure 5.10 it is clear that the effect of water injection at this rate is limited. The figure shows gas in place for the three different regions, affected by injection of water and migration separately.

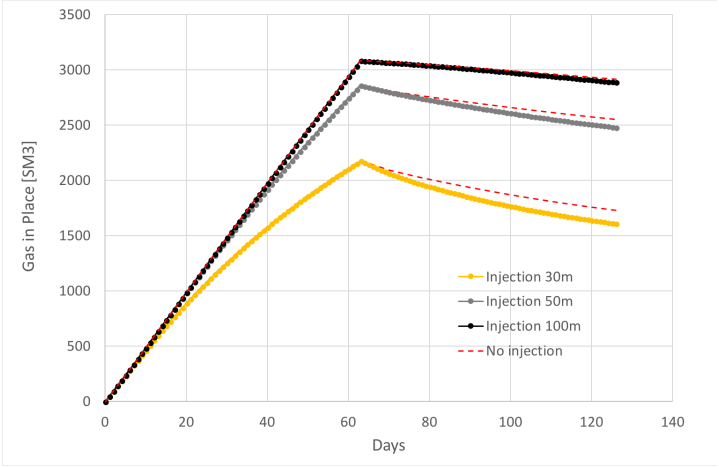

Figure 5.10: Gas in place for the three different regions with water injection.

To further investigate the effect of the water injection, the region defined as a 50m x 50m square with the well in the center was set as a standard for the following graphs and figures. In Figure 5.11, the gas in place for the mentioned region (50m x 50m) is plotted against time for four different water injection rates. It is important to notice that all these rates exceeds the fracture pressure limit of 10 bar as shown in Figure 5.12. The gas in place in Figure 5.11 start from the first day of water injection (day 64), as all curves are equal in the CO_2 injection phase. The y-axis starts at 1500 Sm^3, so that the differences can be seen. The total reduction of the gas in place is relatively small.

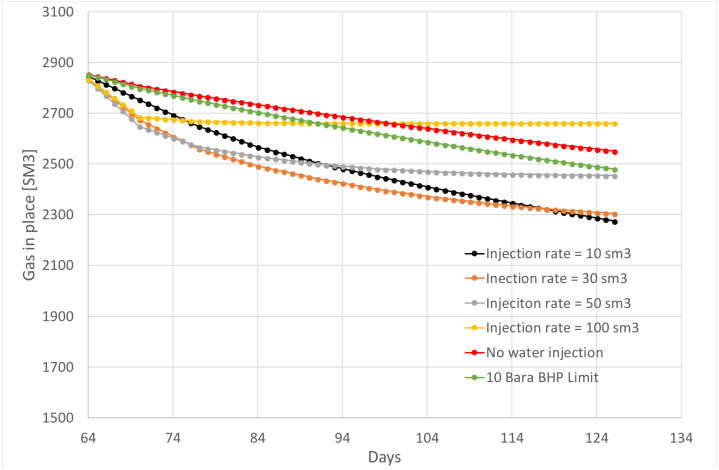

Figure 5.11: Gas in place for a 50m x 50m square with the well in the center is plotted against time, from end of CO_2 injection to end of water injection, for four different water injection rates.

In Figure 5.12 the corresponding well bottom hole pressure to the injection rates in Figure 5.11 is plotted. In addition, the injection limited by a 10 bar well bottom hole pressure and the fracture pressure is included.

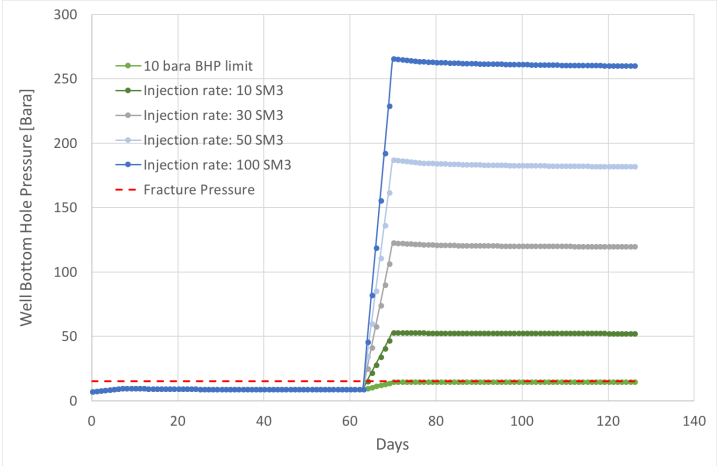

Figure 5.12: Well bottom hole pressure for the different water injection rates.

It is assumed that anisotropy is present at 65 m depth. It is therefore interesting to look at the effect of anisotropy on the migration of the CO_2. In Figure 5.13, the gas in place is plotted for four different anisotropy scenarios: Anisotropy in vertical direction, in lateral direction (North-South), both vertical and lateral and no anisotrpy.

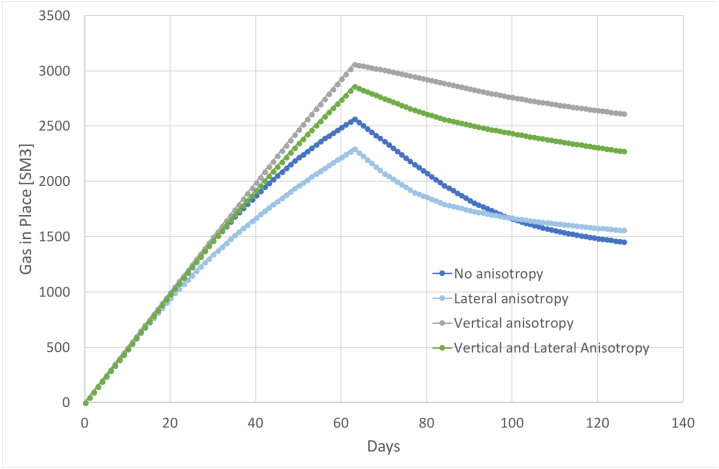

Figure 5.13: Gas in place for a 50m x 50m square with the well in the center is plotted against time for different anisotropies.

In Figure 5.14, the gas in place and bottom hole pressure for a 10 SM3/days water injection in the original and updated model is plotted. Here, the updated model include hysteresis and permeability anisotropy in the north-south and vertical direction.

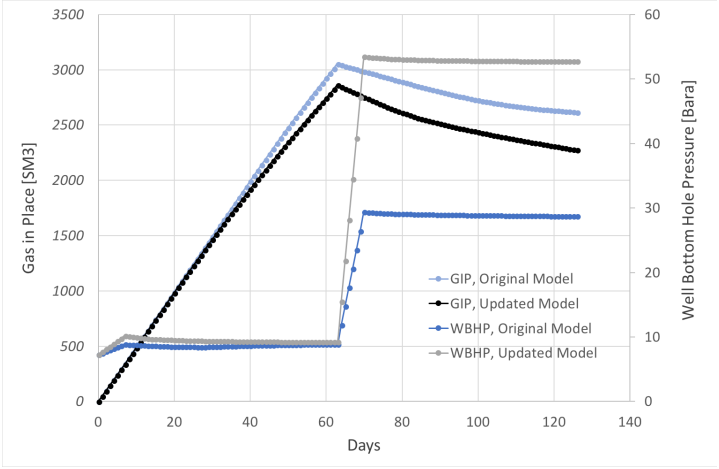

Figure 5.14: Comparison of the gas in place and well bottom hole pressure for a 50m x 50m square with the well in the center is plotted for the original and updated models.

Even though the saturation profile around the well of the original model and the updated model in Figure 5.2 and 5.6 are quite similar, the well bottom hole pressure of the updated model is over twice as high as the one in the original model. Which is caused by the reduced permeability in the updated model.

5.3.3 Production Post Cessation of CO_2njection

The effect of production from the reservoir was investigated by simulating production with different production rates. In Figure 5.15, the gas in place for the whole field is plotted against time for five different rates. The production is stopped when the water cut becomes so large that the pressure loss in the well is greater than 1 Bar, resulting in a $\frac{\delta(GIP)}{\delta T} = 0$ in Figure 5.15.

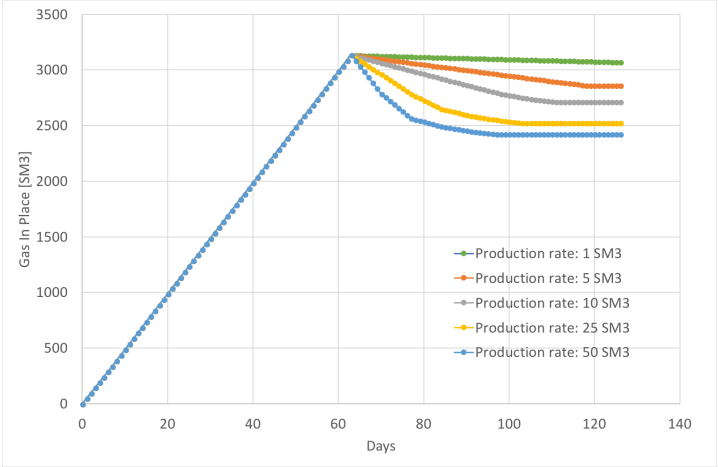

Figure 5.15: Gas in place for the formation, for different production rates.

The corresponding drawdown is plotted in Figure 5.16. The rate of 1 Sm^3 is the only case where the pressure in the well is not reduced to 1 Bar.

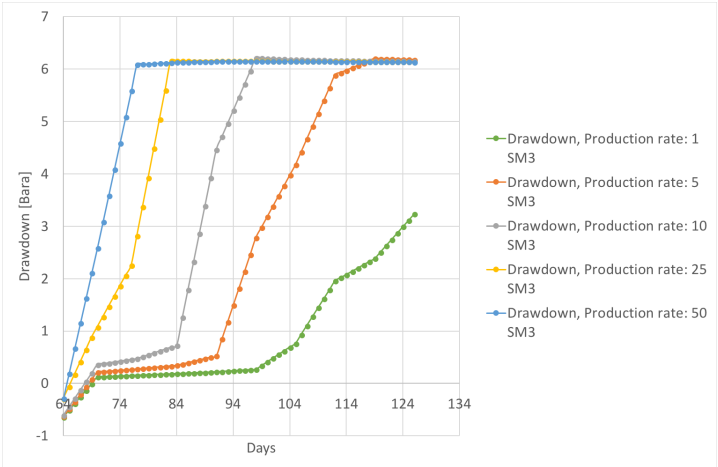

Figure 5.16: Drawdown for different production rates.

When investigating the CO_2 plume evolution, and the saturation profile around the well, it became clear that a large fraction of the injected CO_2 migrates in a vertical direction and gets stratigraphically trapped under the confining layer. It was therefore interesting to investigate the effect of the well placement and to see if the perforation depth would make a difference in the efficiency of the production. In Figure 5.17, the gas in place is plotted against time for the two well placements for the 50 sm^3/day production rate case.

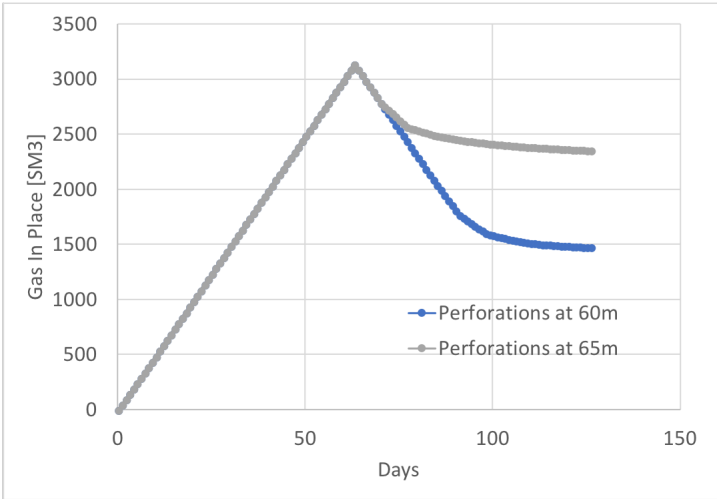

Figure 5.17: Difference in formation gas in place for perforations at 60m and at 65m for a 50 Sm^3/day gas production rate.

From this Figure it is visible that a change in the perforation depth can lead to a much higher cumulative gas production. The effect is further illustrated with the saturation profiles around the well for the two cases displayed in Figure 5.18.

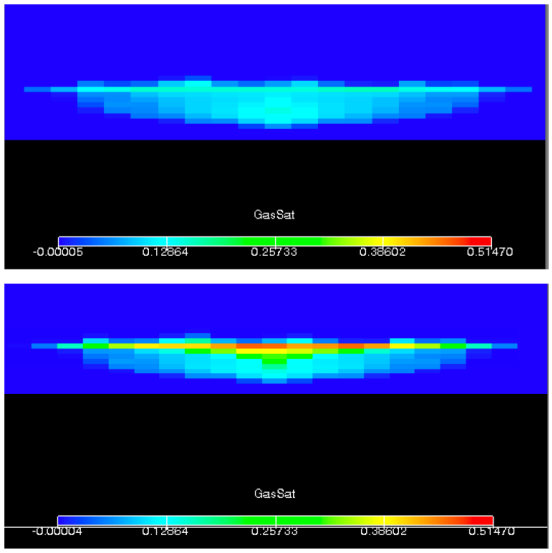

Figure 5.18: Saturation profiles after 63 days of CO_2 injection and 63 days of production for perforations at 60m (top) and at 65m (bottom).

All the production cases were simulated using both the updated model with anisotropy and hysteresis included, as all the previous figures, and the original model. In Figure 5.19, the gas in place and drawdown is plotted against time for the original and updated model.

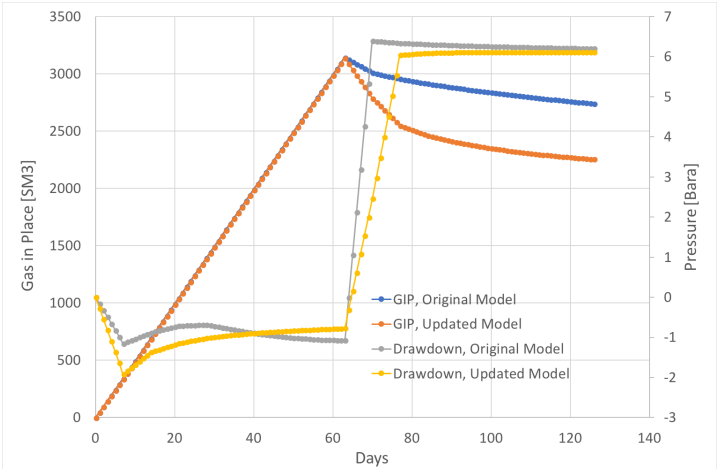

Figure 5.19: Gas in Place and drawdown for original and updated model.

To handle the possible risk of sand production, a lower production rate could be initiated right after cessation of CO_2 injection. The rate could then gradually be increased until it reached the predetermined production rate. In Figure 5.20, one can see the different build ups, and the corresponding effect on the total gas production.

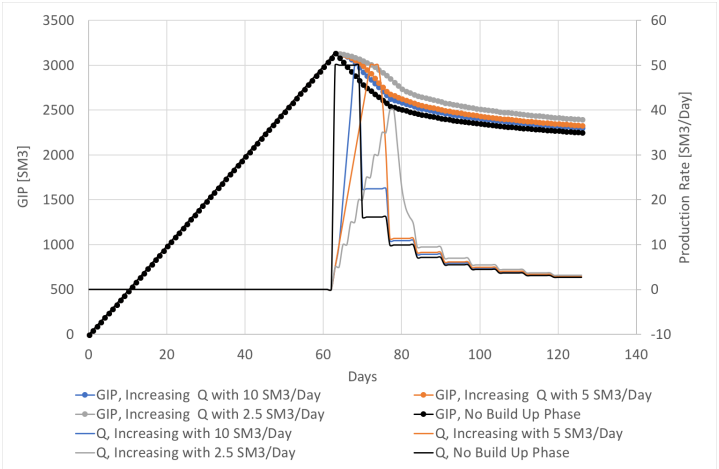

Figure 5.20: Gas in place and production rates for different production strategies.

From the figure, it can be seen that the longer time it takes before the production ”plateau” is reached, the less CO_2 is produced from the reservoir. The difference in the gas in place is not that large, so if it is necessary to include a build up phase to avoid sand production this could be a good option. However, as seen from the figure, if the build up phase is long enough, the pressure support from the formation will not be large enough to produce the desired rate.

Chapter 6

Interpretation and Discussion

6.1 Updates of the simulation- and geology model.

The three relative permeability models that are described so far in this thesis are the original model, the model where relative permeability is a function of grain size distribution, and lastly, the model where relative permeability is a function of grain size distribution and hysteresis is included. The main idea behind these changes, was to be able to describe the expected reservoir response to CO_2 injection in a more realistic way than initially (Jordan et al., 2015). The relative permeability curves was calculated by Corey and Brooks equations as functions of the grain size distribution. The grain size distribution index is essential in these calculations, and is one of the assumed parameters in this thesis. The values of the grain size distribution index was retrieved from Assouline (2005), as general values for different grain size distributions. These were assumed to be applicable for the Svelvik Ridge as a simplification. The grain size distribution index, λ, can be found with capillary pressure curves and Equatino 2.4, as explained in Chapter 2.3. In the original model, the grain size distribution index was assumed to be constant and equal to 2. Residual saturation of the wetting- and non-wetting phase and one capillary pressure curve were given in the simulation files of the original model. The endpoint saturations have been used in the updated simulation models. The capillary pressure curve has been used in the updated simulation models together with defaulted curves.

It is evident from the results, that the model where relative permeabilty is modelled without hysteresis, is not describing a realistic CO_2 plume evolution after an injection. All the CO_2 migrates up and stays stratigraphically trapped under the confining layer. No gas is trapped due to residual trapping. In Chapter 2.4, different trapping mechanisms are

discussed, and as can be seen in Figure 2.3 from Krevor et al. (2015), the three trapping mechanisms, that is effective from the start of a gas storage, are stratigraphic-, residual- and solubility-trapping.

Hence, one can assume that the drainage relative permeability curves as functions of grain size is not able to describe this system alone. This introduces a need to describe the relative permeability during the imbibition process and the transition between the drainage curve and the imbibition curve when the process is reversed like described in Chapter 3.6.

In this thesis, this was done by calculating the imbibition curve using Carlsons model for the non-wetting phase. The imbibition curves are input in the Eclipse simulation model together with the drainage curves. Eclipse will then simulate the hysteresis effect. To investigate the calculations of the drainage and imbibition curves, a sensitivity analysis was conducted.

Assumptions has been made to a various extent when implementing a new relative permeability in this thesis. In these sensitivity analysis, these assumptions will be addressed. Firstly, the computations of the drainage curves are investigated. To calculate the drainage curves the Corey and Brooks equations were used. These are functions of wetting phase saturation, wetting phase residual saturation and grain size distribution index, λ as can be seen in Equation 3.1. To test the sensitivity of the parameters that were assumed, a base case was chosen and four scenarios were evaluated. Since the CO_2 is injected into a silty layer, the base case was set to be the wetting phase drainage curve, calculated with the grain size distribution index for silt (Assouline, 2005) and a residual water saturation of 0.1. This base case is equal to the CO_2 Field Lab simulations, but in that case the grain size distribution index for silt was used. When the base case drainage curve was calculated, the residual wetting phase saturation was multiplied with 0.5 and 2. Then the grain size distribution index, λ, was multiplied with 0.5 and 2. The resulting curves can be seen on figure 6.1

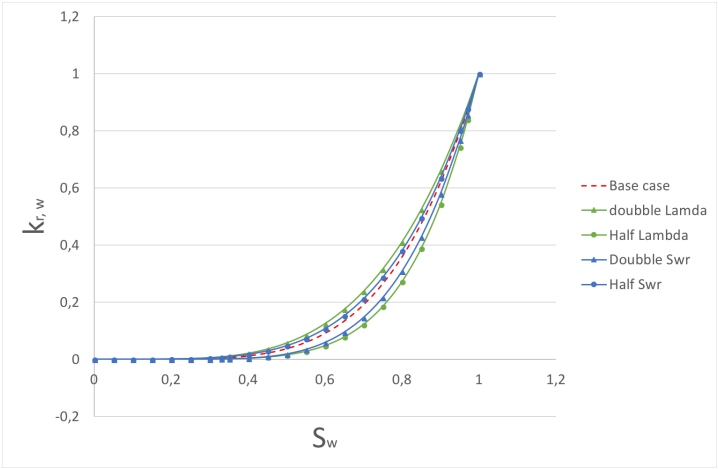

Figure 6.1: Drainage curves of the different scenarios that were tested in the sensitivity analysis of the calculation of the drainage curves.

To get numbers that are easily understood, the average deviation in relative permeability from the base case was calculated. This was then divided by the average relative permeability of the base case, to get a average deviation in $\%$ as displayed in Figure 6.2.

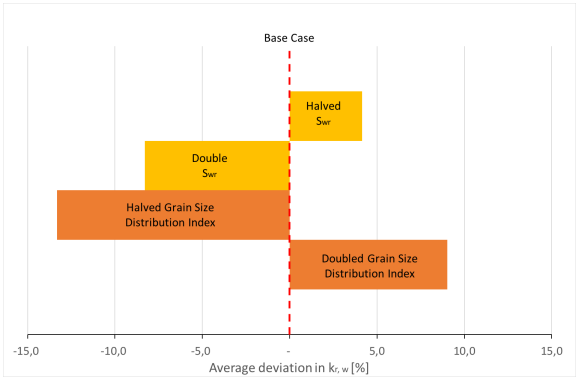

Figure 6.2: Bar diagram showing the average deviation in $k_{r,w}$ $[\%]$, for the different drainage curve scenarios tested in the sensitivity analysis.

A change in the grain size distribution index, λ, will clearly affect the drainage curve the most, according to the bar diagram in Figure 6.2 and the curves in Figure 6.1. This can also be seen from the Corey and Brooks equation where the grain size distribution index is a part of the exponent. In this thesis, the grain size distribution index varies from 0.81 to 3.7. This means that both a doubled and a halved base case λ is realistic. These indexes are not retrieved from samples from the Svelvik test site, but from literature

describing similar grain size distributions. The grain size distribution can be determined from drainage capillary pressure curves like the ones displayed in Figure 2.5 and Equation 2.5 shown in Chapter 2.2.

Since the grain size distribution index, λ, affect the result to the extent shown in Figure 6.2, it is therefore suggested that these curves do not describe the system at the Svelvik ridge, but give an indication of how relative permeability curves as a function of grain size distribution will affect a reservoir with similar properties as the Svelvik ridge. For most simulations results, the changed λ does not affect the saturation profile when compared to the original model. Flow is limited in the vertical direction and the injected gas will mostly flow in the silt below the confining layer. Here, the wetting phase drainage curves are almost equal (λ_{org} = 2, λ_{new}= 1,82), and the reason for the change in the results comes from the simplified original model, and not the grain size distribution itself. The relative permeability as a function of grain size distribution is more relevant in the simulations where the confining layer permeability is reduced and migration patterns are investigated.

A sensitivity analysis was conducted for the calculation of the imbibition curves. Similar to the sensitivity analysis for the drainage curves, a base case with the grain size distribution index for silt and a wetting phase saturation of 0.1 was chosen. In addition, the non-wetting phase residual saturation was set to be 0.25 and the corresponding constant C = 3. In these calculations, the results depend on more parameters than the drainage sensibility study. The ”free” part of the non-wetting saturation is a function of the non-wetting phase residual saturation and the constant C. Therefore, the non-wetting relative permeability was calculated for the the following scenarios:

- Doubled and halved residual non-wetting phase saturation, $S_{nw,r}$
- Doubled and halved residual wetting phase saturation, $S_{w,r}$
- Doubled and halved grain size distribution, λ
- Doubled and halved constant C.

The average deviation from the base case, non-wetting relative permability, in $\%$ is shown in Figure 6.3.

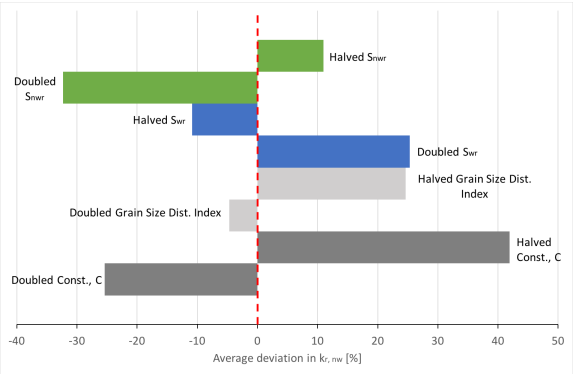

Figure 6.3: Bar diagram showing the average deviation in non-wetting relative permeability [%] for the for different imbibition curve scenarios tested in the sensitivity analysis.

In this sensitivity analysis, when the S_{nwr} was changed, the constant C was changed accordingly to the equation: $C = \frac{1}{S_{nwr}} - 1$. However, when the sensitivity of C was tested, the residual non-wetting saturation, S_{nwr}, was kept constant. As evident from the bar diagram in Figure 6.3 all the parameters are sensitive to change and will affect the result drastically, especially the constant C. For further work, experimental imbibition data should be acquired to be able to calculate a more relevant constant C for the system at the Svelvik ridge. Based on the sensitivity analysis, it is concluded that the imibition curves calculated in this thesis cannot be trusted to represent or describe the system at the Svelvik ridge. However, the results will give an indication of the effect of hysteresis in a similar reservoir.

Based on discussions with Anja Sundal on the interpretation of the Svelvik ridge, it is suggested that there are permeability anisotropy in the north-south and vertical direction, caused by clinoforms, cross lamination and flooding surfaces. In this thesis, this anisotropy is simulated by reducing lateral permeability in the north-south direstion and in the vertical direction. This simplification is not able to describe the angled permeability allowing flow in the direction of the layering caused by the clinoforms. Similar to the imbibition and drainage curves, the anisotropy simulated in this thesis cannot be specifically representative for the Svelvik ridge, as the values chosen for the reduced permeability are based on assumptions. The results will however show a possible effect of the anisotropy that is believed to be present. As described in Chapter 2.2, heterogeneity in form of layers with different permeability has a high influence on pressure build up and storage efficiency. Essentially, the most common effect observed is that heterogeneity could lead to higher capillary trapping as low permeable layers can work as local traps. Simulations ignoring

the effects of heterogeneity will among other things observe significant changes in plume behaviour (Krevor et al., 2015).

It is therefore very important to update the simulation model when new data from the future work on the Svelvik CO_2 Field Lab is acquired. The simulation model and the future geological model can be tested and revised, which makes this research project very interesting. By now, the simulation model where hysteresis and anisotropy in north-south and vertical direction are included, is assumed to be the most detailed and realistic. This model should therefore be tested and revised in future work.

The simulations where the permeability of the confining layers were increased showed that a vertical migration of CO_2 thorugh the confining layer is likely if the permeability of the confining layer is higher than 1 mD. According to Neuzil (1994), which compiled data sets from 12 laboratory studies and 7 field studies that provided ranges of permeability and porosity data in bottom muds, clay, unconsolidated sediment, glacial till, clayey siltstone and sandstone, claystone, mudstone and Argillite, permeability could range from as high as 1 md in unconsolidated sediment with 70 $\%$ porosity and as low as 0.01 nanodarcy (nd) in Argillite with 5 $\%$ porosity. This indicates that migration through the confining layer within the first year is unlikely, unless there are high permeability conducts as eg. fractures through the confining layer. It will be interesting to evaluate possible migration patterns when a new digital geomodel is created, as a more realistic effect of the anisotropy can be simulated.

6.2 Scenario modelling and simulations

The scenario modelling and simulations were conducted to investigate the possibility of approaching the pre-CO_2 injection conditions. Meaning that the water saturation and the formation pressure was identical to the values prior to the CO_2 injection. Since the overlying layer of the injection zone is assumed to be a confining layer, there are no escape of CO_2 in vertical direction in these simulations. The natural migration in the lateral direction is some what limited, therefore two options to accelerate the process of reaching pre-CO_2 injection conditions is evaluated. The first option was to inject water after the injection of CO_2, in an attempt to "push" the CO_2 so far away from the well in a displacement process. The second option was to produce from the well after cessation of the CO_2 injection.

The efficiency of the water injection is limited by the fracture pressure, and the waters ability to displace the CO_2. The fracture pressure was calculated by applying Equations 3.31-3.37 to verify that the previous limit of 10 bar was reasonable. As a simplification, when calculating the overburden stress, it was assumed that the average density of the rock

was equal the density of sandstone, ρ_{rock} = 2100 kg/m^3 (EduMine, 2018).

Since the porosity decline constant, K is not dependant on the fluid occupying the pore space, it is assumed that this will remain constant. It can be seen in Figure 6.4 that a change in this constant, K, will not affect the fracture pressure much. The porosity and the Poisson's ratio are also assumed parameters included in the calculation of the fracturing pressure and the pore pressure is assumed to be hydrostatic. A sensitivity analysis was therefore conducted to investigate the effect of these assumed parameters on the fracture pressure. In Figure 6.4 the deviation in the fracture pressure [%] for the following scenarios for the different parameters calculated on injection depth is presented:

- Doubled and halved porosity decline constant, K.
- Doubled and halved porosity, ϕ.
- Doubled and halved pore pressure, P_c.
- Doubled and halved rock density, ρ_{rock}.
- Doubled and halved Poisson's ratio, μ.

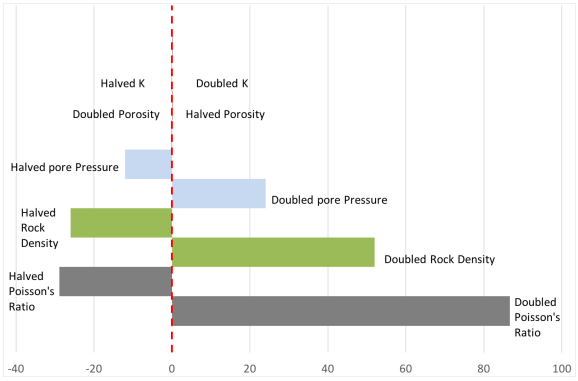

Figure 6.4: Bar diagram showing the deviation in fracture pressure in % for the for different scenarios of fracture pressure calculations at injection depth.

From this figure, it is clear that a change in the porosity decline constant, K, or the porosity, ϕ, will not affect the fracturing pressure much, as a doubled or halved K or ϕ will result in a near to zero change in the fracturing pressure. The pore pressure, rock density and the Poisson's ratio, are sensitive parameters when the fracture pressure is calculated. This determination of the fracture pressure can not be trusted to be a valid limit for a real injection at Svelvik, due to the insecurities in sensitive parameters. The calculations were

conducted to verify the validity of the predetermined bottom hole pressure limit of 10 bar. Since the calculated fracture pressure was higher than 10 bar, the 10 bar limit was used in all simulations.

This pressure limit inhibits the displacing effect of the water injection, as it results in a very low injection rate. Figure 5.11 shows the decreasing gas in place within a 50m x 50m square with the well in the center for different injection rates. The feature that stands out is that none of the tested rates displace CO_2 effectively, even though the fracture pressure limit is exceeded. From these simulations, the result is that there is almost no difference in displacement by water and natural migration. With an increasing water injection rate, the relative permeability of water increase faster, and less CO_2 will be displaced. The bottom hole pressure curves in Figure 5.12 shows that all the tested rates exceed the fracture pressure limit. The rate limited by the calculated fracture pressure is very low, and in Figure 5.10 it is clear that the effect of the injection becomes smaller and smaller as we move further away from the well. After 63 days of water injection limited by the calculated fracture pressure, the gas in place is decreased by 6.8% relative to natural migration in the 30m x 30m region. For the 50m x 50m region the gas in place is 2.8% lower, and for the 100m x 100m it is only 0.9%. The efficiency of the displacement can be increased by eg. adding surfactants to the injection water, but in a realistic case, the CO_2 saturation for the reservoir will not be reduced to a residual saturation. Another point to make is that the chance of more residual trapping can increase. As stated in Krevor et al. (2015), injection of brine after the injection of CO_2 is also an option as this will lead to an imbibition process increasing snap-off and capillary trapping.

The other option to reduce the CO_2 saturation of the reservoir, after cessation of the CO_2 injection, is to produce from the reservoir. This was simulated and investigated by producing at different rates, for different models, and for different perforation depths.

As assumed, the gas production was more effective when the production rate was increased and when the perforation depth was changed. With an increasing production rate, more of the CO_2 would be produced. The increased production efficiency caused by the changed perforation depth was also evident. The CO_2 saturation under the confining layer was greater than on 65m, hence more gas could be produced out. If production of the injected CO_2 is to be initiated, this solution should be further investigated and considered.

In Figure 5.19, production of gas simulated by using the original model and the updated model is shown. By comparing these, it can be seen that the production from the reservoir is greater in the updated model. To understand this, one can look at the productivity index, PI = $\frac{Q}{\Delta p}$. The productivity index can also be expressed as a function of permeability, net thickness, fluid viscosity, formation volume factor, external boundary radius, wellbore

radius and skin factor.

Many of these parameters are equal for the two models, but the differences in the saturation profile around the well, caused by a change in the relative permeability, will result in a higher water cut in the production stream in the original model. A higher fraction of water will increase the average viscosity of the stream and require a higher drawdown to maintain the production rate. This could be a reason for the differences in production efficiency.

For all the scenario simulations, the results are based on the updates in model, hence they are dependant of the updates being correct, and that they are representative for the Svelvik ridge system. In addition to this, both the limits set for the injection pressure and the production rate are calculated based on a number of assumptions, and no safety factors are included. Therefore, these limits are not limits recommended as actual limits for real injection or production tests, but limits for rates of possible scenarios for illustrative purposes.

To verify and evaluate the accuracy of the updates of this model, the simulation results can be compared with observations from the shallow injection test conducted in the previous CO_2 Field Lab project. When tests are conducted at the test site in the future, this model should be reviced.

Chapter 7

Conclusion

The simulations, calculations, assumptions and literature study in this thesis was conducted in an attempt to increase the resolution and accuracy of the simulation model describing a CO_2 injection in the Svelvik ridge. The original simulation model from the CO_2 Field Lab project was revised. The updated model has a relative permeability as a function of grain size distribution, hysteresis is included, and anisotropy is simulated in north-south and vertical direction. If the saturation profiles around the well from the updated model is compared with the original model, there are many similarities. It is obvious that the assumptions and ideas behind the original model was well considered. It will therefore be very interesting to be able to compare these simulation models with the observations from the future injection tests in the Svelvik CO_2 Field Lab. Despite similarities there are clear differences in the models. When anisotropy is not included, one can see that the CO_2 in the new model with hysteresis included is more mobile than in the original model as can be seen in Figure 5.3 and 5.2. These differences are also evident in the scenario simulations.

The ability to produce the CO_2 from the reservoir was much greater in the updated model than in the original. The water was also able to displace the CO_2 more efficiently during the water injection in the updated model, than in the original model. To inject water with the same rate, the updated model needed a higher injection pressure than the original model, caused by reduction of directional permeability to simulate anisotropy. For the same reason, the updated model needed a higher drawdown to be able to produce at the same rate as the original model.

Based on the results of the scenario simulations, injection of water to reduce the CO_2 saturation in the reservoir by displacement is not recommended as an option. This is primarily based on the low injection rate caused by the low bottom hole pressure limit, caus-

ing the displacement of CO_2 to be inefficient. If production from the reservoir is evaluated as a solution to reduce the CO_2 saturation, perforations right beneath the confining layer should be considered. This will allow for the accumulation of CO_2 under the confining layer, caused by stratigraphic trapping, to be produced.

The results of the simulations with increased permeability in the confining layers, indicates that migration through the confining layer within the first year is unlikely, unless there are high permeability conducts as eg. fractures through the confining layer. It will be interesting to evaluate possible migration patterns when a new digital geomodel is created, as a more realistic effect of the anisotropy can be simulated.

Based on the sensitivity analysis in the previous chapter, it is concluded that the imibition and drainage curves calculated in this thesis cannot be trusted to represent or describe the system at the Svelvik ridge. However, the results will give an indication of the effect of relative permeability as a function of grain size distribution and hysteresis in a system similar to the Svelvik ridge. Similar to the imbibition and drainage curves, the anisotropy simulated in this thesis is not representative for the Svelvik ridge, as the values that are chosen for the reduced permeability are based on assumptions. The results will however show a possible effect of the anisotropy that is believed to be present.

The scenario simulations are based on the updates in the model, hence they are dependant of the accuracy in the updates, and that the updates are representative for the Svelvik ridge system. In addition to this, both the limits set for the injection pressure and the production rate are calculated based on a number of assumptions, and no safety factors are included. In conclusion, these limits are not limits recommended as actual limits for real injection or production tests, but limits to illustrate possible injection or production scenarios.

Based on this, it is important to update the simulation model when new data from the future tests on the Svelvik CO_2 Field Lab project is acquired. The simulation model and the geological model can be tested and revised, which makes this research project very interesting. By now, the updated simulation model where hysteresis and anisotropy in north-south and vertical direction are included, is assumed to be the most detailed and realistic model. This model should therefore be tested and revised in future work.

Chapter 8

Recommendations for Further Work

The updates and changes done on the simulation model in this thesis has much room for improvement. As seen from the sensitivity analysis, the assumptions in the different calculations needs to be very accurate for this model to be a representative model for the Svelvik ridge. Some of the work that is recommended to be evaluated and improved is mentioned in this section.

The imbibition curves are one of the updates that affect the model to a large extent, as seen in Figure 5.3. By conducting laboratory experiments to get more knowledge of these curves and the systems relative permeability behaviour would be very beneficial. Experimental data could be gained, and hence imbibition curves could be calculated eg. by using Killoughs normalized experimental data method. Experimental data would also open up possibilities to calculate a more accurate and realistic constant, C, from Equation 3.4. According to the conducted sensitivity analysis shown in Figure 6.3, this constant is a sensitive and important parameter in the imbibition curves calculations. If more than one CO_2 injection is conducted at the site, it could be interesting to investigate the imbibition curves for the wetting phase. These could be calculated by using Lands proposal with Equation 3.8-3.12. The effect of the capillary pressure should also be investigated. In this thesis, only one capillary pressure curve is used in combination with one set of relative permeability curves. The rest of the capillary pressure curves are defaulted. By gaining knowledge about the capillary pressure curves, one could also gain information to calculate a more accurate grain size distribution index by using Equation 2.4.

An updated geomodel is a crucial part of the improvement of the simulation model. Anja Sundal is currently working on a geomodel describing the Svelvik ridge, where anisotropy caused by a complex depositional environment is modelled. The migration pattern displayed in Figure 5.8 could be very different if the anisotropy is modelled as the actual clinoforms in the geomodel. This geomodel should be tested in simulations and compared to the anisotropy simulations from this thesis and to future observations from the injection tests at the Svelvik CO_2 Field Lab. The geomodel and the possible future improved simulation model could also be compared to the observations from the shallow injection conducted in 2011.

From 7th to 12th September 2011, 1.7 tonnes of CO_2 were injected with a wellhead pressure of 1.9-2 bar at a depth of 20 m. The shallow subsurface was monitored using both geophysical and geochemical methods. This test differs from the planned injection in the Svelvik $\#2$ well in some specific ways. There were no confining layer in the 2011 shallow injection, and the CO_2 could migrate freely through the subsurface and out of the ground. It is therefore not that relevant to compare the CO_2 plumes of the simulation of an injection at 65m under an confining layer to the actual 2011 shallow injection. To make this interesting, a reviced model of the shallow subsurface should be made using the same updates as the one made in this thesis. These updates should include the same change in the relative permeability with respect to the grain size distribution index and the effect of hysteresis. Anisotropy similar to the one implemented in this thesis and a future digital geomodel should also be included. This simulation model should then be compared to the observations from the 2011 shallow injection, to see if the updates will result in a more accurate simulation.

In conjunction with the further work on the simulation model, the realism of the scenario modelling could be improved. If injection of water or production from the reservoir, or both, are being realized, the associated limits with improved accuracy and safety factors should be included in the simulations. Lastly, sand production prediction models should be developed to see if there is a risk of sand production, and if so, the severity of it.

Bibliography

Assouline, S., 2005. On the relationships between the pore size distribution index and characteristics of the soil hydraulic functions. Water resources research 41 (7).

Bachu, S., 2015. Review of CO_2 storage efficiency in deep saline aquifers. International Journal of Greenhouse Gas Control.

Barker, J., 2011. Glacial-marine Deposits of Southern Maine. Accessed: 23-04-2018.
URL http://academic.emporia.edu/aberjame/student/barker3/maine.html

Bates, C. C., 1953. Rational theory of delta formation. AAPG Bulletin 37 (9), 2119–2162.

Blunt, M. J., 2017. Multiphase flow in permeable media: A pore-scale perspective. Cambridge University Press.

Bourgoyne Jr., A. T., Chenevert, M. E., Millheim, K. K., Young Jr., F., 1986. Applied Drilling Engineering, SPE Textbook Series VOL.2.

Brown, G., 2000. Henry Darcy and His Law, The Darcy-Weisbach Equation. Accessed: 30-05-2018.
URL https://bae.okstate.edu/faculty-sites/Darcy/DarcyWeisbach/Darcy-WeisbachEq.htm

Carlson, F. M., et al., 1981. Simulation of relative permeability hysteresis to the non-wetting phase. In: SPE annual technical conference and exhibition. Society of Petroleum Engineers.

Chadwick, A., Arts, R., Bernstone, C., May, F., Thibeau, S., Zweigel, P., 2017. Best Practise For the Storage of CO_2 in Saline Aquifers, Observations and Guidelines From

the SACS and CO2STORE Projects. Accessed: 17-11-2017.
URL http://www.co2store.org/TEK/FOT/SVG03178.nsf/Attachments/CO2STORE_Best_Practice_Manual_2007_revision_1.pdf/$$$FILE/CO2STORE_Best_Practice_Manual_2007_revision_1.pdf

Corey, A., Brooks, R., 1964. Hydraulic Properties of Porous Media. Colerado State Univeristy.

EduMine, 2018. Specific Gravity and Porosity of Various Rock Types. Accessed: 12-02-2018.
URL http://www.edumine.com/xtoolkit/tables/sgtables.htm

Gladfelter, R. E., Gupta, S. P., et al., 1980. Effect of fractional flow hysteresis on recovery of tertiary oil. Society of Petroleum Engineers Journal 20 (06), 508–520.

Global CCS Institute, G., 2017. Paris climate change targets cannot be met without CCS: COP23. Accessed: 05-12-2017.
URL https://www.globalccsinstitute.com/sites/www.globalccsinstitute.com/files/content/mediarelease/123543/files/global-status-ccs-2017.pdf

Grimstad, A.-A., 2013. Report D4.4.1D, Project NO. 7020087, Deep geomodel – final version.

Grimstad, A.-A., Polak, S., 2013. Report D4.4.1B, Project NO. 7020087, Shallow geomodel – final version.

Hoff, K. A., 2017. CO_2 capture – Absorption Processes - SINTEF. Accessed: 12-10-2017.
URL https://www.sintef.no/en/co2-capture-absorption-processes/

Institute, G. C., 2018. CO_2 Terminal. Accessed: 30-05-2018.
URL http://hub.globalccsinstitute.com/publications/co2-liquid-logistics-shipping/-concept-llsc-overall-supply-chain-optimization/53-co2

Jerauld, G., et al., 1997. General three-phase relative permeability model for Prudhoe Bay. SPE reservoir Engineering 12 (04), 255–263.

Jordan, M., Grimstad, A.-A., Lindeberg, E., Romdhane, A., Eliasson, P., Querendez, E., 2015. Project Memo, CO_2 Monitoring at the CO_2 Field Lab Test Site in Svelvik: Feasibility study of an air injection at 65m depth.

Killough, J., et al., 1976. Reservoir simulation with history-dependent saturation functions. Society of Petroleum Engineers Journal 16 (01), 37–48.

Krevor, S., Blunt, M. J., Benson, S. M., Pentland, C. H., Reynolds, C., Al-Menhali, A., Niu, B., 2015. Capillary trapping for geologic carbon dioxide storage - From pore scale physics to field scale implications.

Krzemień, e. a., 2013. Risk assessment of a post-combustion and amine-based co2 capture ready process. Journal of Sustainable Mining 12 (4), 18–23.

Kudela, H., 2001. Hydraulic losses in pipes. Accessed: 30-05-2018.
URL http://fluid.itcmp.pwr.wroc.pl/~{}znmp/dydaktyka/fundam_FM/Lecture11_1

Land, C., 1968a. Calculation of Imbibition Relative Permeability for Two- and Three-Phase Flow From Rock Properties. Society Of Petroleum Engineers Journal.

Land, C., 1968b. The optimum gas saturation for maximum oil recovery from displacement by water. 43rd Annual Fall Meeting of SPE of AIME.

Lønne, I., 1993. Sedimentary facies and depositional architecture of ice-contact glaciomarine systems. Dr. Scient Thesis, Department of Soils and Water Sciences, Agricultural University of Norway. Ås.

Mathews, J. H., Fink, K. K., 2004. Numerical Methods Using Matlab, 4 th Edition.

Melø, T., 2011. Hydrogeology of the shallow aquifer at the Svelvik ridge. Master's thesis.

Morita, N., et al., 1994. Field and laboratory verification of sand-production prediction models. SPE Drilling & Completion 9 (04).

Neuzil, C., 1994. How Permeable Are Clays and Shales? Water Resources Research 30 (2).

NGU, 2018. Maps and Data, Norges geologiske undersøkelse (Norwegian Geological Survey). Accessed: 23-04-2018.
URL http://geo.ngu.no/kart/minkommune/?kommunenr=628

Norwegian Petroleum Directorate, 2017. Myths and facts about CO2 storage - Norwegian Petroleum Directorate. Accessed: 03-09-2017.
URL http://www.npd.no/en/Topics/Storage-and-use-of-CO2/Temaartikler/Myths-and-facts-about-CO2-storage/

Palmer, A., Doctor, R., 2017. IPCC Special Report on Carbon dioxide Capture and Storage, Transport of CO_2. Accessed: 01-10-2017.
URL https://www.ipcc.ch/pdf/special-reports/srccs/srccs_chapter4.pdf

Pettersen, Ø., 2006. Basic Reservoir Simulation With the Eclipse Reservoir Simulator, Lecture Notes. Dept. of Mathematics, Univ. of Bergen.

Rendall, H., 2012. Project NO. 7020087, Memo, Laboratory measurements of spectral gamma radiation and grain size.

Ringstad, C., 2017. Kickoff Presentation, Svelvik CO_2 Field Lab.

Rodoste, T., 2010. Monitoring Techniques for the Validation Phase Michigan Carbon Dioxide Storage Field DemonstrationAccessed: 13-10-17.
URL https://irp-cdn.multiscreensite.com/5b322158/files/uploaded/Fact%20sheet%20on%20monitoring%20techniques.pdf

Röhnert, A. D., 2016. Geometry and sedimentary facies of low-angle clinoforms, Edgeøya, Svalbard. Master's thesis.

Ruden, F., 2010. Supervision Report, completion of the Svelvik Appraisal Well (Svelvik CO_2).

SCCS, 2015. CO_2MultiStore Joint Industry Project. Accessed: 10-11-2017.
URL http://www.sccs.org.uk/expertise/reports/co2multistore-joint-industry-project

Schaerer, C. E., Marchesin, D., Sarkis, M., Bedrikovetsky, P., 2006a. Permeability hysteresis in gravity counterflow segregation. SIAM Journal on Applied Mathematics 66 (5), 1512–1532.

Schaerer, C. E., Marchesin, D., Sarkis, M., Bedrikovetsky, P., 2006b. Permeability hysteresis in gravity counterflow segregation. SIAM Journal on Applied Mathematics 66 (5), 1512–1532.

Schlumberger, 2015. Eclipse, Technical Description, Version 2015.1.

Standing, M., 1975. Notes on relative permeability relationships. Lecture Notes, Trondheim, Norway.

Standing, M., 1981. Volumetric and phase behavior of oil field hydrocarbon systems.

Standing, M. B., Katz, D. L., et al., 1942. Density of natural gases. Transactions of the AIME 146 (01), 140–149.

STEMM-CCS, 2017. Sub-seabed carbon dioxide storage — STEMM-CCS. Accessed: 01-09-2017.
URL http://www.stemm-ccs.eu

Sundal, A., 2017. Preliminary work on geomodelling of the Svelvik ridge, not published.

Sørensen, R., 1981. Foreløpig beskrivelse til kvartærgeologisk kart SVELVIK – CL 083, M1:10 000 Norges geologiske undersøkelse, Rapport 1807/7 -1981.

Sørensen, R., Lie, K., Nybakken, S., 1990. DRØBAK 1814 II, kvartærgeologisk kart – M 1 :50 000. Norges geologiske undersøkelse.

Torland, A., 2018. Preliminary work on pore network modelling, not published.

UNFCCC, 2017. UNFCCC, The Paris Agreement. Accessed: 01-10-2017.
URL http://unfccc.int/paris_agreement/items/9485.php

U.S. Energy Information Administration, 2017. International Energy Outlook (2017). Accessed: 14-10-2017.
URL https://www.eia.gov/outlooks/ieo/pdf/0484(2017).pdf

Whitson, C. H., Brulé, M. R., 2000. Phase behavior. Henry L. Doherty Memorial Fund of AIME, Society of Petroleum Engineers Richardson, TX.

Appendix

8.1 Numerical solutions in Eclipse

Eclipse is a industry-reference reservoir simulator. To understand how the simulator will solve the problems numerically, one can look at the model equation. The 3D model equation in Eclipse is given as:

$$\frac{\delta u}{\delta t} = \frac{\delta^2 u}{\delta x^2} + \frac{\delta^2 u}{\delta y^2} + \frac{\delta^2 u}{\delta z^2} \tag{8.1}$$

The central differences for the spatial approximation and forward difference in time, and hence the finite difference approximation to Equation (8.1) can be found with a Taylor series expansion:

$$f(x+h) = f(x) + f'(x)h + \frac{f''(x)h^2}{2!} + \frac{f'''(x)h^3}{3!} + ... \tag{8.2}$$

$$f'(x) = \frac{f(x+h) - f(x)}{h} + O(h) \tag{8.3}$$

Where:

O(h) = Error term of order (h)

h = Step length

The second derivative can be found by summing Equation (8.2) with the following equation:

$$f(x-h) = f(x) - f'(x)h + \frac{f''(x)h^2}{2!} - \frac{f'''(x)h^3}{3!} + ... \tag{8.4}$$

Resulting in Equation (8.5):

$$f(x+h) + f(x-h) = 2f(x) + f''(x)h^2 + ...$$

$$f''(x) = \frac{f(x+h) + f(x-h) - 2f(x)}{h^2} + O(h^2) \tag{8.5}$$

The finite difference approximation to Equation (8.1) can then be written as Mathews and Fink (2004):

$$\frac{u_{i,j,k}^{n+1} - u_{i,j,k}^{n}}{\Delta t} = \frac{u_{i+1,j,k} + u_{i-1,j,k} - 2u_{i,j,k}}{\Delta x^2} + \frac{u_{i,j+1,k} + u_{i,j-1,k} - 2u_{i,j,k}}{\Delta y^2} + \frac{u_{i,j,k+1} + u_{i,j,k-1} - 2u_{i,j,k}}{\Delta z^2} \tag{8.6}$$

The superscript "n" in Equation (8.6) denotes the time step. If the right side of the equation is evaluated at time step n, the equation is solved *explicitly* for the solution $u_{i,j,k}^{n+1}$, which makes it possible to find the solution at time n+1 for all the cells (i,j,k). A problem with an explicit scheme is that once an error develops, it will grow with time. Explicit schemes are therefore seldomly used.

If the right side of Equation (8.6) is solved at time step n+1, all terms but $u_{i,j,k}^{n}$ are unknown. This is an *implicit* formulation of the problem. The implicit solution is more stable than the explicit solution. When an error occurs the implicit scheme corrects itself with time and approach the correct solution, unlike the explicit. The implicit scheme is default in Eclipse, but IMPES is an available option. IMPES stands for implicit pressure, explicit saturation. As the name implies, IMPES is a method in between explicit and implicit, a mixture of both. It is a nummerical method where the pressure is solved implicitly and the saturation is updated explicitly. IMPES has some of the advantages of the Implicit method and requires less computational work.

To illustrate, Figure 8.1 shows the system structure for a grid with 3 cells in x-direction, 3 cells in y-direction and 3 cells in z-direction. To solve the system given in Equation (8.6), it is apparent that the relevant cells for the calculations are found by using the seven point stencil. To compute the value of cell (i,j,k) the values of the cells (i$\pm$1,j,k), (i,j$\pm$1,k) and (i,j,k$\pm$1) are needed.

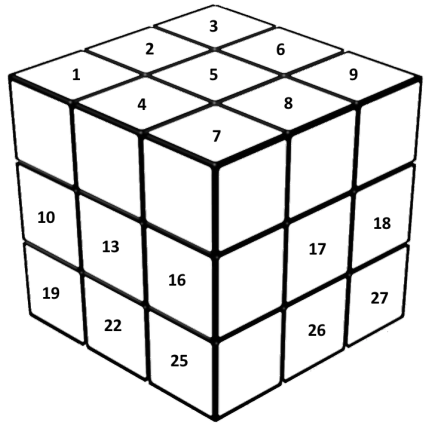

Figure 8.1: Cube showing system structure for a grid with 3x3x3 cells.

In Figure 8.1, it is clear that cell (1,1,1) is dependant of (2,1,1), (1,2,1) and (1,1,2) which is equivalent to cell 1 being dependant of cell 2, 4 and 10. By following this system, a matrix like the one presented in Figure 8.2 can be acheived.

	1	2	3	4	5	6	7	8	9	10	11	12	13	14	15	16	17	18	19	20	21	22	23	24	25	26	27
1	X	X		X						X																	
2	X	X	X		X						X																
3		X	X			X						X															
4	X			X	X		X						X														
5		X		X	X	X		X						X													
6			X		X	X			X						X												
7				X			X	X								X											
8					X		X	X	X								X										
9						X		X	X									X									
10	X									X	X		X						X								
11		X								X	X	X		X						X							
12			X								X	X			X						X						
13				X						X			X	X		X						X					
14					X						X		X	X	X		X						X				
15						X						X		X	X			X						X			
16							X						X			X	X								X		
17								X						X		X	X	X								X	
18									X						X		X	X									X
19										X									X	X		X					
20											X								X	X	X		X				
21												X								X	X			X			
22													X						X			X	X		X		
23														X						X		X	X	X		X	
24															X						X		X	X			X
25																X						X			X	X	
26																	X						X		X	X	X
27																		X						X		X	X

Figure 8.2: Coefficient matrix for the grid system in Figure 8.1. ”X” denotes a non-zero value.

As the figure demonstrates, most entries in the system are zero. There are seven row entries with values, and these are following a diagonal pattern. Therefore, this kind of

matrix are often called a 7-diagonal matrix. The goal by making such a matrix is to get a structure which is optimal for some solution procedure. This may seem unproblematic, but is in reality a bit more difficult due to the complexity of the Black oil equations. Each element in the matrix is actually a 3x3 matrix, or in our case, a 2x2 matrix since there are only two phases in our system. Due to coupling between saturation and pressure (eg. capillary pressure) and saturation dependant coefficients, the Black oil equations contain non-linear terms. The system in Figure 8.2 is therefore not a linear system of equations known from linear algebra. The fact that representation of fractures and faults in the numerical model requires more complex grid structures, breaks up the purity of the diagonals, by creating non-zero entries outside the diagonal, and zeros in the diagonal pattern. Grids with non-neighbouring connections can therefore not be solved by the specialized methods to solve the 7-diagonal matrices.

There are many ways to solve non-linear problems. One popular technique is the Newton-Raphson method. This method can best be described through an example. The problem is to solve the equation $f(x) = 0$, where the function $f(x) = y$ is showed on figure 8.3. The algorithm to solve this by the Newton-Raphson method is then as follows:

1. Choose an appropriate starting point x^0 and the corresponding $f(x^0)$.

2. Find the tangent to f(x) in the point $[x^0, f(x^0)]$.

3. Find the intersection between this tangent and the x-axis, x^1 as shown on figure 8.3.

4. Repeat this until $f(x^n)$ is equal to zero, within tolerance.

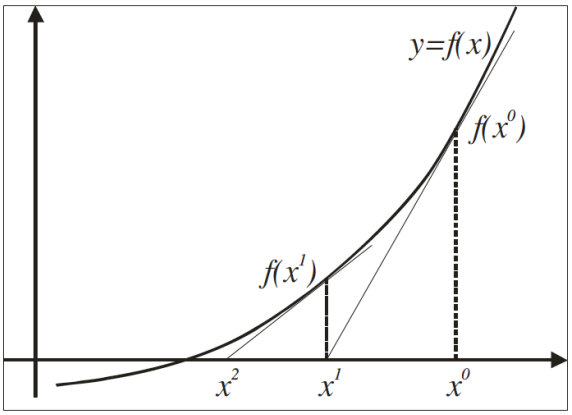

Figure 8.3: Graph illustrating the Newton-Raphson method.

From Figure 8.3Pettersen, Ø. (2006), it can easily be seen that the solution will converge against the solution. The tangent equation is given by $y = f(x^0) + f'(x^0) \cdot (x - x^0)$, and the point x^1 is found by setting y=0 in the tangent equation such that

$$x^1 = x^0 - \frac{f(x^0)}{f'(x^0)} \tag{8.7}$$

A stop criterion should be defined so that $|f(x^n)| < \epsilon$, where ϵ is an error tolerance.

This system can be used to solve non-linear equations. The idea is somewhat the same, but the solution for a system wil be more complex. The non linear problem is:

$$\begin{aligned} F_1(x) &= 0 \\ F_2(x) &= 0 \\ F_3(x) &= 0 \\ &\cdot \\ &\cdot \\ &\cdot \\ F_n(x) &= 0 \end{aligned} \tag{8.8}$$

The system is equivalent to the derivative of f is the total differential of the F_n. Assuming that the value of x after i iterations is x^i, the equivalent of the tangent in Equation 8.7 is:

$$\frac{dF}{dx}(x^i) \cdot \Delta x^i + F(x^i) = 0$$

And if the equation is expanded it becomes:

$$\begin{aligned} &\frac{dF_1}{dx_1}(x^i)\Delta x_1^i + \frac{dF_1}{dx_2}(x^i)\Delta x_2^i + \cdots + \frac{dF_1}{dx_n}(x^i)\Delta x_n^i + F_1(x^i) = 0 \\ &\frac{dF_2}{dx_1}(x^i)\Delta x_1^i + \frac{dF_2}{dx_2}(x^i)\Delta x_2^i + \cdots + \frac{dF_2}{dx_n}(x^i)\Delta x_n^i + F_2(x^i) = 0 \\ &\cdot \\ &\cdot \\ &\cdot \end{aligned} \tag{8.9}$$

$$\frac{dF_n}{dx_1}(x^i)\Delta x_1^i + \frac{dF_n}{dx_2}(x^i)\Delta x_2^i + \cdots + \frac{dF_n}{dx_n}(x^i)\Delta x_n^i + F_n(x^i) = 0$$

Hence, the equivalent of Equation 8.7 is to solve equation 8.9 with respect to $\Delta(x^i)$. The solution vector can be updated with $x^{i+1} = x^i + \Delta x^i$, and the iterations continue until $||F(x^i)|| < \varepsilon$, where ε is a preferred error term. The double vertical lines around the expression ($||*||$) represents a norm, e.g $||F|| = \Sigma|F_i|$. Solving equation 8.9 with respect to $\Delta(x^i)$, is where the major part of the work in simulations is required.

To apply this to the Black oil equations, one can start by looking at the following black oil difference equations with dissolved gas:

For water and/or oil:

$$\Delta T_l \Delta \psi_l + q_{l,ijk} = C_{ijk}\Delta_t(\phi S_l b_l) \tag{8.10}$$

For gas:

$$\Delta T_g \Delta \psi_g + \Delta R_s T_o \Delta \psi_o + q_{g,ijk} = C_{ijk}\Delta_t(\phi S_g b_g + \phi R_s S_o b_o) \tag{8.11}$$

Where:

$\Delta T \Delta \psi = \Delta_x T_x \Delta_x \psi + \Delta_y T_y \Delta_y \psi + \Delta_z T_z \Delta_z \psi$
T = Transmissibility, a measure of the conductivity of the formation corrected for the viscosity of the
ψ = Fluid potential, the mechanical energy per unit mass.
b_l = Inverse of formation volume factor, $\frac{1}{B_l}$ = $\frac{st.voll}{res.voll}$
$C_{ijk} = (\Delta x_i \Delta y_j \Delta z_k)/\Delta t$ (for a rectangular cartesian grid).
R_s = Solution gas-oil ratio, $\frac{st.vol.gas}{st.vol.oil}$
q = Flow rate, volume of fluid per unit time
S = Saturation
ϕ = Porosity

By rewriting Equation 8.10 and 8.11, we can define functions F_1, F_2 and F_3:

$$F_1 = \Delta T_w \Delta \psi_w + q_{w,ijk} - C_{ijk}\Delta_w(\phi S_w b_w) \tag{8.12}$$

$$F_2 = \Delta T_o \Delta \psi_o + q_{o,ijk} - C_{ijk}\Delta_o(\phi S_o b_o) \tag{8.13}$$

$$F_3 = \Delta T_g \Delta \psi_g + \Delta R_s T_o \Delta \psi_o + q_{g,ijk} - C_{ijk}\Delta_t(\phi S_g b_g + \phi R_s S_o b_o) \tag{8.14}$$

So that $F_i = 0$ for i=1,2,3. The phase pressures and fluid saturations for the three phases are primary unknowns, resulting in a independent vector variable of v = (p_w, p_o, p_g, S_w, S_o, S_g). p_o and p_g can be determined from capillary pressure, and S_o can be determined from $S_o = 1 - (S_w + S_g)$. By implementing this, the first equation in the system shown in Equation 8.9 becomes:

$$\frac{dF_1}{dp_w}\Delta p_w + \frac{dF_1}{dp_o}\Delta p_o + \frac{dF_1}{dp_g}\Delta p_g + \frac{dF_1}{dS_w}\Delta S_w + \frac{dF_1}{dS_o}\Delta S_o + \frac{dF_1}{dS_g}\Delta S_g + F_1 = 0 \quad (8.15)$$

Which can be rewritten as:

$$\bigtriangledown_v F_1 \cdot \Delta v + F_1 = 0 \quad (8.16)$$

Imagine that we are iterating on *v*, and the solution at the current iteration is v^i. The next Newton-Raphson iteration is then:

$$\sum_{c \epsilon CC} (\bigtriangledown_v F_m \cdot \Delta v)_c^i + F_m^i = 0, m = 1, 2, 3 \quad (8.17)$$

$c \epsilon CC$ denotes that the "cell c is in the computational cube", meaning that the 7-point stencil is centered at c. This is a linear system that can be solved by a variety of techniques, e.g. the Gauss-Seidel method, which will not be discussed in detail in this thesis. In the simulation of the CO_2 injection at Svelvik, there are only two phases present (water and CO_2), hence only Equation 8.12 and 8.14 will be used, which will make the equation system simpler.

To complete this short and brief explanation of the numerical approach to solving flow equations in Eclipse, it is natural to look at the summary of the procedure for advancing the solution one time step by the Newton-Raphson method:

1. Formulate the problem (Equation 8.16), with the current values of the v-vector as start-values.
2. Solve the problem by the Newton-Raphson method by formulating a tangent equation (Equation 8.17) and solving it for Δv^i.
3. Check error criterion $||F(v^i)|| < \varepsilon$
4. If the solution has not converged, update v-vector and repeat from 1.

When the solution has converged, we say that a solution is found by iteration according to the Newton-Raphson scheme. In Eclipse terminology, these iterations are called

Newton-iterations Pettersen, Ø. (2006).

8.2 Eclipse data file

The data file below was used for the simulation of a CO_2 injection where anisotropy and hysteresis were included. The CO_2 injection lasted for 63 days, and then the well was shut for 63 days.

```
RUNSPEC
TITLE
Svelvik: CO2 injection into sand-rich layer at 60-70 m. No dip.
-- Anisotropy in north-south and vertical direction and hysteresis included.

DIMENS
 40 40 61 /

OIL
GAS

UNIFIN
UNIFOUT

METRIC

TABDIMS
-- Table Of Dimensions
-- NTSFUN  NTPVT  NSSFUN  NPPVT NTFIP NRPVT
-- ------  -----  ------ -----  ----- -----
     8       1      25     10     2     7/
-- NTSFUN: No. of saturation tables entered.
-- NTPVT : No. of PVT tables entered (in the PROPS section).
-- NSSFUN: Max. no. of saturation node in each saturation table, ie.,
--         Max. no. of data points in each table.
-- NPPVT : Max. no. of pressure nodes in any PVT table
-- NTFIP : Max. no. of FIP regions def using FIPNUM in REGIONS section
-- NRPVT : Max. no. of Rs nodes in any live oilpvt table

EQLDIMS
```

```
----NTEQUL  Internal    Max depht
--      p-nodes   nodes in RSVD
     1         1*           2           /

REGDIMS
   2 /
SATOPTS
HYSTER/

START
1     JUL    2014  12:00:00.0/

NSTACK
 200 /
--=================================================================
GRID
--=================================================================
INCLUDE
'Dip0full$\_$Grid.incl' /


INIT

--Svelvik properties
INCLUDE
'Dip0full$\_$Props.incl' /

COPY
 PERMX PERMY /
 PERMX PERMZ /
```

```
/

-- Inactive layers 61
ACTNUM
 96000*1 1600*0 /


BOX
    1  40  1  40  1 61 / -- Everything
MULTPV
  97600*10.0/

BOX
  2 39 2 39 2 60 / -- Interior
MULTPV
  85196*1.0 /

-- Reducing permeability in injection zone to simulate anisotropy
BOX
  2 39 2 39 51 60 / -- injection zone
PERMZ
  14440*10.0/

PERMX
  14440*10.0 /


ENDBOX

--================================================================
```

```
PROPS
----------------------------------------------------------------

DENSITY
 999.1026   0.0000      1.842 / -- Water and CO2


-- Reservoir temperature:  Hurdal gradient (NGU)

PVDO
--     Pressure        Bo   Viscosity
--       bar       Rm3/Sm3        mPa s
1.01325         1.000000  1.30888476
1.994283024 0.999981  1.29754392
3.956400703 0.999948  1.27600000
5.937769034 0.995000  1.27555917
6.928962038 0.990000  1.26490507
7.920155776 0.989800  1.25439500
8.911349167 0.989600  1.24402637
/

PVDG
--      Pressure       Bg         Visosity
--    bar      Rm3/Sm3        mPa s
1.01325         1.000000  0.0147
1.994283  0.506814        0.0147
2.975334  0.336788  0.0147
3.956401  0.251095  0.0147
4.946578  0.199082  0.0147
5.937769  0.164397  0.0147
```

```
6.928962  0.139643  0.0147
7.920156  0.121091  0.0147
8.911349  0.106672  0.0147
/


ROCK
-- Pref     Compressibility
   5.0       1.0E-04  /

-- Saturation Dependent Data


SOF2
-- Oil Saturation Functions (2-phases)
--  So      Krog
-- ----    -------
-- Corey: end point saturations 0.1 and 1.0; exponent 4
--drainage 1:Fine Sand, 2: Silt, 3: Sandy Clay, 4: Sandstone
-- Imbibition  5:Fine Sand, 6: Silt, 7: Sandy Clay, 8: Sandstone
--1
   0.00    0.00000
   0.05    0.00000
   0.10    0.00000
   0.15    0.00004
   0.20    0.00042
   0.25    0.00176
   0.30    0.00487
   0.33    0.00798
   0.35    0.01072
```

```
    0.40    0.02045
    0.45    0.03530
    0.50    0.05663
    0.55    0.08594
    0.60    0.12480
    0.65    0.17488
    0.70    0.23798
    0.75    0.31595
    0.80    0.41074
    0.85    0.52439
    0.90    0.65901
    0.95    0.81679
    0.97    0.88689
    1.00    1.00000 /
--2
    0.00    0.00000
    0.05    0.00000
    0.10    0.00000
    0.15    0.00001
    0.20    0.00012
    0.25    0.00065
    0.30    0.00210
    0.33    0.00373
    0.35    0.00525
    0.40    0.01107
    0.45    0.02083
    0.50    0.03601
    0.55    0.05836
    0.60    0.08988
    0.65    0.13284
```

```
  0.70   0.18977
  0.75   0.26345
  0.80   0.35697
  0.85   0.47364
  0.90   0.61706
  0.95   0.79113
  0.97   0.87026
  1.00   1.00000 /
--3
  0.00   0.000000000
  0.05   0.000000000
  0.10   0.000000000
  0.15   0.000000136
  0.20   0.000006041
  0.25   0.000055486
  0.30   0.000267604
  0.33   0.000574721
  0.35   0.000906789
  0.40   0.002457871
  0.45   0.005710842
  0.50   0.011854029
  0.55   0.022574912
  0.60   0.040167981
  0.65   0.067649131
  0.70   0.108876209
  0.75   0.168675370
  0.80   0.252972944
  0.85   0.368932583
  0.90   0.525097449
  0.95   0.731537257
```

```
    0.97    0.830761782
    1.00    1.000000000          /
--4
    0.00    0.000000
    0.05    0.000000
    0.10    0.000000
    0.15    0.000010
    0.20    0.000152
    0.25    0.000772
    0.30    0.002439
    0.35    0.005954
    0.40    0.012346
    0.45    0.022872
    0.50    0.039018
    0.55    0.062500
    0.60    0.095260
    0.65    0.139470
    0.70    0.197531
    0.75    0.272072
    0.80    0.365950
    0.85    0.482253
    0.90    0.624295
    0.95    0.795620
    1.00    1.000000 /
--Imbibition:
--5
  0.00      0.00000
    0.05    0.00000
    0.10    0.00000
    0.15    0.00004
```

```
  0.20   0.00042
  0.25   0.00176
  0.30   0.00487
  0.33   0.00798
  0.35   0.01072
  0.40   0.02045
  0.45   0.03530
  0.50   0.05663
  0.55   0.08594
  0.60   0.12480
  0.65   0.17488
  0.70   0.23798
  0.75   0.31595
  0.80   0.41074
  0.85   0.52439
  0.90   0.65901
  0.95   0.81679
  0.97   0.88689
  1.00   1.00000 /
--6
    0.00     0.00000
    0.05     0.00000
    0.10     0.00000
    0.15     0.00001
    0.20     0.00012
    0.25     0.00065
    0.30     0.00210
    0.33     0.00373
    0.35     0.00525
    0.40     0.01107
```

```
       0.45     0.02083
       0.50     0.03601
       0.55     0.05836
       0.60     0.08988
       0.65     0.13284
       0.70     0.18977
       0.75     0.26345
       0.80     0.35697
       0.85     0.47364
       0.90     0.61706
       0.95     0.79113
       0.97     0.87026
   1.00    1.00000 /
--7
    0.00     0.000000000
      0.05    0.000000000
      0.10     0.000000000
      0.15     0.000000136
      0.20     0.000006041
      0.25     0.000055486
      0.30     0.000267604
      0.33     0.000574721
      0.35    0.000906789
      0.40     0.002457871
      0.45     0.005710842
      0.50     0.011854029
      0.55     0.022574912
      0.60     0.040167981
      0.65     0.067649131
      0.70     0.108876209
```

```
        0.75     0.168675370
        0.80     0.252972944
        0.85     0.368932583
        0.90     0.525097449
        0.95     0.731537257
        0.97     0.830761782
     1.00    1.000000000          /
--8
     0.00    0.000000
        0.05    0.000000
        0.10    0.000000
        0.15    0.000010
        0.20    0.000152
        0.25    0.000772
        0.30    0.002439
        0.35    0.005954
        0.40    0.012346
        0.45    0.022872
        0.50    0.039018
        0.55    0.062500
        0.60    0.095260
        0.65    0.139470
        0.70    0.197531
        0.75    0.272072
        0.80    0.365950
        0.85    0.482253
        0.90    0.624295
        0.95    0.795620
     1.00    1.000000 /
SGFN
```

```
-- Gas Saturation Functions
--  Sg          krg         Pc
-- ----       -------    ------
-- Corey
-- Pc: unknown source
-- Drainage 1:Fine Sand, 2: Silt, 3: Sandy Clay, 4: Sandstone
-- Imbibition  5:Fine Sand, 6: Silt, 7:Sandy clay, 8: Sandstone
--1
   0.00    0.000000000  1*
   0.03    0.000056540  1*
   0.05    0.000260152  1*
   0.10    0.002048638  1*
   0.15    0.006802120  1*
   0.20    0.015852721  1*
   0.25    0.030422323  1*
   0.30    0.051615933  1*
   0.33    0.067924872  1*
   0.35    0.080413816  1*
   0.40    0.117662035  1*
   0.45    0.164060842  1*
   0.50    0.220150071  1*
   0.55    0.286290218  1*
   0.60    0.362636996  1*
   0.65    0.449105417  1*
   0.70    0.545315700  1*
   0.75    0.650504049  1*
   0.80    0.763353622  1*
   0.85    0.881586765  1*
   0.90    1.000000000  1*   /
--2
```

```
    0.00    0.000000000  0.00000
    0.03    0.000076310  0.01668
    0.05    0.000348928  0.01701
    0.10    0.002704039  0.01791
    0.15    0.008832373  0.01891
    0.20    0.020242583  0.02003
    0.25    0.038187920  0.02129
    0.30    0.063669508  0.02273
    0.33    0.082899180  0.02369
    0.35    0.097439993  0.02438
    0.40    0.140007640  0.0263
    0.45    0.191641003  0.02857
    0.50    0.252374333  0.03127
    0.55    0.322013975  0.03455
    0.60    0.400146135  0.03863
    0.65    0.486146650  0.04385
    0.70    0.579193882  0.05074
    0.75    0.678286914  0.06032
    0.80    0.782274096  0.07453
    0.85    0.889906787  0.09790
    0.90    1.000000000  0.14378  /
--3
    0.00    0.000000000  1*
    0.05    0.000555149  1*
    0.10    0.004141031  1*
    0.15    0.013020474  1*
    0.20    0.028731863  1*
    0.25    0.052208516  1*
    0.30    0.083892059  1*
    0.35    0.123839465  1*
```

```
  0.40   0.171823356  1*
  0.45   0.227425088  1*
  0.50   0.290120055  1*
  0.55   0.359354507  1*
  0.60   0.434612961  1*
  0.65   0.515475047  1*
  0.70   0.601660127  1*
  0.75   0.693057289  1*
  0.80   0.789736825  1*
  0.85   0.891935895  1*
  0.90   1.000000000  1*  /
--4
  0.00   0.000000000  1*
  0.03   0.000068370  1*
  0.05   0.000313410  1*
  0.10   0.002444481  1*
  0.15   0.008037088  1*
  0.20   0.018543181  1*
  0.25   0.035219929  1*
  0.30   0.059126507  1*
  0.33   0.077306009  1*
  0.35   0.091120427  1*
  0.40   0.131853300  1*
  0.45   0.181765860  1*
  0.50   0.241081999  1*
  0.55   0.309801439  1*
  0.60   0.387690449  1*
  0.65   0.474269600  1*
  0.70   0.568796680  1*
  0.75   0.670240944  1*
```

```
   0.80    0.777239393  1*
   0.85    0.888005474  1*
   0.90    1.000000000  1*  /
--Imbibition curves:
--5
   0  0         1*
   0.1  0         1*
   0.2  0         1*
   0.3  0.007708224 1*
   0.4  0.057187507 1*
   0.5  0.153603921 1*
   0.6  0.298965698 1*
   0.7  0.492019018 1*
   0.8  0.726244975 1*
   0.9  0.983269479 1* /
--6
  0 0          0.00
  0.1 0          0.01791
  0.2 0          0.02003
  0.3 0.009987375 0.02273
  0.4 0.070271979 0.02438
  0.5 0.180123831 0.02857
  0.6 0.335143321 0.03455
  0.7 0.527966068 0.05074
  0.8 0.748288171 0.07453
  0.9 0.983819708 0.14378   /
--7
  0 0         1*
  0.1 0         1*
  0.2 0         1*
```

```
  0.3 0.01465062  1*
  0.4 0.091862356 1*
  0.5 0.215230144 1*
  0.6 0.372156053 1*
  0.7 0.554318331 1*
  0.8 0.757977858 1*
  0.9 0.983859775 1* /
--8
  0 0         1*
  0.1 0         1*
  0.2 0         1*
  0.3 0.009095916 1*
  0.4 0.065356193 1*
  0.5 0.170588834 1*
  0.6 0.3228343171    1*
  0.7 0.516653896 1*
  0.8 0.742234284 1*
  0.9 0.983740963 1* /

EHYSTR
   0.1  8  1.0  0.1  KR  RETR DRAIN OIL  NO NO NO 0.0 /

--DIFFC
----  Mw1   Mw2    Dgg        Dog        Dgo         Doo        Dgocp     Dogcp
---- g/mol g/mol   m2/d       m2/d       m2/d        m2/d       m2/d      m2/d
----  18.0  44.0  4.32E-03  4.32E-03  1.782E-04  3.456E-04  1.0 /
--    18.0  44.0   0.0        0.0       1.782E-04   0.0        1.0 /
--    18.0  44.0   0.0        0.0       1.782E-04   0.0        1.0 /
--
---- ================================================================================
```

```
REGIONS
---- ================================================================================
-- Assigning drainage curves to different reginons
SATNUM
 32000*1 16000*2 16000*4 16000*3 16000*2 1600*3/
-- Assigning imbibition curves to different reginons
IMBNUM
32000*5 16000*6 16000*8 16000*7 16000*6 1600*7/


EQUALS
--array value ix1 ix2 jy1 jy2 kz1 kz2
FIPNUM    1     1  40   1  40   1  61/
FIPNUM    2   16  25  16  25   50 61/
/

--PVTNUM
--6400*1 505600*2/
--EQLNUM
--6400*1 505600*2/
--

--================================================================
SOLUTION
--================================================================

EQUIL
--Datum depth   Pinit  WOC     pcwoc    GOC   pcgoc   Rs   Rv  Accuracy
--   m           bar    m       bar      m     bar
     0          1    400      0.0     0.0   0.0     1    0     /
```

```
--   0          1    400      0.0     0.0   0.0     1    0     /

--RESTART
-- 'RADDIFFGROV'  50 /

RPTRST
BASIC=2 DEN /

RPTSOL
RESTART=1 /

SUMMARY ==============================================================
-------- THIS SECTION SPECIFIES DATA TO BE WRITTEN TO THE SUMMARY FILES
-------- AND WHICH MAY LATER BE USED WITH THE ECLIPSE GRAPHICS PACKAGE
FGIPL
FGIPG
FGIT
FGIR
FPR
FGPR
FGPT
FLPR
FLPT

WBHP
/
RGIPG
/
RPR
/
```

```
WGIT
/

SEPARATE

RPTONLY

RUNSUM

EXCEL

SCHEDULE ================================================================
---------THIS SECTION SPECIFIES THE OPERATIONS TO BE SIMULATED
------------------------------------------------------------------------

RPTSCHED
 FIP RESTART=2 /


MESSAGES
-- Print limits                                          Stop limits
-- Messages Comments Warning Problems Error Bug  Messages Comments Warnings Problems Error Bug
    6000     6000    10000   100000    2    100   60000    60000    100000   1000000    2   100 /

WELSPECS
-- General Spesification Data For Wells
--    WELL    WELL   L O C A T I O N     BHP    PREF.   DRAINAGE
--    NAME    GROUP    I        J      DATUM   PHASE    RADIUS
--   -------  -----  -----     ----     -----   -----   -------
     'WELLI'  'G1'     20       20        1*    'GAS'     1* /
```

```
/

COMPDAT
-- Connection Between Wells and Blocks
--    WELL         L O C A T I O N                    Saturation  Transmis.  Well Bore
--    NAME      I     J     K(upper) K(lower) STATUS  Table No.   Factor     Diameter   Eff. Kh  Skin  D-fact
    Direction
--   ------   -----  ---   -------- --------  ------ ----------  ---------  ---------   -------  ----  ------
    ---------
     'WELLI'    20    20       55      55     'OPEN'     0          1*         0.10       1*       1*    1*
                1*    /
/


WTEST
-- Name    Period  Reason   Maximum tests
   ----    ------  ------   -------------
  'WELLI'    .1      'P'         1*        /
/

TUNING
--TSINIT  TSMAXZ  TSMINZ  TSMCHP  TSFMAX  TSFMIN  TSFCNV  TSDIFF  THRUPT TMAXWC
  0.0001    0.5   0.0001/
--TRGTTE  TRGCNV  TRGMBE  TRGLCV  XXXTTE  XXXCNV  XXXMBE  XXXLCV  XXXWFL  TRGFIP  TRGSFT
/
-- NEWTMX   NEWTMN  LITMAX  LITMIN  MXWSIT  MXWPIT DDPLIM  DDSLIM  TRGDPR  XXXDPR
     12       1       200/

TUNINGDP
/
```

```
--       TRGDDP  TRGDDS
--1*   1*   1.0     0.01 /

WCONINJE
-- Control Data For Injection Wells
--    WELL    INJ              CONTROL   FLOW-RATE-TARGET     BHP      THP     VFP    VAPORIZED OIL IN
--    NAME    TYPE    STATUS    MODE    SURFACE  RESERVOIR   TARGET   TARGET  TABLE$\#$   INJECTION GAS
--   ------  ------   ------   -------  -------  ---------   ------   ------  ------   -------------
     'WELLI' 'GAS'    'OPEN'   'RATE'     50        1*        10       1*      0         1*   /
/

TSTEP
 9*7 /
WCONINJE
-- Control Data For Injection Well
--    WELL    INJ              CONTROL   FLOW-RATE-TARGET      BHP      THP
--    NAME    TYPE    STATUS    MODE    SURFACE  RESERVOIR    TARGET   TARGET
--   ------  ------   ------   -------  -------  ---------   --------  ----
     'WELLI' 'GAS'    'SHUT'   'RATE'    0         1*           10       1*    /
/
TSTEP
 9*7 /

END
```